arXiv:1404.0152v1 [astro-ph.GA] 1 Apr 2014

Dynamics of ten clusters of galaxies with substructures

Kiran Lakhchaura[1] and K. P. Singh

Department of Astronomy and Astrophysics, Tata Institute of Fundamental Research,

1 Homi Bhabha Road, Mumbai 400 005, India

Received _____; accepted _____

[1]e-mail : kiran_astro@tifr.res.in

ABSTRACT

We present a detailed *Chandra* study of a sample of ten clusters of galaxies selected based on the presence of substructures in their optical images. The X-ray surface brightness maps of most of these clusters show anisotropic morphologies, especially in the central regions. A total of 22 well resolved significantly bright X-ray peaks (corresponding with high-density regions) are seen in the central parts (within $r_c/2$) of the clusters. Multiple peaks are seen in central parts of six clusters. Eleven peaks are found to have optical counterparts (10 coinciding with the BCGs of the 10 clusters and one coinciding with the second brightest galaxy in A539). For most of the clusters, the optical substructures detected in the previous studies are found to be outside the field of view of *Chandra*. In the spectroscopically produced 2-D temperature maps, significantly lower temperatures are seen at the location of three peaks (two in A539 and one in A376). The centers of five clusters in our sample also host regions of higher temperature compared to the ambient medium, indicating the presence of galaxy scale mergers. The X-ray luminosity, gas mass and central cooling time estimates for all the clusters are presented. The radial X-ray surface-brightness profiles of all but one of the clusters are found to be best-fitted with a double-β model, pointing towards the presence of double-phased central gas due to cool-cores. The cooling time estimates of all the clusters, however, indicate that none of them hosts a strong cool-core, although the possibility of weak cool-cores cannot be ruled out.

Subject headings: Galaxies: clusters: general — Galaxies: clusters: individual:(A193, A376, A539, A970, A1377, A1831B, A2124, A2457, A2665, A3822) — Galaxies: clusters: intracluster medium — X-rays: galaxies: clusters

1. Introduction

Clusters of galaxies, the largest known gravitationally bound objects, are believed to grow by the mergers of smaller groups of galaxies (Geller & Beers 1982; Dressler & Shectman 1988; Girardi et al. 1997; Kriessler & Beers 1997; Jones & Forman 1999; Schuecker et al. 2001; Burgett et al. 2004). The intracluster medium (ICM), i.e. the hot (T$\sim 10^7 - 10^8$K) and tenuous (n$\sim 10^{-3}$ cm^{-3}) ionized plasma that fills the space between the galaxies in a cluster, emits in the X-rays mainly through bremsstrahlung and line emission (Kellogg et al. 1972; Mitchell et al. 1979; Sarazin 1988; McNamara & Nulsen 2007).

Based on their X-ray morphologies, clusters of galaxies can be classified as regular (or evolved clusters) and irregular (or early type clusters; see Sarazin 1988). In general, the X-ray surface-brightness profiles of the rich, evolved and relaxed clusters are smooth in the outer parts and sharply peaked at the centres (Forman & Jones 1982; Sarazin 1988). The central sharp peaks characterize a very important phenomenon in the relaxed clusters, viz. the "central cooling flows". Until very recently, the central gas in clusters was thought to be a "single phase" rapidly cooling dense gas, that is pushed towards the cluster centre by the pressure exerted by the outer layers, thereby, constituting the "cooling flows" (see Sarazin 1988; Fabian 1994, for a review). However, the absence of large amounts of expected cooled gas at the centre, the inadequacy of the single-β model to fit the X-ray surface brightness profiles of the clusters (specially at the centres) and the requirement of an additional cool component in the model while fitting the X-ray spectrum of the central region, led to the "two phase" model of central gas in the clusters (Fukazawa et al. 1994; Makishima et al. 2001; Takahashi et al. 2009; Gu et al. 2012). In this model, the central region of the clusters is assumed to be filled with a mixture of a hotter and a cooler X-ray gas phase. Unlike the rich and relaxed clusters, the X-ray surface brightness distributions of the relatively poorer, younger and unrelaxed clusters are characterized by significant substructures and relatively

smaller and multiple central peaks (see Forman & Jones 1990; Jones & Forman 1992, 1999; Schuecker et al. 2001).

Mergers in the clusters are characterized by shocks that compress the intracluster gas and result in an increase in the temperature (and hence, entropy and pressure) of the ICM. This creates large scale anisotropies in the thermodynamic maps of the clusters (Roettiger et al. 1996). Mergers generate bulk gas flows and turbulence in the ICM, and therefore, can result in the disruption of central cooling flows in the unrelaxed clusters (see Fabian 1994; Markevitch & Vikhlinin 2007; Owers et al. 2011; Maurogordato et al. 2011). In addition, mergers can also lead to metal enrichment of the ICM through enhanced ram-pressure stripping (Domainko et al. 2005). Observations of the clusters with the *Chandra X-ray Observatory* (CXO) have led to a better understanding of various small-scale phenomena in the clusters, such as central morphologies, shock and cold fronts, "cavities" due to radio sources and the cooling flow problem.

In this paper, we present a study of the X-ray properties of the ICM in a sample of ten low-redshift ($0.028 \leq z \leq 0.76$) clusters of galaxies using the publicly available *Chandra* X-ray data. Our sample contains A193, A376, A539, A970, A1377, A1831B, A2124, A2457, A2665, and A3822, selected on the basis of the presence of significant substructures in their optical images, as revealed in Flin & Krywult (2006) and Ramella et al. (2007). The study aims at finding evidence for X-ray substructures and/or mergers in these clusters. X-ray morphology and the thermodynamic maps of the clusters are the two main tools used for this purpose.

The paper is organized as follows. Details of the *Chandra* observations used in this paper, and the data reduction methods employed are presented in §2. The resultant X-ray maps overlaid on the optical maps, the radial profiles of X-ray surface-brightness, the global spectral parameters, the azimuthally averaged profiles of the projected spectral parameters

and the two-dimensional projected thermodynamic maps are presented in §3. A discussion based on the general properties of the clusters derived on the basis of these results is given in §4. A comparison of the values of the general L_X-kT scaling relation for the clusters of galaxies with the values obtained for our sample, and its implications are discussed in §4.2. Special features and other properties of individual clusters are summarized in §4.3. A lambda cold dark matter cosmology with $H_0 = 70$ km s^{-1} Mpc^{-1} and $\Omega_M = 0.3$ ($\Omega_\Lambda = 0.7$) has been assumed throughout.

2. X-ray observations and Data Reduction

Redshifts and celestial coordinates of the ten clusters studied here along with a log of their *Chandra* observations (observation IDs, dates of observations and exposure times) are given in Table 1. The data were analyzed with the CIAO version 4.3 and CALDB version 4.4.0. X-ray images for all clusters were made in the 0.3-8.0 keV band using the ciao task *dmcopy* with a pixel size of 4.0″. The diffuse X-ray emission maps of the clusters were made as follows: (a) Point sources were detected using the CIAO task *wavdetect*, and were removed from both the image and event files. The holes created in the X-ray images due to the removal of point sources were filled with the average value of the counts in the neighboring pixels, using the ciao task *dmfilth*. (b) Exposure maps were created for all the clusters, which were used to normalize the X-ray images. (c) The normalized images were smoothed using Gaussian kernels of appropriate width (see the caption of Figure 1), using the ciao task *aconvolve*. One of the clusters, A539, was observed twice with the *CXO*, therefore, combined event files and exposure maps from both the observations were used to create the exposure corrected images of the cluster. Radial profiles of X-ray surface brightness of all the clusters were produced from the normalized and unsmoothed diffuse X-ray emission maps obtained from step (b). To make these profiles we calculated the

average surface-brightness for a number of circular annuli, and the total number of and size of the annuli were chosen on the basis of total number of photon counts in that cluster (see §3.3). The last annulus was fixed such that the surface brightness calculated for that annulus is at least 1.25 σ above the mean local background.

Using the point source removed event files, average spectra of all the clusters were extracted in the energy band of 0.5-7.0 keV, and used in the analysis described in §3.3. To make radial profiles of various thermodynamical quantities (described in §3.4), spectra were extracted in a number of circular annuli in each cluster (except in A970 and A1377). The total number of the circular annuli was chosen such that each annulus has sufficient ($\geq$600) counts in it. For each cluster, the brightest peak of the X-ray emission was fixed as a common centre for all the annuli, and spectra were extracted in the energy band of 0.5-7.0 keV. Spectra were also extracted from a number of box-shaped regions in each cluster in the energy range of 0.5-7.0 keV. All spectra were analyzed using XSPEC (§3.3) and resultant spectral parameters were used to make maps of thermodynamic quantities (§3.5). The number and sizes of boxes were chosen carefully such that each box had sufficient ($\geq$600) counts in it. In the inner brighter parts of the cluster small sized boxes were chosen and in the outer fainter parts larger boxes were chosen. Spectral information for A539 was extracted separately from the two independent exposures but the spectral data were analyzed simultaneously with a common spectral model.

It was found that local background subtraction was not sufficient for removing the particle and cosmic background components present in the average X-ray spectra of the clusters, and large residuals were seen in the high-energy-end of the spectrum of all clusters. Additionally, as most of these sources have low redshifts, their emission filled nearly the entire field of view of the detector and it was impossible to find nearby emission-free regions. Therefore, we used the *Chandra* blank-sky background observations to create

the background spectrum for all the spectral analyses. For this we followed the standard procedure described in the *CXO science threads*. No background subtraction was done for the imaging analysis used to make the surface brightness maps. Local background subtraction was, however, used while making the radial profiles of X-ray surface-brightness. For this purpose, background was estimated from an annular region just outside the outermost annulus used in making the surface-brightness profiles.

3. Analysis and Results

3.1. X-ray and Optical Morphology

The exposure-corrected, point source removed and smoothed X-ray images of all the ten clusters, produced in §2, are shown in the left-hand-side of Figure 1. Six of the ten clusters showed significant substructures or multiple peaks in their central regions. Therefore, zoomed-in images of their central regions have been shown in the left-hand-side of Figure 2. The right-hand-sides of Figures 1 and 2 show the overlays of the X-ray intensity contours on the optical images of the clusters from the SuperCOSMOS survey in the B_J band. The Brightest Cluster Galaxies (BCGs) of some of the clusters are found to be shifted away from their X-ray peaks, and the shift is maximum for A970 ($\sim 33'' = 38$ kpc). The departure from spherically symmetric X-ray morphology is found to be maximum for A1377. A detailed discussion on the X-ray and optical morphologies of the individual clusters is given in §4.3.

3.2. X-ray Surface Brightness Profiles

The radial profiles of X-ray surface brightness of the ten clusters, produced in §2, are shown in Figure 3. The profiles were fitted with both single-β model

($S(r)= S_{01}(1+(r/r_{c1})^2)^{-3\beta+0.5}$) and double-$\beta$ model ($S(r)= \sum_{i=1}^{2} S_{0i}(1+(r/r_{ci})^2)^{-3\beta+0.5}$). Here, S(r) is the total surface-brightness at a distance r from the centre of the cluster; S_{0i} and r_{ci} are values of peak surface-brightness and core radius for the i^{th} component of the model (i=1 for single-β model and i=1,2 for double-β model), and β is the ratio of the specific kinetic-energy of the dark-matter particles to that of the intracluster gas (Rosati et al. 2002).

All the ten clusters were fitted with the single-β model using chi-square minimization. The average value of minimum reduced chi-square ($(\chi^2_\nu)_{min}$) thus obtained was $\sim$2.8, resulting in a poor fit in all cases. The best-fit parameter value for the core radii (r_{c1}) were in the range of 70-270 kpc. We, therefore, employed the double-β model to all the clusters. As a result, the value of $(\chi^2_\nu)_{min}$ reduced to $\sim$1 for all the clusters, except A1377. The improvement in the fit is >99% based on F-statistic. The cluster A1377 showed a very poor fit for both the single-β and double-β models with the value of $(\chi^2_\nu)_{min} \sim 2.4$ in both cases. For this cluster, the results did not improve even when the values of S_{02}, r_{c2} and β parameters, single or combined, were frozen to the values of S_{01}, r_{c1} and β, obtained from the single-β model fit, respectively. The results of the double-β model fitting for the nine clusters and single-β model fitting for A1377, are given in Table 2. All the fits are shown as dashed lines in Figure 3. For seven clusters viz. A376, A539, A970, A2124, A2457 and A2665, A3822, that showed large central residuals in their single-β fits, the radii of the smaller core components (r_{c1}) obtained from the double-β fits were found to lie in the range of $\sim$18-46 kpc. For A193 and A1831B, the best-fit values of r_{c1} were found to be 64 kpc and 118 kpc respectively, which are significantly larger than those obtained for the other seven clusters.

Considering the possibility of X-ray emission from the cluster's hot gas being affected by emission from the central bright galaxies, we removed the central galaxy regions (the

central 20-25 kpc regions) from the surface-brightness profiles of all the clusters. The resultant profiles were then fitted with the single-β model. Despite the absence of large central excess emission, the improvement in $(\chi^2_\nu)_{min}$ obtained from the new single-β model fit was not significant relative to the initial single-β fits, for all the clusters except A376 and A539. For these two clusters, the value of $(\chi^2_\nu)_{min}$ for the new single-β fits was found to be close to 1. This was expected for A376 and A539, as the core radius r_{c1} from their double-β model fits was found to be $\sim$ 20 kpc (see Table 2), which is comparable to the zone of exclusion. For the other eight clusters (with $r_{c1} > 30$ kpc), the average value of $(\chi^2_\nu)_{min}$ for the new single-β model fits was found similar to that obtained in the initial single-β fits. A discussion based on all these results and their implications, is given in §4.

3.3. Average X-ray Spectral Analysis

X-ray spectral fitting package XSPEC was used for all the spectral analyses done in this paper. Average spectra for all clusters were extracted as described in §2. For the spectral fits, the single-temperature *apec* plasma emission model (Smith et al. 2001) (with the AtomDB code v2.0) along with the *wabs* photoelectric absorption model (Morrison & McCammon 1983), was used. Relative elemental abundances used in the *apec* model are from Anders & Grevesse (1989) and those for the *wabs* model are from Anders & Ebihara (1982). Due to the poor spectral statistics multi-temperature fits could not be constrained. The neutral hydrogen column densities along the line of sight to the clusters (N_H) were frozen to the values (see Table 3) obtained from the Leiden/Argentine/Bonn (LAB) Galactic HI survey (Kalberla et al. 2005). The redshifts (Table 1) were frozen to the values obtained from the SIMBAD astronomical database, for all the clusters, except A1831B, for which the redshift obtained by Kopylov & Kopylova (2010) was used. The resulting spectra of all the clusters, along with the histograms of best

fit model spectra are shown in Figure 6. The best fit values of the temperature, abundance and *apec* normalizations are given in Table 3. The maximum average temperature of 5.3 ± 0.3 keV is seen for A3822, while A1377 is found to have the minimum average temperature of 1.7 ± 0.2 keV. The estimated average elemental abundance for the clusters ranges from 0.09 ± 0.04 (for A1377) to 0.5 ± 0.1 (for A2665) times the solar value. We have also estimated the X-ray luminosity in the energy range 0.5-7.0 keV (L_X) and the bolometric X-ray luminosity (L_X^{bol}) in the energy range 0.1-100 keV (using the '*dummyrsp*' command in XSPEC) for all the clusters. The L_X^{bol} values of all the clusters were scaled up to a radius of r_{200} (radius within which mean density of the cluster equals 200 times the critical density at the redshift of the cluster), using the double β-model fits obtained for their X-ray surface brightness in §3.2. The R_{200} values were obtained from the literature and for A2665, for which R_{200} could not be found in the literature, a typical value of 1.5 Mpc was assumed. The values of L_X and L_X^{bol}, along with the R_{200} values used and their references, are given in Table 4. The results show that A3822, the hottest cluster of the sample, is also the most X-ray luminous cluster while A1377, the coolest cluster, is the least X-ray luminous.

3.4. Radial Profiles of Thermodynamic Quantities : Cooling time and Gas Mass

We have produced the azimuthally averaged profiles of temperature (kT), electron number density (n_e), entropy (S), and pressure (P) for all the clusters of the sample, except for A970 and A1377. These two clusters were dropped in this analysis because their X-ray surface brightness maps were found to be the most asymmetrical/irregular in the whole sample. Spectra were extracted as described in §2. The details of the spectral analyses performed for this section are the same as given in §3.3, except that here the elemental abundances of all the annuli belonging to a specific cluster have been frozen to the

respective average abundance value obtained for that cluster in §3.3. The temperature (kT) of each annulus was obtained as a direct result of the spectral analyses and the temperature profiles obtained for all the clusters are shown in Figure 5. The values of the normalization constants (K) obtained for the *apec* model fitted to data from each annulus, and the relation $K = 10^{-14}EI/(4\pi[D_A(1+z)]^2)$ from Henry et al. (2004) were used to derive the electron density (n_e) for that annulus. Here, EI is the emission integral $\int n_e n_p dV$. The units assumed for K, n_e (n_p) and D_A in the above relation are cm^{-5}, cm^{-3} and cm, respectively. Density is assumed to be constant within each annulus. Using $n_p = 0.855n_e$ (Henry et al. 2004), we obtained, $EI = 0.855n_e^2 V$, where V is the volume of non-deprojected spherical shell (if r_o and r_i are the radii of the inner and outer annuli of the annular shell (in angular units) then $V = 4/3D_A^3\pi\Omega(r_o^2 - r_i^2)$, where Ω is the solid angle subtended by the annular shell). The resulting density profiles are shown in Figure 6. To calculate the entropy (S) and the pressure (P) for an annulus, we used the relations $S = kTn_e^{-2/3}$ and $P = n_e kT$, respectively (Gitti et al. 2010). The resulting entropy and pressure profiles are shown in Figures 7 and 8, respectively.

The density, entropy and pressure profiles of all the eight clusters show an average decrease, increase and decrease, respectively, from the centre outwards. The temperature profiles of all the clusters, however, seem to be almost isothermal, though a significantly low temperature is found at the centre of A2457. A high temperature in the outermost annulus of A2665 and in the fourth (counting from the centre outwards) annulus of A3822 is also found. The projection effects along the line of sight to a cluster tend to smooth out the spatial variations of the thermodynamic quantities. Therefore, we also carried out a deprojection analysis of the annuli spectra for each cluster, using the techniques described in Lakhchaura et al. (2011, 2013). The resulting deprojected profiles of thermodynamic quantities (although in agreement with the projected profiles) had very large errors and, therefore, are not shown in this paper. However, we have used the central gas temperatures

and densities derived from the deprojection analysis and the following equations from Sarazin (1988) to calculate the cooling times for the eight clusters studied in this section.

$$t_{cool} = 8.5 \times 10^{10} yr \left[\frac{n}{10^{-3} cm^{-3}}\right]^{-1} \left[\frac{T_g}{10^8 K}\right]^{1/2} \quad (1)$$

The estimated cooling times of the eight clusters are given in Table 4. Cooling times of all the clusters are found to be much greater than the Hubble time therefore, none of them seems to be a cool-core-cluster. The poor statistics and large errors in the estimated cooling times, however, do not preclude the possibility of a weak cooling flow in some of the clusters. Deeper *Chandra* observations of the central parts of the clusters are required for a better estimation of the cooling times.

We have estimated the gas mass for each cluster by fitting the projected gas densities using the single β-model i.e.,

$$n_e(r) = n_e(0) \left(1 + \frac{r^2}{r_c^2}\right)^{(3/2)\beta}, \quad (2)$$

where $n_e(0)$ is the central density and r_c is the core radius. The following formula from Donnelly et al. (2001) was used to estimate the gas mass ($M_{gas}(r)$) of all the eight clusters studied in this section out to radii 1 Mpc and R_{200} :

$$M_{gas}(r) = 4\pi\rho_0 \int_0^r s^2 \left[1 + \left(\frac{s}{r_c}\right)^2\right]^{(3/2)\beta} ds \quad (3)$$

$\rho_0 = \mu n_e(0) m_p$; where m_p and μ (=0.609 from Gu et al. (2010)) are the mass of a proton and the average molecular weight for a fully ionized gas. We also tried fitting the double-β model to the density profiles but due to very few data points available, the results obtained were not significant. The estimated values of the gas mass of eight clusters are given in Table 4.

3.5. 2D Projected Thermodynamic Maps

For a better resolved estimation of the spatial variations of the thermodynamic quantities we have produced projected temperature (kT), abundance, density (n_e), entropy (S), and pressure (P) maps for all the ten clusters of our sample. Spectra were extracted from box shaped regions as described in §2. Details of the spectral fitting, and the relations used to calculate the electron density (n_e), entropy (S), and pressure (P) are given in §3.3 and §3.4, respectively. The volume of each box was calculated using the relation given in Henry et al. (2004) and Ehlert et al. (2011). The resulting temperature (kT) maps are shown in Figure 9, the electron density (n_e) maps are shown in Figure 10, the entropy (S) maps are shown in Figure 11, and the pressure (P) maps are shown in Figure 12. The temperature maps of most of the clusters show anisotropies and high temperature regions in many parts of the cluster except A193 which seems to be mostly isothermal except at the centre. The maps of density, entropy and pressure of all the clusters show an average decrease, increase and decrease from the central outwards, as seen in the azimuthally averaged profiles. The various features observed in the thermodynamic maps are discussed in detail in §4.3 for the individual clusters.

4. Discussion

4.1. Global properties

The 2-D X-ray substructure and thermodynamic maps of the ten clusters, resulting from a detailed analysis of their *Chandra* archival data, are being presented here for the

first time.[1] Due to the small field of view of *Chandra*, the observations did not cover the outer parts of the clusters and, therefore, for many of the clusters the optical subclusters reported by Flin & Krywult (2006) and/or Ramella et al. (2007) are found to be outside the field of view of *Chandra*.

The X-ray surface brightness profiles of all the clusters (except A1377) are found to be better fitted with the double-β model than the single-β model (see §3.2), suggesting the presence of a double-phase gas in their central regions, which is a characteristic of the cool-core clusters. The negligible improvement in the single-β model fits, after removing the central galaxy regions of the clusters (see §3.2), implies that the X-ray emission from the ICM is not significantly affected by the emission from the central galaxies. The results from the surface-brightness profile fits, thus, seem to be in contrast with the central cooling time estimates, which suggest an absence of strong central cooling in all the ten clusters (see §3.4). The central cooling time estimates of the clusters can be affected by mergers between the central galaxies. These mergers can lead to an increase in the central temperatures of the clusters which can result in an increase in the central cooling time estimates. Central galaxy mergers are evident in many of the clusters of our sample, that show multiple X-ray peaks and high temperature regions in their central regions (see §4.3). Due to the large errors in the cooling time estimates of the clusters, the weak cool-core and non cool-core segregation is extremely difficult. Therefore, based on our results we argue for an absence of strong cooling in the clusters in our sample. Deeper *Chandra* observations of the central parts are, therefore, required for a better estimation of the temperatures and densities in the central regions of the clusters, and to resolve the weak-cool-core/non-cool-core ambiguity.

The average values of temperatures of all the clusters are found to be consistent with

[1]Cavagnolo et al. (2009) have earlier produced and analyzed the X-ray surface-brightness and entropy profiles for four of the ten clusters A193, A376, A2124 and A539.

the typically observed values, and range between 1.7 keV to 5.3 keV. The average elemental abundances of all clusters, except A1377, are also found to be similar to the normally observed values, and range between 0.2 to 0.5 times the solar value. The radial temperature profiles of all the clusters of the sample (except A193 and A1831B) seem to be consistent with the generally observed isothermal profiles

in the centers of the non-cool core clusters. The temperature maps of many of these clusters show presence of significantly hotter/colder regions in their thermodynamic maps, specially in their central regions. This combined with the presence of multiple small peaks seen in the central bright regions of X-ray maps, indicate the presence of shocked hot gas or stripped off cold gas resulting from possible galaxy scale mergers in the centre of the clusters.

4.2. L_X-kT relation

The bolometric X-ray luminosities (L_X) of clusters of galaxies are generally found to have a power-law dependence on their average X-ray temperatures (kT) i.e. $L_X = K\ (kT)^{\alpha}$. Here 'K' is the constant of proportionality, and is equal to the expected bolometric X-ray luminosity for kT = 1keV. Figure 13 shows the relationship between the L_X and kT values obtained by Takey et al. (2013). The positions of the all the clusters of our sample are shown as rectangles and the well known merging clusters Coma and A754, the extremely relaxed cluster Perseus, and three of our previously studied clusters viz. A3395, A3532 and A3530 (Lakhchaura et al. 2011, 2013) are shown as diamonds. The results obtained by us for the ten clusters seem to be most consistent with the relation obtained by Takey et al. (2013). The only large outliers are the strong cool-core cluster Perseus which is shifted to the high luminosity side relative to all the L_X-kT relations, and A376 and A2124, shifted to the low luminosity side.

4.3. Individual Clusters

The X-ray morphologies of all the clusters of our sample show substructures and departures from spherical symmetry, especially in their central parts. Our analysis has revealed several interesting new features in the central regions of many clusters. Below we discuss the findings in each of the ten clusters.

A193: X-ray emission is detected (significance>3σ) up to a radius of about $400''$ ($\sim$0.4 Mpc $\sim R_{200}/5$) in this cluster (see Figure 3). In the X-ray image of the central part of this cluster, three distinct X-ray peaks (significant at $> 8\sigma$ above the immediate surroundings), marked as 1, 2 and 3 in Figure 2(a), are seen. The peaks have very similar X-ray brightness and, therefore, none of them stands out as the single brightest X-ray peak of the cluster. The apparent spatial extents of the peaks 1, 2 and 3 are $19'' \times 30''$, $21'' \times 21''$ and $34'' \times 24''$, respectively, significantly larger than the width of the smoothing Gaussian kernel used in Figure 2(a) ($= 4''$). The peak separations 1-2, 2-3 and 1-3 are about $33''$, $24''$ and $69''$ ($\sim$32 kpc, 23 kpc and 66 kpc), respectively. In the optical image of the cluster, the brightest optical peak is found to be located near the X-ray peak 1, which is associated with the BCG of the cluster (see Figure 2(b)). Another optical peak seen near the X-ray peak 2, is due to a foreground star located close to the line-of-sight to A193. The BCG in the optical image is separated from the X-ray peaks 1 and 2 by about $10''$ and $30''$ ($\sim$10 kpc and 29 kpc), respectively . Seigar et al. (2003) detected three infrared peaks in the I-band map of this cluster from the *Hubble Space Telescope (HST)*, and in the K-band map from the *United Kingdom InfraRed Telescope (UKIRT)*. Contours of infrared emission from the HST I-band map have been overlaid on the optical image of central part of the cluster, and are shown as an inset in Figure 2(b). All the infrared peaks are found coinciding with the BCG of the cluster, and have been marked as a, b and c in Figure 2(b), in a

decreasing order of infrared surface brightness. Considering their very small spatial extents these peaks do not seem to be related with the X-ray peaks. The infrared peaks seem to be star forming "hotspots" within the BCG. The irregular X-ray emission and multiple X-ray peaks in the central region of the cluster also point towards galaxy scale (∼20-60 kpc scale) mergers. Mergers are reinforced by the thermodynamic maps of the cluster. The temperature map (Figure 9(a)) shows a high temperature in the central region of the cluster (marked as 'a', average kT= $4.8^{+0.4}_{-0.3}$ keV). The temperature is significantly high compared to the average temperature of the immediate surrounding region (kT= 3.7 ± 0.2 keV). The density map (Figure 10(a)) shows a high density for the three peaks in Figure 2(a) ($n_e = (9.0 \pm 0.2) \times 10^{-3}$, $(10.2 \pm 0.5) \times 10^{-3}$ and $(9.5 \pm 0.2) \times 10^{-3}$ cm^{-3} for peaks 1, 2 and 3 , respectively). The entropy map shows a low entropy at the location of the peaks 1 and 2 ($= 87^{+13}_{11}$ and 77^{+27}_{-17} keV cm^2, respectively) and a high entropy ($= 115^{+28}_{-22}$ keV cm^2) at the location of peak 3 (see Figure 11(a)).

A376: We have detected X-ray emission (significance$\geq 3\sigma$) up to a radius of about 480″ (∼0.45 Mpc ∼$R_{200}/5$) in this cluster (see Figure 3). The X-ray image of the central region of A376 (Figure 2(c)) shows a compression of inner contours towards the NE. Along with the brightest X-ray peak (marked as '1' in Figure 2(c)), the cluster shows a secondary X-ray peak (marked as '2'), about 1.2′ (∼65 kpc) towards the SW of the brightest peak. Both the peaks are found to be significantly brighter than their immediate neighborhood (significance $> 21\sigma$ for peak 1 and $> 10\sigma$ for peak 2). The apparent spatial extent of peak 1 is $\sim 130'' \times 103''$ and that of peak 2 is $\sim 47'' \times 43''$, therefore both peaks are significantly larger than the width of the smoothing Gaussian kernel used in Figure 2(c) (= 8″). The brightest X-ray peak (peak 1) is found to be coinciding with the brightest galaxy in the optical image of the cluster (Figure 2(d)), although no optical counterpart is seen for the secondary X-ray peak. Proust et al. (2003) studied this cluster using the position and velocity informations of 73 member galaxies and found a regular distribution

of galaxies within the central 15′ (∼0.84 Mpc). They also found a substructure bound to the main cluster, separated by about 20′ (∼1.1 Mpc) towards the southwest (outside the *Chandra* FOV). The X-ray image of the cluster from the *Röentgen Satellite (ROSAT)* High Resolution Imager (HRI) given in Proust et al. (2003), shows a contraction of contours towards the NE similar to the *Chandra* image (see Figure 2(c)), although the secondary X-ray peak detected by us is not seen in the HRI image. Proust et al. (2010) again studied this cluster with 40 new galaxy velocity measurements, and found a bimodal distribution of galaxy velocities and a morphological segregation of late-type and early-type galaxies. They suggested a very complex dynamics for A376, and the possibility of an ongoing merger with the southwest subcluster. The temperature map of the cluster shown in Figure 9(b) indicates a drop in the temperature at the location of the secondary peak (kT= $2.7^{+0.5}_{-0.4}$ keV vs. $3.6^{+1.5}_{-0.4}$ keV at peak 1 in Fig. 2(c); ΔkT= 0.9 ± 0.6 keV). Two higher temperature regions are seen to the north (marked as 'a', kT= $4.7^{+0.9}_{-0.6}$ keV) and south (marked as 'b', kT= $5.4^{+1.3}_{-1.0}$ keV) side of the central region in Fig. 9(b). The entropy map of the cluster (Figure 11(b)) also shows significantly higher values of entropies in the regions 'a' and 'b' ($S_a = 186^{+37}_{-26}$ keV cm^2 and $S_b = 203^{+53}_{-41}$ keV cm^2). The entropy map also shows an entropy of $= 83^{+19}_{-16}$ keV cm^2 near the secondary peak (peak 2 in Fig. 2(c)) which is significantly lower than the value of entropy at the same distance from the centre (the brightest peak) on the diametrically opposite side (marked as 'c', $S_c = 178^{+45}_{-33}$ keV cm^2). The low values of temperature and entropy near the secondary X-ray peak suggest that the peak may be associated with the cool core of a small subcluster or a nearby galaxy that has already merged with the main cluster (see Kempner et al. 2002; Ma et al. 2012). The distortions of the X-ray contours (compression along NE and elongation along SW) and the presence of high temperature and high entropy regions in various parts of the cluster, seem to be the possible results of an ongoing merger between A376 and the southwest subcluster detected by Proust et al. (2003), and in agreement with the results of Proust et al. (2010).

A539: This is the nearest cluster in our sample with a redshift of 0.0284 (SIMBAD). In this cluster, we have detected X-ray emission (significance$\geq 3\sigma$) up to a radius of about $700''$ ($\sim$0.4 Mpc $\sim R_{200}/5$; see Figure 3). We find a double peak in the X-ray image of the central regions of this cluster (Figure 2(e), the brighter peak is marked as '1' and the other peak is marked as '2'). The peaks are found to be brighter than their immediate surroundings at a significance level of about 14σ. The spatial extents of peak 1 and 2 are $69'' \times 44''$ and $57'' \times 47''$, respectively, which are significantly larger than the width of the smoothing Gaussian kernel used in Figure 2(e) ($= 8''$). The projected separation between the two peaks is about $45''$ ($\sim$26 kpc). In the optical image the cluster (Figure 2(f)), many (at least five) bright galaxies are seen near the centre. In Figure 2(f), the X-ray peak 1 is found close to three of these galaxies (including the brightest optical galaxy of the cluster), although shifted from all of them by about $10''$ ($\sim$6 kpc). The X-ray peak 2 is close to the other two galaxies, and is at a projected separation of about $7''$ ($\sim$4 kpc) from them. Ostriker et al. (1988) detected the presence of two major spatially overlapping structures in A539, separated in velocity space by more than 4000 km s^{-1} (see also Girardi et al. 1997). Using wavelet analysis, Flin & Krywult (2006) also detected two groups of galaxies in the central parts of this cluster, at scales of 258 kpc ($\sim 7.5'$) and 188 kpc ($\sim 5.5'$). The X-ray images produced by us, however, do not show substructuring at these scales in this cluster. The double X-ray peaks at the centre of the cluster seem to be formed by the overlapping X-ray halos of the nearby five galaxies. All these galaxies have redshifts very close to the mean redshift of the cluster, and therefore are members of the cluster. The close proximity of these galaxies with the BCG of the cluster indicates possible interactions between them. However, the absence of high temperature and high entropy regions in between or at the location of these peaks rules out an ongoing merger between the galaxies (see Figures 9(c) and 11(c)). It appears that the galaxies have started coming together to merge with

the BCG in due course of time. In the temperature map, Fig. 9(c), and entropy map, Fig. 11(c), the two bright peaks in Fig. 2(e) seem to have significantly lower temperature ($2.7^{+0.3}_{-0.2}$ keV at peak 1 and 2.8 ± 0.1 keV at peak 2) and entropy (58^{+7}_{-5} keV cm^2 at peak 1 and 71^{+6}_{-5} keV cm^2 at peak 2) than their surrounding medium on the northern, western and southern side (marked as 'a', with average kT$\sim 3.1 \pm 0.1$ keV and average S$\sim 106 \pm 3$ keV cm^2). The outermost regions and the regions on the eastern side have a low temperature similar to that of the two peaks, although a small region on the westernmost edge of the map (marked as 'b') seems to have a slightly higher temperature of 3.0 ± 0.3 keV.

A970: In A970, the X-ray emission extends to a radius of about 360″ ($\sim$0.41 Mpc $\sim R_{200}/4.5$; see Figure 3). The cluster shows a highly asymmetric X-ray morphology (see Figure 1(g)). The X-ray contours seem to be highly compressed along the south-east and elongated along the north-west. A similar compression of contours towards the south-east was also observed in the *Einstein* Imaging Proportional Counter (IPC) image of the cluster (see Sodré et al. 2001). The X-ray peak seems to be significantly shifted (by about 2′ $\sim$140 kpc) towards the south-east from the centre of the outer X-ray contours. The cluster therefore, seems to be moving along the south-east. The brightest central galaxy, in the optical image of the cluster (Figure 1(h)), seems coinciding with the location of the compression of the X-ray contours. The temperature map of the cluster in Figure 9(d) seems to be bimodal with the eastern parts colder than the western parts ($kT_{east} = 4.1 \pm 0.4$ keV and $kT_{west} = 5.1 \pm 0.5$ keV $\Longrightarrow$ ΔkT$\sim 1.0 \pm 0.6$ keV). The results obtained by us, thus, suggest that the cluster is out of dynamical equilibrium, in agreement with the findings of Sodré et al. (2001). Sodré et al. obtained a very high value of the velocity dispersion ($\sim$845 km s^{-1}) and large scale velocity gradients in the cluster, and, therefore, suggested that the cluster is out of equilibrium. Sodré et al. also found a substructure towards the north-west of the cluster with a very different galaxy dispersion ($\sim$381 km s^{-1}) and without any X-ray

emission. The subcluster was also detected by Ramella et al. (2007) in the galaxy velocity distribution maps. In the X-ray image of the cluster (Figure 1(g)), we do not see any X-ray emission from this subcluster. It seems that the cluster has had a past merger with the optical group towards the northwest and, as a result of it, is now out of dynamical equilibrium.

A1377: X-ray emission is detected (significance$\geq 3\sigma$) up to a radius of about $470''$ ($\sim$0.47 Mpc $\sim R_{200}/3$) in this cluster (see Figure 3). In its X-ray image (Figure 1(i)), the cluster shows a highly irregular X-ray emission. A zoomed-in image of the central part of the cluster shows several weak peaks (see Figure 2(g)). Three of the brightest peaks are marked as 1, 2 and 3 in decreasing order of brightness. Peak 1 is brighter than its immediate surrounding at a significance level of greater than $\sim 5\sigma$, whereas peaks 2 and 3 are brighter than their immediate surroundings at a significance level of greater than $\sim 3\sigma$. The apparent spatial extents of peaks 1, 2 and 3 are $\sim 54'' \times 48''$, $\sim 66'' \times 44''$ and $\sim 54'' \times 48''$, respectively. Thus, all the peaks are significantly larger than the width of smoothing Gaussian kernel used in Figure 1(i) ($= 8''$). The 1-2, 2-3 and 1-3 peak separations are about $43''$, $67''$ and $90''$ ($\sim$43 kpc, 67 kpc and 90 kpc), respectively. In its optical image (Figure 2(h)), the BCG is found coinciding with the second brightest X-ray peak (peak 2), although shifted towards the south by about $10''$ ($\sim$10 kpc). Quite intriguingly, the brightest peak 1 does not seem to have an optical counterpart. The cluster has the lowest X-ray temperature (kT$= 1.7 \pm 0.2$ keV) and the lowest bolometric X-ray luminosity ($L_X^{bol} = (1.05 \pm 0.03) \times 10^{43}$ ergs s^{-1}) in the entire sample (Tables 3 and 4). The cluster also has the lowest value of the average elemental abundance A1377 ($= 0.09 \pm 0.04$ times the solar value), which is significantly lower than the typical values observed for clusters ($\sim$0.3 times the solar value). This indicates that the ICM of the cluster has not been processed sufficiently. A1377, therefore, seems to be a young unrelaxed cluster, which is

consistent with its extremely irregular morphology. The temperature map (Figure 9(e)) of the cluster shows an irregular distribution and the average temperature of the western parts ($kT_{west} = 2.0 \pm 0.2$ keV) seems to be slightly lower than the average temperature of the eastern parts ($kT_{east} = 2.4 \pm 0.4$ keV), although due to the large errors the difference is not significant. Unlike all the other clusters of the sample, A1377 shows anisotropic and irregular density, entropy and pressure distributions (Figures 10(e), 11(e) and 12(e), respectively).

A1831B: The cluster A1831, is a visual superposition of the two clusters, A1831A and A1831B, located along very close line-of-sights, but at very different average redshifts ($cz \sim 18870$ km s^{-1} and 22629 km s^{-1}, respectively) (Kopylov & Kopylova 2010). Kopylov & Kopylova (2010) found that A1831B is a much richer cluster than A1831A, the latter being a poor foreground cluster. They also found that the X-ray emission from this region is associated with A1831B. We detected significant X-ray emission ($\geq 3\sigma$) from A1831B up to a radius of about $360''$ ($\sim$0.52 Mpc $\sim R_{200}/4$; see Figure 3). In the X-ray image (Figure 1(k)), the emission from the cluster seems to be smooth, although with a significant departure from spherical symmetry. In the optical image (Figure 1(l)), the brightest galaxy in the field is found very close to the peak of the X-ray emission. The galaxy has a redshift of about $\sim$0.076 (Smith et al. 2004) (equal to the mean redshift of A1831B) and, therefore, is the BCG of A1831B. No distinguishable X-ray emission is detected from the cluster A1831A, which is located to the southwest at about a projected separation of $1'$ ($\sim$86 kpc) from A1831B (Kopylov & Kopylova 2010). The outermost X-ray contours in Figure 1(k) show an extension along the north-west. Interestingly, Ramella et al. (2007) found an optical subcluster towards the northwest of the A1831B BCG, at a projected distance of $\sim 10'$ ($\sim$860 kpc) and the same redshift. The subcluster lies just outside the FOV of *Chandra*. It seems that the extension of X-ray emission in A1831B towards the northwest is due to a possible tidal interaction of the cluster with the

NW subcluster. A shift of about 2″ (∼3 kpc) between the position of the BCG and the peak/centroid of the X-ray emission seen in Figure 1(l), suggests that the cluster is out of dynamical equilibrium. In the temperature profile of the cluster, a gradual decrease is seen from the centre outwards. However, in the temperature map of the cluster (Figure 9(f)), a higher temperature can be seen in the central region (marked as 'a', average kT= 4.3 ± 0.3 keV) and towards the east (marked as 'b', average kT= 3.9 ± 0.4 keV) as compared to the average temperature of 2.9 ± 0.3 keV seen in the outer parts of the cluster.

A2124: We have detected X-ray emission (significance$\geq 3\sigma$) extending to a radius of about 380″ (∼0.48 Mpc $\sim R_{200}/4$) in this cluster (see Figure 3). In the X-ray image of the cluster, the emission seems to be regular on large scales, but is aligned along the NW-SE direction (see Figure 1(m)). However, a zoomed-in image of the central region of the cluster shows four peaks (see Figure 2(i), the peaks are numbered from 1 to 4, in decreasing order of brightness). Peaks 1, 2, 3 and 4 are brighter than their immediate surroundings at significance levels of about 22σ, 15σ, 15σ and 11σ, respectively. The apparent spatial extents of peaks 1, 2, 3 and 4 in Figure 1(m) are $\sim 38'' \times 38''$, $\sim 28'' \times 28''$, $\sim 20'' \times 18''$ and $\sim 13'' \times 28''$, respectively. Therefore, all the peaks seem to be significantly larger than the width of the smoothing Gaussian kernel used in Figure 1(m) (=4″). The 1-2, 1-3, 1-4, 2-3, 2-4 and 3-4 peak separations are about 23″, 26″, 48″, 48″, 26″ and 75″ (∼29, 33, 60, 60, 33 and 94 kpc), respectively. The BCG in the optical image of the cluster (Figure 2(j)) is found nearest to the brightest of the X-ray peaks (peak 1), although, shifted towards the NE by about 6″ (∼7 kpc). No optical emission is seen from the other three X-ray peaks. Flin & Krywult (2006) had detected two small optical subclusters in the central part of the cluster at a scale of 129 kpc (∼1.7′). The X-ray image of the central region of the cluster (Figure 2(i)) does not show substructures at this scale, although there seems to be a connection between the optical subclusters and the multiple central X-ray peaks. The

temperature map of the cluster (Figure 9(g)) shows a high temperature in the central region (marked as 'a', average kT= $4.7^{+0.4}_{-0.3}$ keV). In general, a significantly lower temperature of $\sim 3.5 \pm 0.3$ keV is observed in the outermost parts of the map. However, a significantly higher temperature region is seen in the easternmost parts (marked as 'b', kT= $4.6^{+0.6}_{-0.5}$ keV). A small region with a higher temperature is indicated in the southeastern parts (marked as 'c', kT= $4.4^{+0.8}_{-0.6}$ keV), and a very low temperature is seen in the southwestern corner of the map (marked as 'd', kT= $1.7^{+0.6}_{-0.4}$ keV). The region, marked as 'e', lying between the high temperature regions 'a' and 'b', seems to have a lower temperature of kT= 3.9 ± 0.3 keV. The mismatch between the optical and X-ray peaks, and the high temperature regions in the centre of the cluster suggest ongoing mergers between the central galaxies. The X-ray peaks can, therefore, be related to the displaced X-ray halos of the central galaxies of the cluster.

A2457: X-ray emission is detected (significance$\geq 3\sigma$) up to a radius of about $360''$ ($\sim$0.41 Mpc $\sim R_{200}/3$) in this cluster (see Figure 3). The large scale X-ray emission of the cluster seems to be regular and aligned along the E-W direction (see Figure 1(o)). However, X-ray image of the central region of the cluster (Figure 2(k)) shows the central X-ray morphology of the cluster to be highly irregular. Multiple peaks are seen in the central region of the cluster, four of which have been numbered as 1 to 4 in Figure 2(k), in a decreasing order of brightness. The peaks 1, 2, 3 and 4 are brighter than their immediate surroundings at significance levels of more than 17σ, 17σ, 17σ and 12σ, respectively. The spatial extents of peaks 1, 2, 3 and 4 are $\sim 13'' \times 19''$, $\sim 13'' \times 13''$, $\sim 45'' \times 26''$ and $\sim 19'' \times 21''$, respectively. Therefore, all the peaks are found to be significantly larger than the width of smoothing Gaussian kernel used in Figure 1(o) ($=4''$). However, due to their close proximity peaks 1 and 2 are not well separated and the boundaries are not well defined. The two peaks could either be separate peaks or a single broader peanut shaped

bright region. The peak separations 1-2, 1-3, 1-4, 2-3, 2-4 and 3-4 are about 12″, 20″, 28″, 21″, 28″ and 41″ (14, 23, 32, 24, 32 and 47 kpc), respectively. The BCG in the optical image of the cluster (Figure 2(l)), is located in between the two brightest X-ray peaks 1 and 2, and is separated from them by about 6″ and 8″ (7 kpc and 9 kpc), respectively. The other two X-ray peaks do not seem to have an optical counterpart. Flin & Krywult (2006) found a group of galaxies in the centre of the cluster at a scale of 129 kpc (∼1.9′). Therefore, the multiple X-ray peaks seen in A2457 seem to be connected with the hot gas of the galaxy group. In its temperature profile, A2457 shows a drop in its innermost annulus followed by an isothermal profile outwards. The cluster seems to host a (weak) cool-core. The temperature map of the cluster (Figure 9(h)), however, shows a higher temperature region in the central and eastern parts (marked as 'a', average kT= 4.0 ± 0.2 keV) relative to the regions seen in the northern, western and southern parts of the cluster (average kT= 2.8 ± 0.2 keV). The high temperature region has a large spatial extent and seems to be an indication of the central group of galaxies having merged with the rest of the cluster.

A2665: Significant ($\geq 3\sigma$) X-ray emission extends to a radius of about 400″ (∼0.43 Mpc) in this cluster (see Figure 3). The X-ray image of the cluster (Figure 2(q)) shows that the emission in its central region is aligned along the NE-SW direction and the central X-ray contours are compressed along the SE. The BCG in the optical image of the cluster (Figure 2(r)) is slightly shifted (by about 7″ ∼8 kpc) towards the NW with respect to centroid of the innermost X-ray contours. The cluster has an average X-ray temperature of 4.4±0.2 keV and a high elemental abundance of $= 0.5 \pm 0.1$ times the solar value. The thermodynamic maps of the cluster show only slightly lower temperature and entropy in the central region (marked as 'a', average $kT_1 = 4.1 \pm 0.2$ keV, average S= 106 ± 6 keV cm^2), as compared to the somewhat higher temperature and higher entropy regions seen in the outer parts of the cluster, towards the south (marked as 'b', kT= $4.6^{+0.8}_{-0.7}$ keV, S= 158^{+28}_{-25} keV cm^2) and

east (marked as 'c', kT= $4.6^{+0.8}_{-0.6}$ keV, S= 155^{+28}_{-22} keV cm^2; see Figures 9(i) and 11(i)). The temperature difference, however, does not seem to be significant due to large measurement errors. The cluster is not well studied, therefore, little information is available in the literature.

A3822: In this cluster, we detected significant X-ray emission (significance$\geq 3\sigma$) up to a radius of 430″ ($\sim$0.62 Mpc, see Figure 3), which is about one-fourth of the virial radius (R_{200}) of the cluster. The innermost contours in the X-ray image of A3822 (Figure 1(s)) show an elongation towards the North and a contraction along the South. Also, the BCG in the optical image of the cluster (Figure 1(t)) seems to be slightly shifted ($\sim$10″ $\sim$14 kpc) from the X-ray peak southwards. The cluster is found to have the highest average X-ray temperature of 5.3 ± 0.3 keV and the highest bolometric X-ray luminosity of $(40.4 \pm 1.2) \times 10^{43}$ ergs s^{-1}, in the entire sample (see Tables 3 and 4). The thermodynamic maps of the cluster show an average temperature of 4.7 ± 0.2 keV and entropy of 150 ± 10 keV cm^2 in the central region (marked as 'a'). Although higher temperature (average kT= $5.4^{+1.9}_{-1.2}$ keV) and higher entropy (average S= 456^{+168}_{-106} keV cm^2) values are measured towards the northern part (marked as 'b' in Figures 9(j) and 11(j)), the difference is not statistically significant. A higher temperature region (marked as 'c', kT= $6.0^{+1.3}_{-0.9}$ keV) is also indicated at a distance of about 2′ ($\sim$170 kpc) towards the southwest from the centre of the cluster. Very little information is available on A3822 in the literature.

5. Summary

We have presented a detailed study of a sample of ten low-redshift clusters of galaxies with optical substructures, using their *Chandra* X-ray observations. X-ray images of all the clusters of the sample (except A1831, A2665 and A3822) exhibit significant sub-structures,

especially in their central regions. Multiple central X-ray intensity peaks are detected in six clusters viz. A193, A376, A539, A1377, A2124 and A2457. A total of 22 peaks are detected, of which eleven are found to have optical galaxy counterparts (10 coincident with the BCGs of the clusters and one coincident with the second brightest galaxy of A539). All the peaks are found to be brighter (significance$>3\sigma$) than their immediate surroundings and are well resolved even after taking into account the smoothing kernels used. In the thermodynamic maps, three peaks (one in A376 and two in A539) are found to be significantly colder than their immediate surroundings. For A539 for which both the cold peaks are found to have optical galaxy counterparts, the peaks seem to be due to the cold gas stripped off from the two galaxies, as a result of interactions between them. In the absence of high temperature regions between the two peaks, ongoing mergers between the two galaxies cannot be established. However, to rule out the mergers completely, higher resolution temperature maps are required. For the secondary peak in A376, with significantly lower temperature and lower entropy than its surroundings, no counterpart is seen in the optical image. Therefore, the peak seems to be due to a remnant of a cool core of a subcluster that has already merged with the main cluster. The X-ray morphology of A970 is found to be azimuthally asymmetric and its temperature map seems to be bimodal. The cluster seems to be out of dynamical equilibrium which is probably due to a past merger with the optical subcluster in the northwest. The cluster A1831B seems to be tidally interacting with a subcluster towards the northwest. The values of average X-ray temperature and bolometric X-ray luminosity are found to be maximum for A3822 and minimum for A1377. A1377 is found to have the most irregular X-ray morphology and thermodynamic maps, and has the smallest value of average elemental abundance in the entire sample. The cluster, therefore, seems to be the youngest cluster of the sample. The asymmetric thermodynamic maps and presence of small significantly higher temperature regions in various parts of at least five of the ten clusters (A193, A376, A1831, A2124 and A3822) suggest the possibility of galaxy

scale mergers in them. The non-detection of substructures in the X-ray intensity maps coinciding with the hotter regions (that would have confirmed the presence of a shocked gas), however, raises some doubts regarding the reality of these features. A better and more significant detection of the substructures and variations in thermodynamic maps will require much deeper *Chandra* observations of the clusters. The profiles of X-ray surface-brightness show very good fits with the double-β model for all the clusters (except A1377), thereby indicating the presence of a (weak) cool core in them. From their cooling time estimates none of the clusters seems to have a strong cool core in it, although presence of weak cool cores in some of the clusters cannot be ruled out. The bolometric X-ray luminosities and the average X-ray temperature of all the clusters of our sample are found to be consistent with the L_X-kT relation of clusters obtained by Takey et al. (2013).

6. Acknowledgements

The X-ray data used in this research have been obtained from the High Energy Astrophysics Science Archive Research Center (HEASARC), provided by NASA's Goddard Space Flight Center. We have used observations done with the *Chandra* X-ray Observatory, managed by NASA's Marshall Center.

REFERENCES

Anders, E., & Ebihara, M. 1982, Geochim. Cosmochim. Acta, 46, 2363

Anders, E., & Grevesse, N. 1989, Geochim. Cosmochim. Acta, 53, 197

Burgett, W. S., Vick, M. M., Davis, D. S., et al. 2004, MNRAS, 352, 605

Cavagnolo, K. W., Donahue, M., Voit, G. M., & Sun, M. 2009, ApJS, 182, 12

Domainko, W., Kapferer, W., Schindler, S., et al. 2005, Advances in Space Research, 36, 685

Donnelly, R. H., Forman, W., Jones, C., et al. 2001, ApJ, 562, 254

Dressler, A., & Shectman, S. A. 1988, AJ, 95, 985

Ehlert, S., Allen, S. W., von der Linden, A., et al. 2011, MNRAS, 411, 1641

Fabian, A. C. 1994, ARA&A, 32, 277

Flin, P., & Krywult, J. 2006, A&A, 450, 9

Forman, W., & Jones, C. 1982, ARA&A, 20, 547

Forman, W., & Jones, C. 1990, in Clusters of Galaxies, ed. W. R. Oegerle, J. Fitchett, & L. Danly, 257

Fukazawa, Y., Ohashi, T., Fabian, A. C., et al. 1994, PASJ, 46, L55

Geller, M. J., & Beers, T. C. 1982, PASP, 94, 421

Girardi, M., Escalera, E., Fadda, D., et al. 1997, ApJ, 482, 41

Gitti, M., O'Sullivan, E., Giacintucci, S., et al. 2010, ApJ, 714, 758

Gu, L., Xu, H., Gu, J., et al. 2012, ApJ, 749, 186

Gu, L.-Y., Wang, Y., Gu, J.-H., et al. 2010, Research in Astronomy and Astrophysics, 10, 1005

Henry, J. P., Finoguenov, A., & Briel, U. G. 2004, ApJ, 615, 181

Jones, C., & Forman, W. 1992, in NATO ASIC Proc. 366: Clusters and Superclusters of Galaxies, ed. A. C. Fabian, 49

Jones, C., & Forman, W. 1999, ApJ, 511, 65

Kalberla, P. M. W., Burton, W. B., Hartmann, D., et al. 2005, A&A, 440, 775

Kellogg, E., Gursky, H., Tananbaum, H., Giacconi, R., & Pounds, K. 1972, ApJ, 174, L65

Kempner, J. C., Sarazin, C. L., & Ricker, P. M. 2002, ApJ, 579, 236

Kopylov, A. I., & Kopylova, F. G. 2010, Astrophysical Bulletin, 65, 205

Kopylova, F. G., & Kopylov, A. I. 2006, Astronomy Letters, 32, 84

Kriessler, J. R., & Beers, T. C. 1997, AJ, 113, 80

Lakhchaura, K., Singh, K. P., Saikia, D. J., & Hunstead, R. W. 2011, ApJ, 743, 78

—. 2013, ApJ, 767, 91

Ma, C.-J., Owers, M., Nulsen, P. E. J., et al. 2012, ApJ, 752, 139

Makishima, K., Ezawa, H., Fukuzawa, Y., et al. 2001, PASJ, 53, 401

Markevitch, M., & Vikhlinin, A. 2007, Phys. Rep., 443, 1

Maurogordato, S., Sauvageot, J. L., Bourdin, H., et al. 2011, A&A, 525, A79

McNamara, B. R., & Nulsen, P. E. J. 2007, ARA&A, 45, 117

Mitchell, R. J., Dickens, R. J., Burnell, S. J. B., & Culhane, J. L. 1979, MNRAS, 189, 329

Morrison, R., & McCammon, D. 1983, ApJ, 270, 119

Ostriker, E. C., Huchra, J. P., Geller, M. J., & Kurtz, M. J. 1988, AJ, 96, 1775

Owers, M. S., Randall, S. W., Nulsen, P. E. J., et al. 2011, ApJ, 728, 27

Proust, D., Capelato, H. V., Hickel, G., et al. 2003, A&A, 407, 31

Proust, D., Capelato, H. V., Lima Neto, G. B., & Sodré, L. 2010, A&A, 515, A57

Ramella, M., Biviano, A., Pisani, A., et al. 2007, A&A, 470, 39

Reiprich, T. H. 2001, PhD thesis, Max-Planck-Institut für extraterrestrische Physik, P.O. Box 1312, Garching bei München, Germany

Roettiger, K., Burns, J. O., & Loken, C. 1996, ApJ, 473, 651

Rosati, P., Borgani, S., & Norman, C. 2002, ARA&A, 40, 539

Sarazin, C. L. 1988, X-ray emission from clusters of galaxies

Schuecker, P., Böhringer, H., Reiprich, T. H., & Feretti, L. 2001, A&A, 378, 408

Seigar, M. S., Lynam, P. D., & Chorney, N. E. 2003, MNRAS, 344, 110

Smith, R. J., Hudson, M. J., Nelan, J. E., et al. 2004, AJ, 128, 1558

Smith, R. K., Brickhouse, N. S., Liedahl, D. A., & Raymond, J. C. 2001, ApJ, 556, L91

Sodré, Jr., L., Proust, D., Capelato, H. V., et al. 2001, A&A, 377, 428

Takahashi, I., Kawaharada, M., Makishima, K., et al. 2009, ApJ, 701, 377

Takey, A., Schwope, A., & Lamer, G. 2013, A&A, 558, A75

Vulcani, B., Poggianti, B. M., Dressler, A., et al. 2011, MNRAS, 413, 921

This manuscript was prepared with the AAS LaTeX macros v5.2.

Table 1: Redshifts and positions (α (J2000), δ (J2000)) of the ten clusters of the sample along with the details (observation ID, date of observations ad exposure time) of their *Chandra* observations.

Cluster	Redshift	α (J2000)	δ (J2000)	Observation ID	Date of Observation	Exposure Time (ks)
A193	0.0490	01 25 07.3	08 41 36.0	6931	2005 Nov 10	18.2
A376	0.0475	02 45 48.0	36 51 36.0	12277	2010 Nov 07	10.6
A539	0.0284	05 16 35.1	06 27 14.0	5808	2005 Nov 18	24.6
				7209	2005 Nov 20	18.8
A970	0.0588	10 17 34.3	-10 42 01.0	12285	2011 Feb 04	10.1
A1377	0.0514	11 47 15.7	55 43 01.6	6943	2006 Sep 08	44.1
A1831B	0.0755	13 59 15.1	27 58 34.5	12283	2011 Apr 19	10.1
A2124	0.0654	15 44 59.3	36 03 40.0	3238	2002 May 20	19.6
A2457	0.0591	22 35 40.3	01 31 33.6	12276	2011 Jan 12	10.1
A2665	0.0556	23 50 50.6	06 09 00.0	12280	2011 Jan 17	10.1
A3822	0.0760	21 54 06.2	-57 50 49	8269	2007 Mar 14	8.2

Table 2: Results obtained from the double-β model fitting of the X-ray surface brightness profiles of the clusters, as described in §3.2. Here, S_{01} and S_{02} are the peak surface brightness, and r_{c1} and r_{c2} are the corresponding core radii of the two components of the double-β model. Values of the index β (assumed same for both the components) are also given. For A1377, results of the single-β model fitting are given. The values of the reduced chi-square minimum $(\chi^2_\nu)_{min}$ and the degrees of freedom of each fit are also given.

Cluster	S_{01} (10^{-5} counts s^{-1} $arcsec^{-2}$)	S_{02} (10^{-5} counts s^{-1} $arcsec^{-2}$)	r_{c1} (kpc)	r_{c2} (kpc)	β ($= \beta 1 = \beta 2$)	$(\chi^2_\nu)_{min}$ (DOF)
A193	3.3±0.4	4.0±0.5	64±13	192±28	0.63±0.05	1.38 (45)
A376	2.3±0.3	0.8±0.1	27±4	193±19	0.67±0.04	0.84 (55)
A539	5.9±0.6	2.3±0.1	18±2	169±8	0.48±0.01	1.28 (81)
A970	1.5±0.2	1.4±0.2	37±11	142±21	0.65±0.05	0.93 (40)
A1377	0.43±0.01	–	252±46	–	0.75±0.15	2.42 (19)
A1831B	2.8±0.2	0.8±0.1	118±28	374±89	2.20±0.70	0.86 (40)
A2124	4.7±0.3	2.5±0.2	40±5	171±16	0.70±0.04	1.59 (43)
A2457	1.9±0.3	0.7±0.1	37±8	232±39	1.10±0.20	0.48 (39)
A2665	3.1±0.3	1.5±0.1	47±7	190±22	1.10±0.10	1.45 (24)
A3822	0.9±0.3	1.6±0.1	31±12	154±14	0.76±0.05	0.95 (48)

All errors are quoted at 90% confidence level based on χ^2_{min}+2.71.

Table 3: Average spectral properties of all the clusters of the sample resulting from the analysis described in §3.3. the N_H values obtained from the LAB survey for all the clusters, are given in the second column.

Cluster	N_H	kT	Abundance	*apec* norm.	$(\chi^2_\nu)_{min}$ (DOF)
	(10^{20} cm^{-2})	(keV)	(Rel. to solar)	(10^{-3} cm^{-5})	
A193	4.29	4.0 ± 0.1	0.2 ± 0.1	10.7 ± 0.2	1.4 (40)
A376	5.49	4.8 ± 0.4	$0.3^{+0.2}_{-0.1}$	6.1 ± 0.3	0.68 (40)
A539	10.5	3.0 ± 0.1	0.19 ± 0.03	14.1 ± 0.2	1.0 (77)
A970	4.39	4.6 ± 0.3	0.2 ± 0.1	12.8 ± 0.5	1.1 (37)
A1377	0.75	1.7 ± 0.2	0.09 ± 0.04	2.1 ± 0.2	0.9 (25)
A1831B	1.38	3.9 ± 0.2	0.3 ± 0.1	8.3 ± 0.4	0.93 (40)
A2124	1.86	4.8 ± 0.3	0.3 ± 0.1	5.4 ± 0.2	1.1 (40)
A2457	5.62	3.9 ± 0.3	0.2 ± 0.1	7.7 ± 0.4	1.5 (40)
A2665	6.02	$4.4^{+0.3}_{-0.2}$	0.5 ± 0.1	8.9 ± 0.4	0.93 (40)
A3822	2.18	5.3 ± 0.3	0.2 ± 0.1	16.0 ± 0.5	1.3 (39)

All errors are quoted at 90% confidence level based on χ^2_{min}+2.71.

Table 4: Estimates of 0.5-7.0 keV X-ray luminosity (L_X), bolometric X-ray luminosity (L_{bol}) calculated within R_{200}, cooling times (t_{cool}) and gas mass ($M_{gas}(r)$) (for both r= 1 Mpc and r=R_{200}) for the cluster sample. The second column gives the R_{200} values used here and their references.

Cluster	R_{200}	L_X (0.5-7.0 keV)	L_X^{bol} (0.1-100 keV)	t_{cool}	$M_{gas}(r = 1Mpc)$	$M_{gas}(r = R_{200})$
	(Mpc)	(10^{43} erg s^{-1})	(10^{43} erg s^{-1})	(10^{10} yr)	(10^{13} $M_\odot$)	(10^{13} $M_\odot$)
A193	1.83[1]	6.64 ± 0.04	11.5 ± 0.2	1.2 ± 0.6	6.7 ± 0.7	18.5 ± 1.9
A376	2.06[1]	3.91 ± 0.05	6.8 ± 0.3	1.1 ± 0.4	6.2 ± 0.9	10.4 ± 1.5
A539	1.87[2]	3.67 ± 0.03	7.4 ± 0.2	0.8 ± 0.2	12.4 ± 1.0	40.9 ± 3.2
A970	1.84[1]	11.9 ± 0.1	18.2 ± 0.7	–	–	–
A1377	1.40[3]	0.88 ± 0.03	1.6 ± 0.1	–	–	–
A1831B	2.27[4]	12.3 ± 0.3	17.1 ± 0.5	1.0 ± 0.2	4.7 ± 0.7	21.9 ± 3.3
A2124	1.92[1]	6.4 ± 0.1	9.5 ± 0.3	1.1 ± 0.7	2.7 ± 0.3	7.6 ± 1.0
A2457	1.40[1]	6.8 ± 0.1	10.2 ± 0.5	1.5 ± 0.7	5.3 ± 1.0	12.7 ± 2.4
A2665	1.50[5]	8.0 ± 0.1	11.5 ± 0.5	1.0 ± 0.3	2.5 ± 0.3	4.1 ± 0.6
A3822	2.43[2]	25.9 ± 0.2	40.4 ± 1.2	1.2 ± 0.4	6.0 ± 0.8	30.6 ± 4.1

All errors are quoted at 90% confidence level based on χ^2_{min}+2.71.

[1] Vulcani et al. (2011), [2] Reiprich (2001), [3] Kopylova & Kopylov (2006), [4] Kopylov & Kopylova (2010),

[5] assumed.

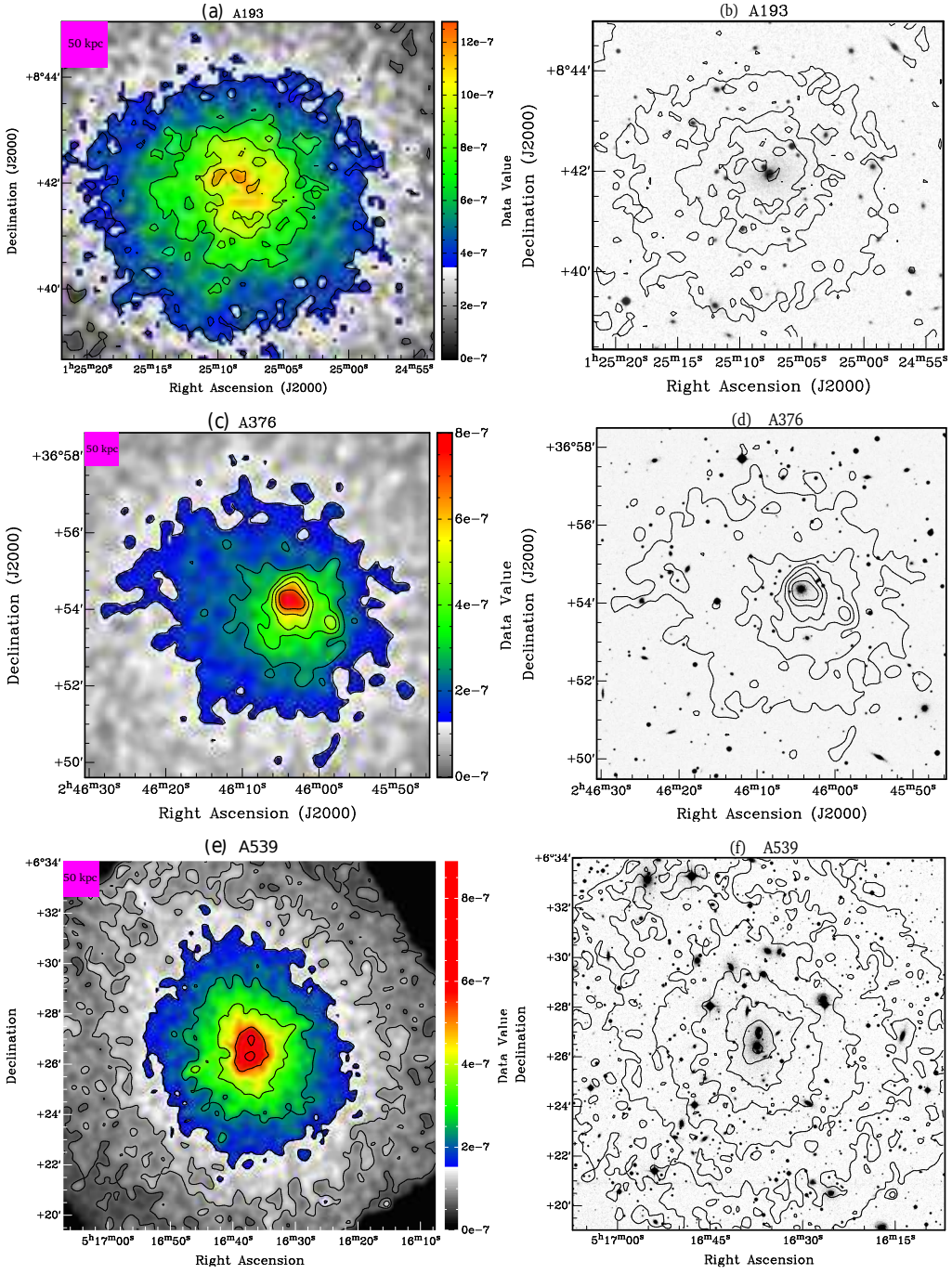
(a) A193
50 kpc
+8°44′
+42′
+40′
Declination (J2000)
1h25m20s
25m15s
25m10s
25m05s
25m00s
24m55s
Right Ascension (J2000)
12e−7
10e−7
8e−7
6e−7
4e−7
2e−7
0e−7
Data Value
(b) A193
Declination (J2000)
Right Ascension (J2000)
(c) A376
50 kpc
+36°58′
+56′
+54′
+52′
+50′
2h46m30s
46m20s
46m10s
46m00s
45m50s
8e−7
6e−7
4e−7
2e−7
0e−7
(d) A376
(e) A539
50 kpc
+6°34′
+32′
+30′
+28′
+26′
+24′
+22′
+20′
5h17m00s
16m50s
16m40s
16m30s
16m20s
16m10s
Declination
Right Ascension
(f) A539
16m45s
16m30s
16m15s

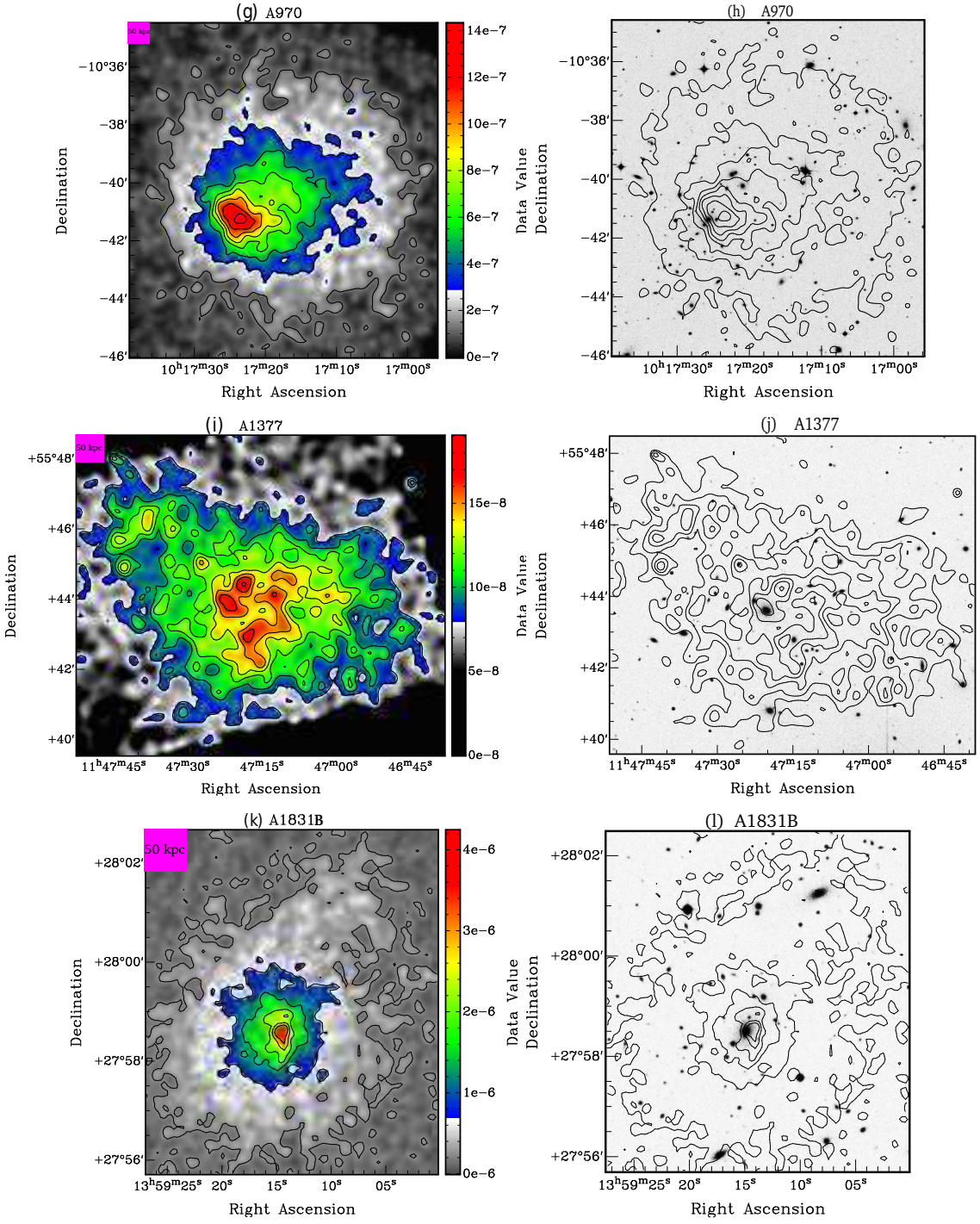
(g) A970
50 kpc
−10°36′
−38′
−40′
−42′
−44′
−46′
Declination
10h17m30s
17m20s
17m10s
17m00s
Right Ascension
14e−7
12e−7
10e−7
8e−7
6e−7
4e−7
2e−7
0e−7
(h) A970
Data Value
Declination
(i) A1377
50 kpc
+55°48′
+46′
+44′
+42′
+40′
11h47m45s
47m30s
47m15s
47m00s
46m45s
15e−8
10e−8
5e−8
0e−8
(j) A1377
(k) A1831B
50 kpc
+28°02′
+28°00′
+27°58′
+27°56′
13h59m25s
20s
15s
10s
05s
4e−6
3e−6
2e−6
1e−6
0e−6
(l) A1831B

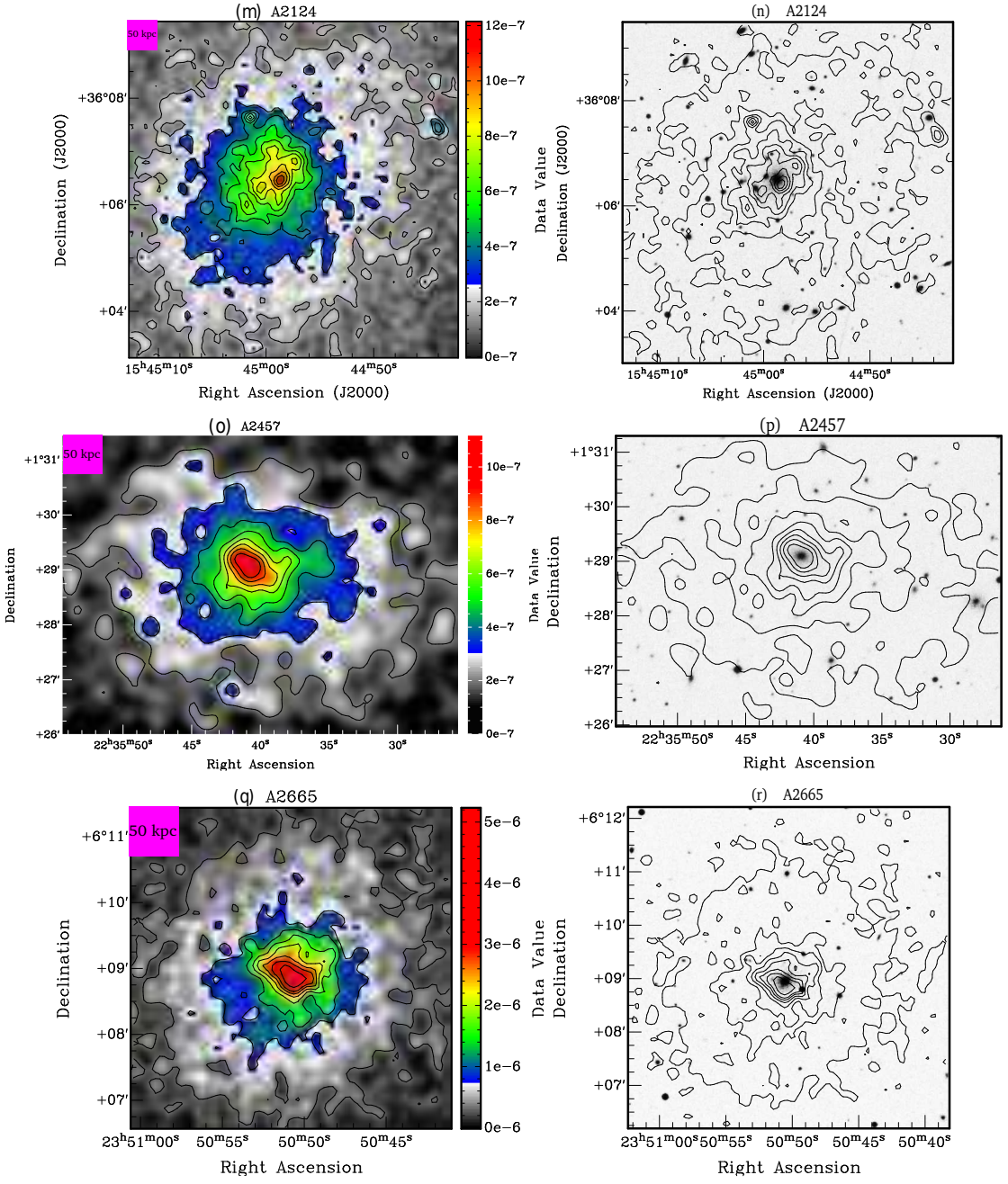
(m) A2124
50 kpc
+36°08′
+06′
+04′
Declination (J2000)
15h45m10s
45m00s
44m50s
Right Ascension (J2000)
12e−7
10e−7
8e−7
6e−7
4e−7
2e−7
0e−7
(n) A2124
Data Value
Declination (J2000)
Right Ascension (J2000)
(o) A2457
50 kpc
+1°31′
+30′
+29′
+28′
+27′
+26′
Declination
22h35m50s
45s
40s
35s
30s
Right Ascension
10e−7
8e−7
6e−7
4e−7
2e−7
0e−7
(p) A2457
Data Value
Declination
Right Ascension
(q) A2665
50 kpc
+6°11′
+10′
+09′
+08′
+07′
Declination
23h51m00s
50m55s
50m50s
50m45s
Right Ascension
5e−6
4e−6
3e−6
2e−6
1e−6
0e−6
(r) A2665
Data Value
Declination
+6°12′
+11′
+10′
+09′
+08′
+07′
23h51m00s
50m55s
50m50s
50m45s
50m40s
Right Ascension

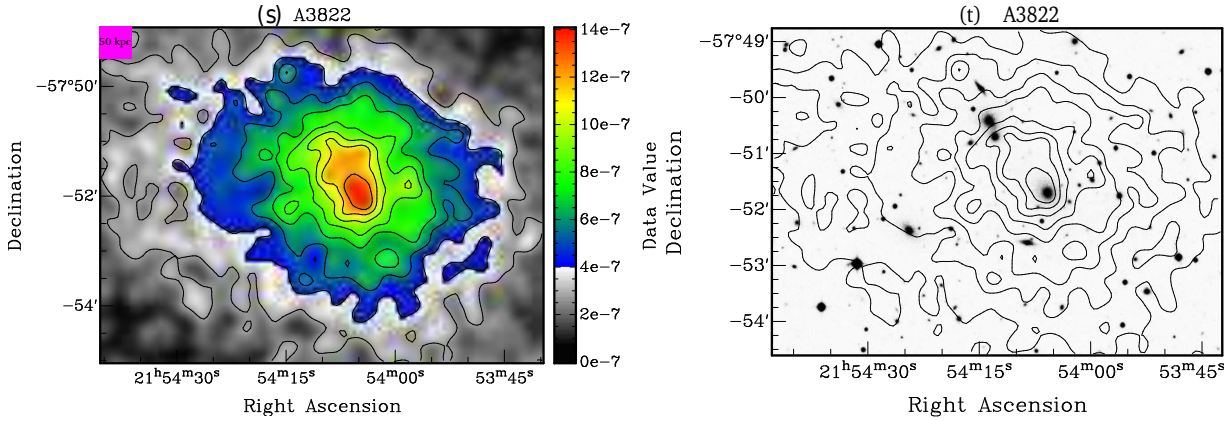

Fig. 1.— (a), (c), (e), (g), (i), (k), (m), (o), (q), and (s): *Chandra* X-ray image of the clusters A193, A376, A539, A970, A1377, A1831B, A2124, A2457, A2665, and A3822, smoothed with Gaussian kernels of width 4″, 8″, 8″, 8″, 8″, 4″, 4″, 8″, 4″, and 8″, respectively. The contour levels are distributed from 4σ to 25σ, 3σ to 28σ, 3σ to 59σ, 3σ to 60σ, 3σ to 13σ, 3σ to 78σ, 3σ to 32σ, 3σ to 42σ, 5σ to 105σ, and 3σ to 19σ above the mean background, for the clusters A193, A376, A539, A970, A1377, A1831B, A2124, A2457, A2665, and A3822, respectively. The scale is expressed in units of counts s^{-1} cm^{-2} $pixel^{-1}$. (b), (d), (f), (h), (j), (l), (n), (p), (r), and (t): Optical images of the clusters A193, A376, A539, A970, A1377, A1831B, A2124, A2457, A2665, and A3822, from the SuperCOSMOS survey overlaid with the X-ray contours from the LHS. The pink boxes on the top left corner of the images on the left side mark a 50 kpc×50 kpc region.

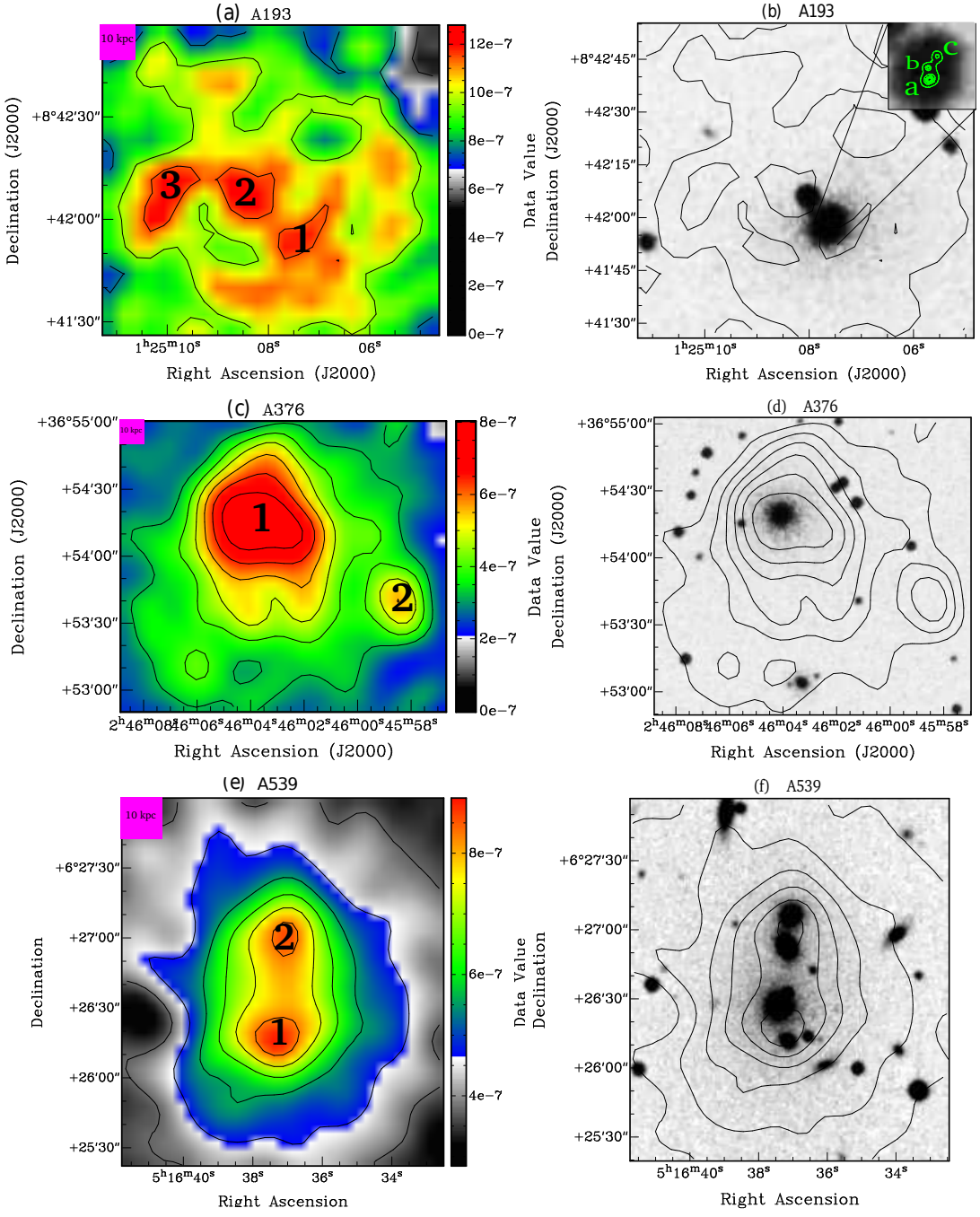
(a) A193
10 kpc
12e−7
10e−7
8e−7
6e−7
4e−7
2e−7
0e−7
3
2
1
Declination (J2000)
+8°42′30″
+42′00″
+41′30″
1h25m10s
08s
06s
Right Ascension (J2000)
(b) A193
Data Value
Declination (J2000)
+8°42′45″
+42′30″
+42′15″
+42′00″
+41′45″
+41′30″
b
c
a
1h25m10s
08s
06s
Right Ascension (J2000)
(c) A376
10 kpc
8e−7
6e−7
4e−7
2e−7
0e−7
1
2
Declination (J2000)
+36°55′00″
+54′30″
+54′00″
+53′30″
+53′00″
2h46m08s46m06s46m04s46m02s46m00s45m58s
Right Ascension (J2000)
(d) A376
Data Value
Declination (J2000)
+36°55′00″
+54′30″
+54′00″
+53′30″
+53′00″
2h46m08s46m06s 46m04s 46m02s 46m00s 45m58s
Right Ascension (J2000)
(e) A539
10 kpc
8e−7
6e−7
4e−7
2
1
Declination
+6°27′30″
+27′00″
+26′30″
+26′00″
+25′30″
5h16m40s
38s
36s
34s
Right Ascension
(f) A539
Data Value
Declination
+6°27′30″
+27′00″
+26′30″
+26′00″
+25′30″
5h16m40s
38s
36s
34s
Right Ascension

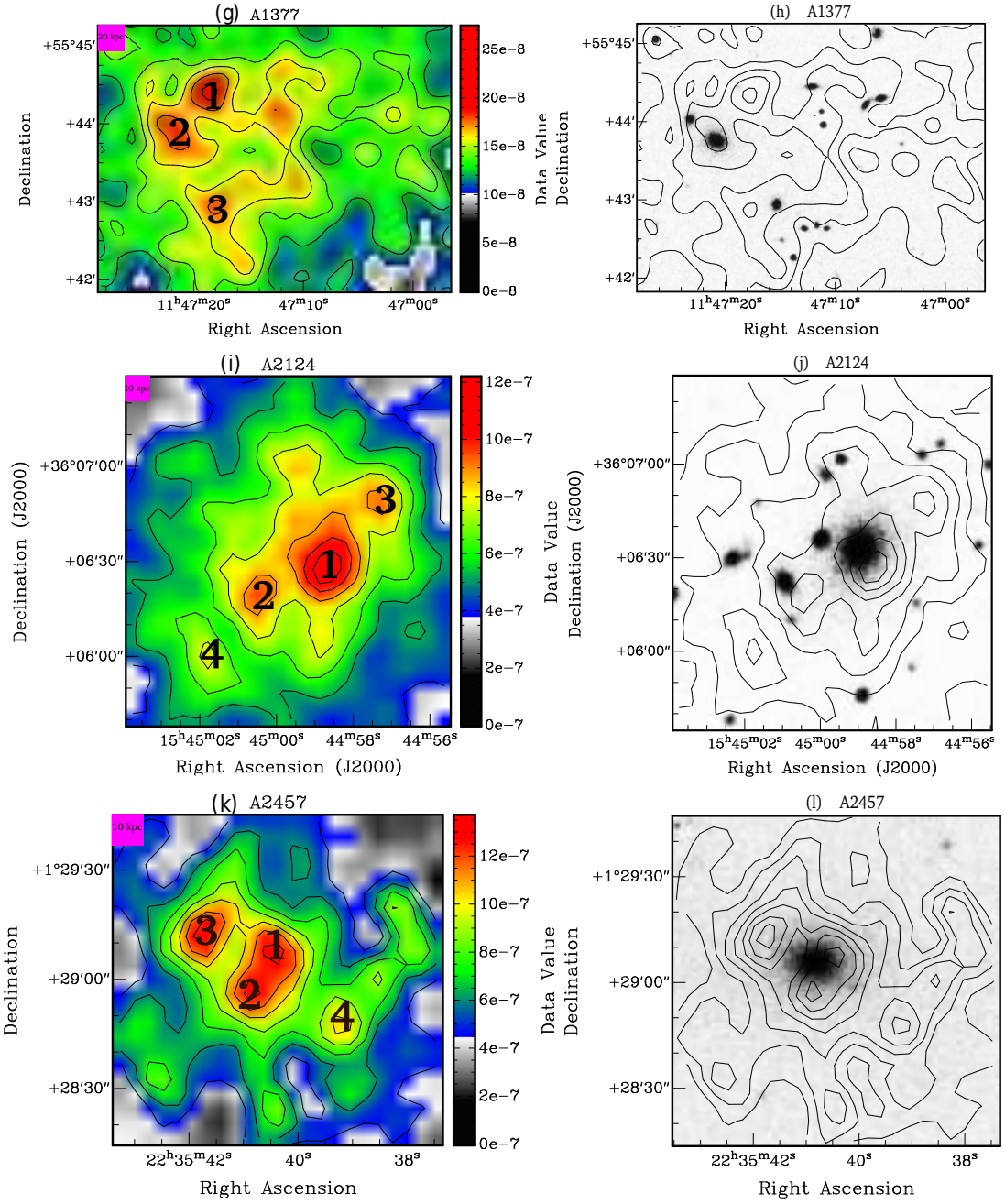

Fig. 2.— (a), (c), (e), (g), (i) and (k) : *Chandra* X-ray images of the central parts of the clusters A193, A376, A539, A1377 and A2124 and A2457, smoothed with Gaussian kernels of width 4″, 8″, 8″, 8″, 4″ and 4″ respectively. The contour levels are distributed from 12σ to 25σ, 12σ to 30σ, 11σ to 89σ, 7σ to 16σ, 10σ to 32σ and 7σ to 22σ above the mean background, for the clusters

A193, A376, A539, A1377, A2124 and A2457, respectively. The scales are expressed in units of counts s^{-1} cm^{-2} $pixel^{-1}$. (b), (d), (f), (h), (j) and (l) : Optical images of the central parts of the clusters A193, A376, A539, A1377, A2124 and A2457, respectively, from the SuperCOSMOS survey overlaid with the X-ray contours from the LHS. The pink boxes on the top left corner of the images on the left side mark a 10 kpc×10 kpc region (20 kpc×20 kpc for A1377).

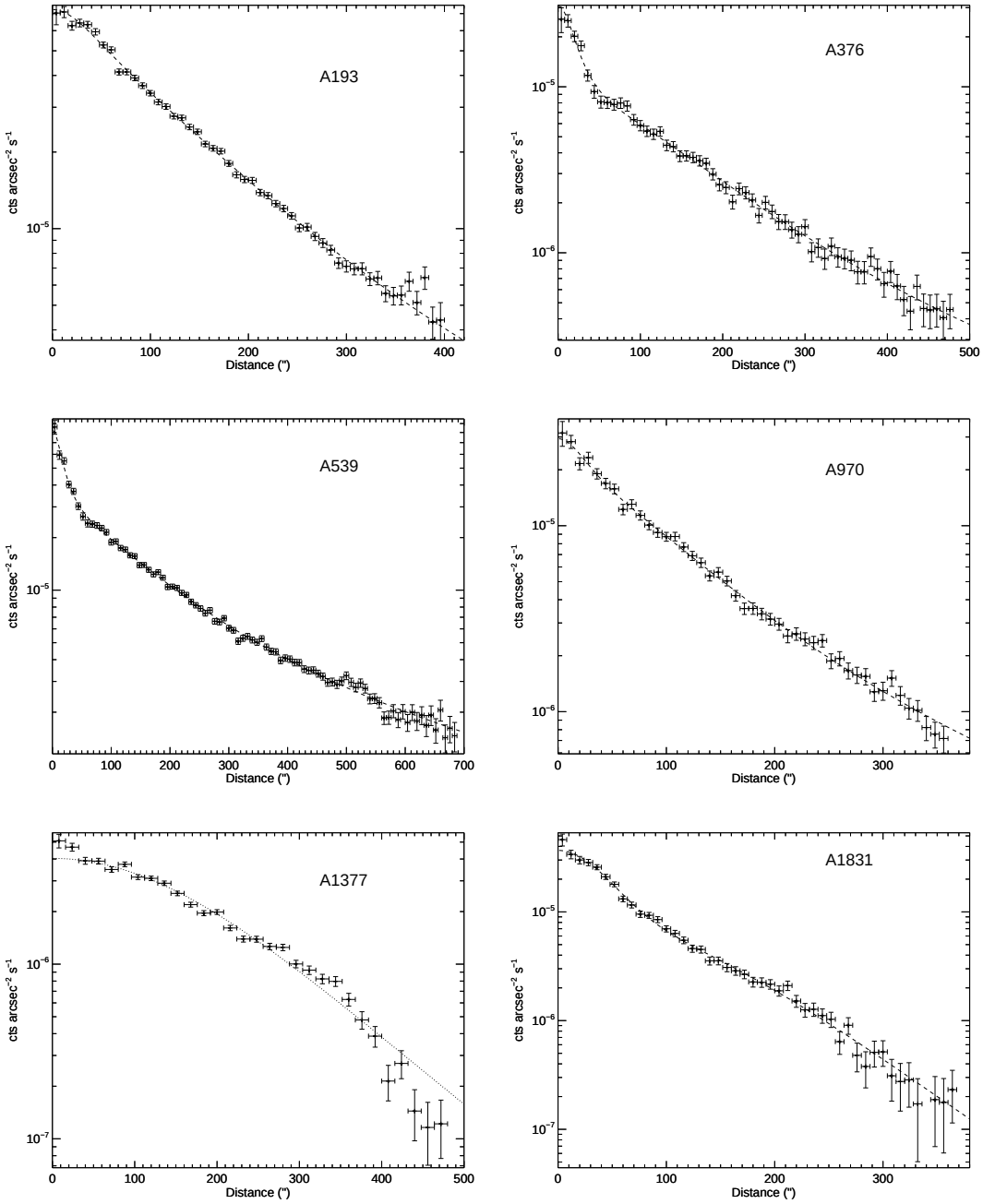
A193
A376
A539
A970
A1377
A1831
cts arcsec^{-2} s^{-1}
Distance (")

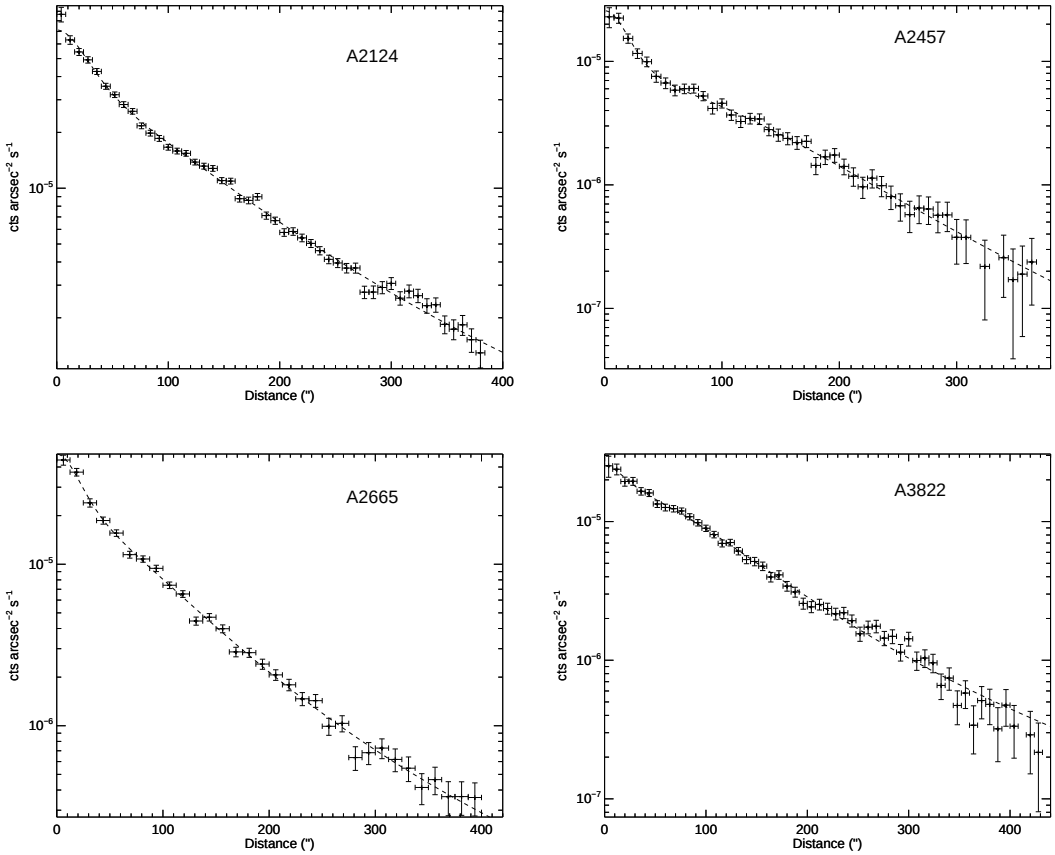

Fig. 3.— X-ray surface brightness profiles of the clusters A193, A376, A539, A970, A1831B, A2124, A2457, A2665, and A3822 fitted with double-β model (single-β for A1377), shown with the dashed line. The results of the fitting are provided in Table 2.

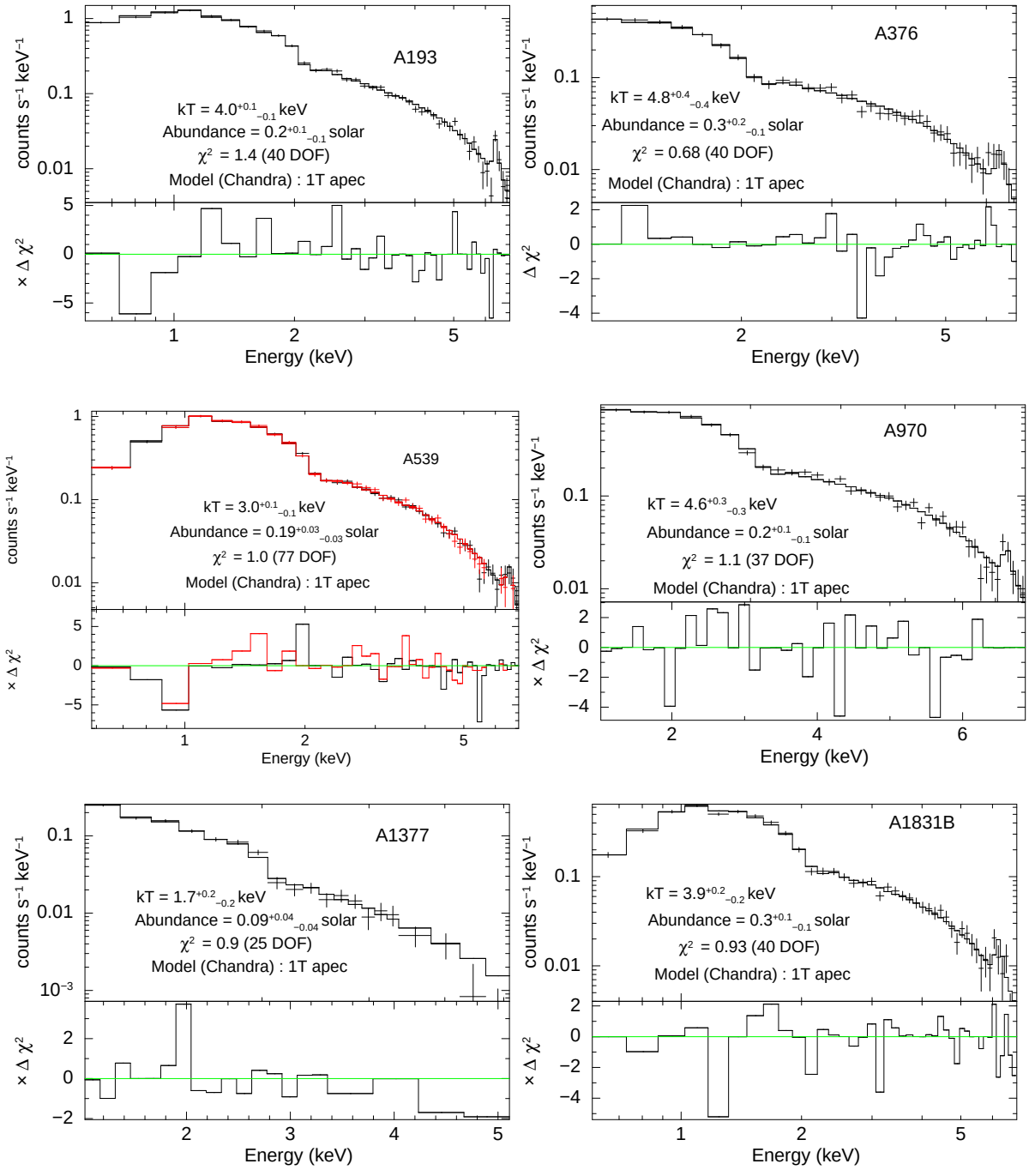
A193
kT = 4.0$^{+0.1}_{-0.1}$ keV
Abundance = 0.2$^{+0.1}_{-0.1}$ solar
χ^2 = 1.4 (40 DOF)
Model (Chandra) : 1T apec
counts s^{-1} keV^{-1}
× Δ χ^2
Energy (keV)
A376
kT = 4.8$^{+0.4}_{-0.4}$ keV
Abundance = 0.3$^{+0.2}_{-0.1}$ solar
χ^2 = 0.68 (40 DOF)
Model (Chandra) : 1T apec
Δ χ^2
Energy (keV)
A539
kT = 3.0$^{+0.1}_{-0.1}$ keV
Abundance = 0.19$^{+0.03}_{-0.03}$ solar
χ^2 = 1.0 (77 DOF)
Model (Chandra) : 1T apec
Energy (keV)
A970
kT = 4.6$^{+0.3}_{-0.3}$ keV
Abundance = 0.2$^{+0.1}_{-0.1}$ solar
χ^2 = 1.1 (37 DOF)
Model (Chandra) : 1T apec
Energy (keV)
A1377
kT = 1.7$^{+0.2}_{-0.2}$ keV
Abundance = 0.09$^{+0.04}_{-0.04}$ solar
χ^2 = 0.9 (25 DOF)
Model (Chandra) : 1T apec
Energy (keV)
A1831B
kT = 3.9$^{+0.2}_{-0.2}$ keV
Abundance = 0.3$^{+0.1}_{-0.1}$ solar
χ^2 = 0.93 (40 DOF)
Model (Chandra) : 1T apec
Energy (keV)

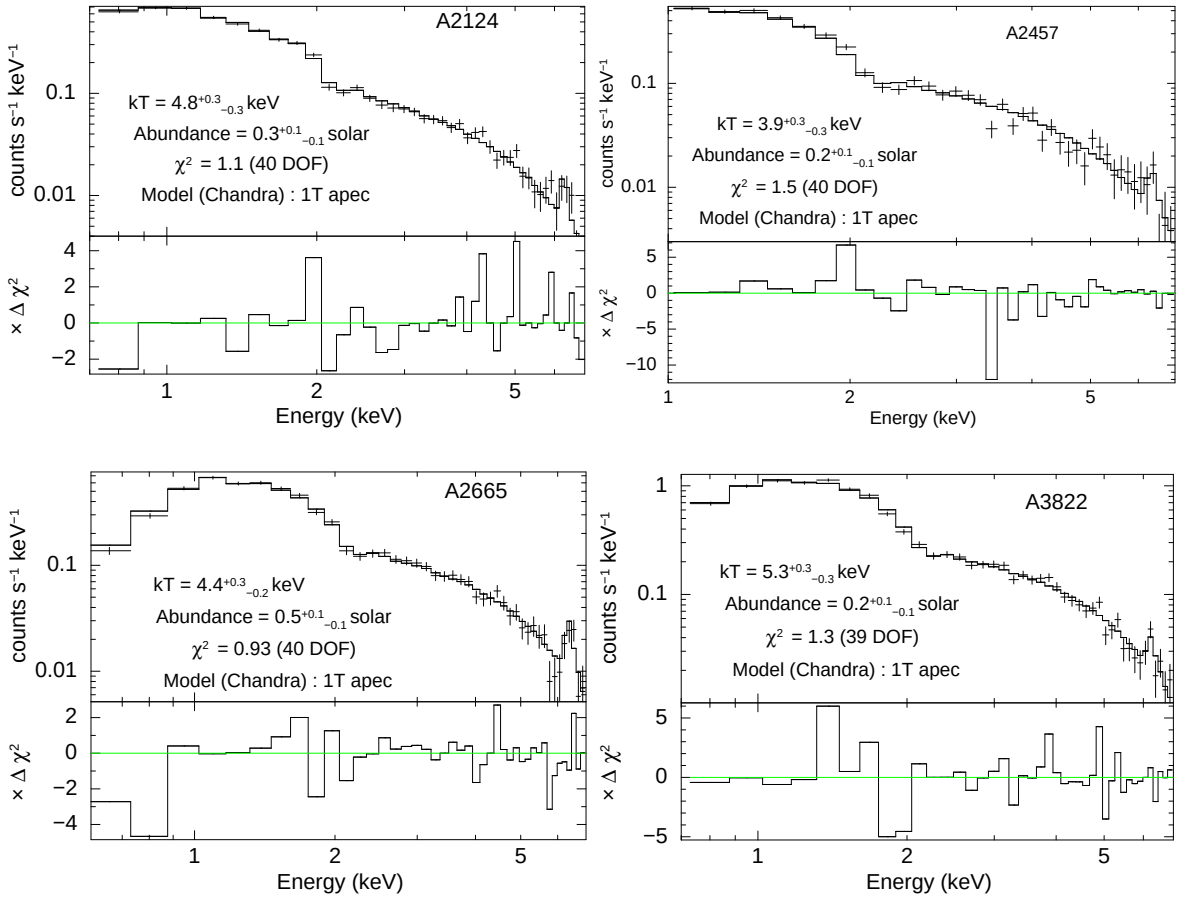

Fig. 4.— Average spectra of the clusters A193, A376, A539, A970, A1377, A1831B, A2124, A2457, A2665, and A3822 from the *Chandra ACIS* detector. All the spectra have been fitted with *wabs*apec* model shown as a histogram. Details of the spectral analysis are given in §3.3, and the best-fit parameters are shown here as insets. For A539 the two different colored spectra used correspond to the two *Chandra* observations of the cluster used in this paper.

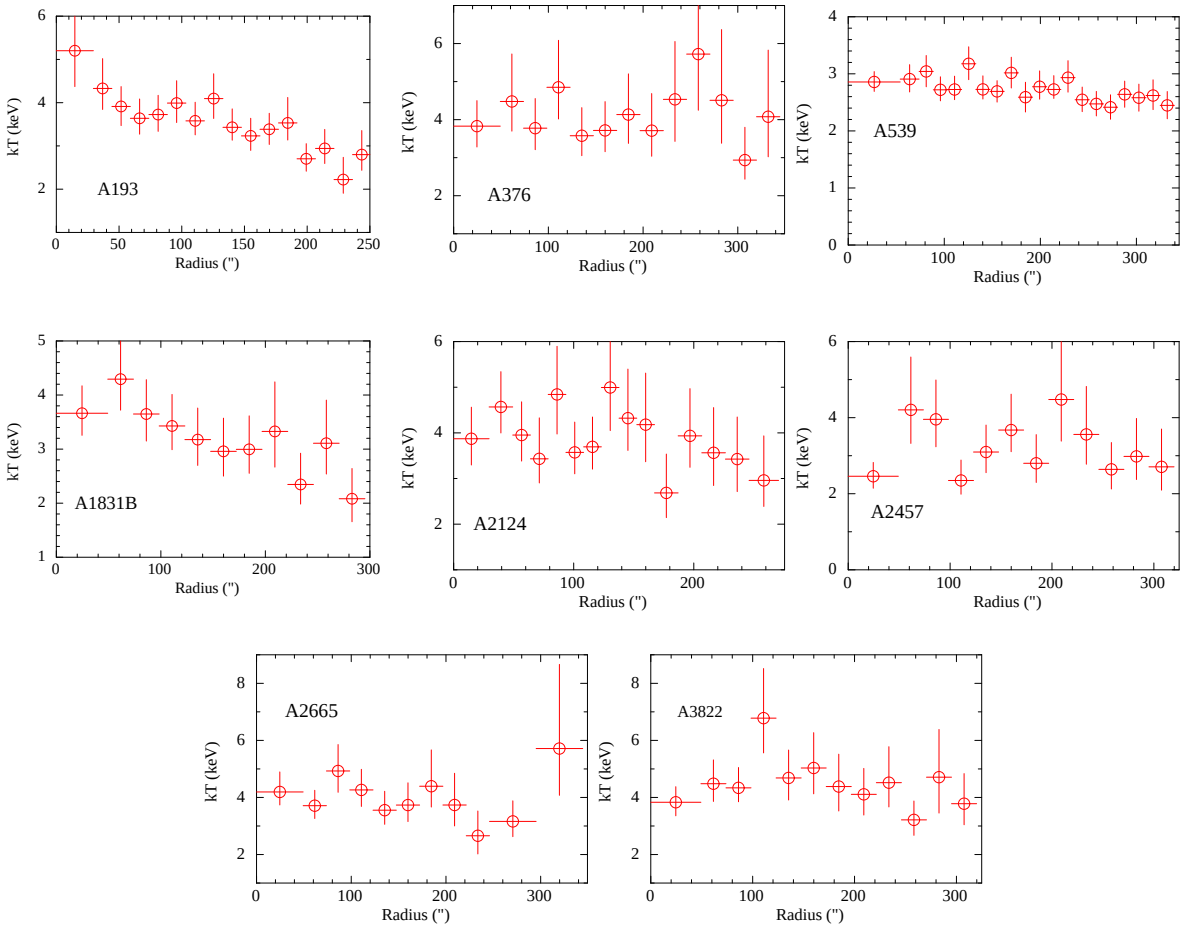

Fig. 5.— Projected temperature (kT) profiles obtained from the spectral analysis of circular annuli centred on the surface brightness peaks of the clusters A193, A376, A539, A1831B, A2124, A2457, A2665, and A3822, respectively. For each cluster, the value of elemental abundance was frozen to the average abundance obtained for the whole cluster.

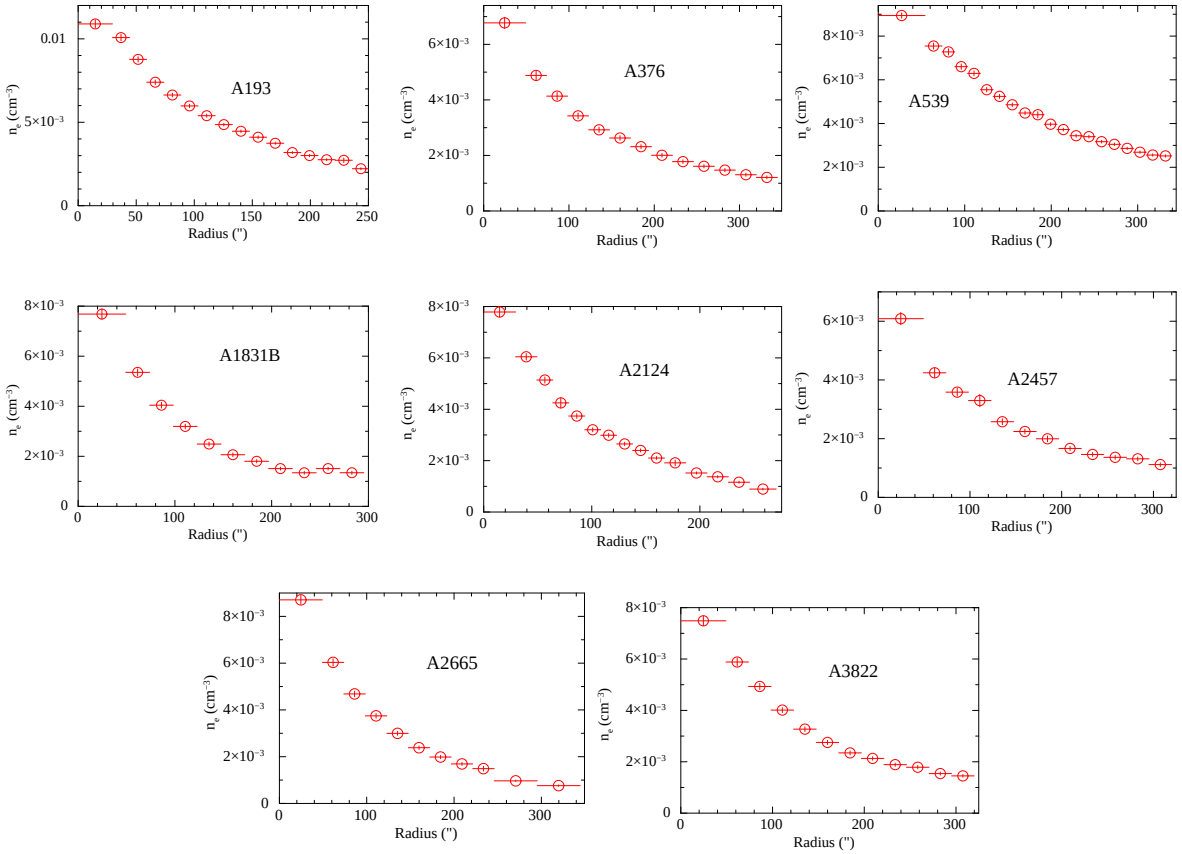

Fig. 6.— Projected electron number density (n_e) profiles of the clusters A193, A376, A539, A1831B, A2124, A2457, A2665, and A3822, respectively.

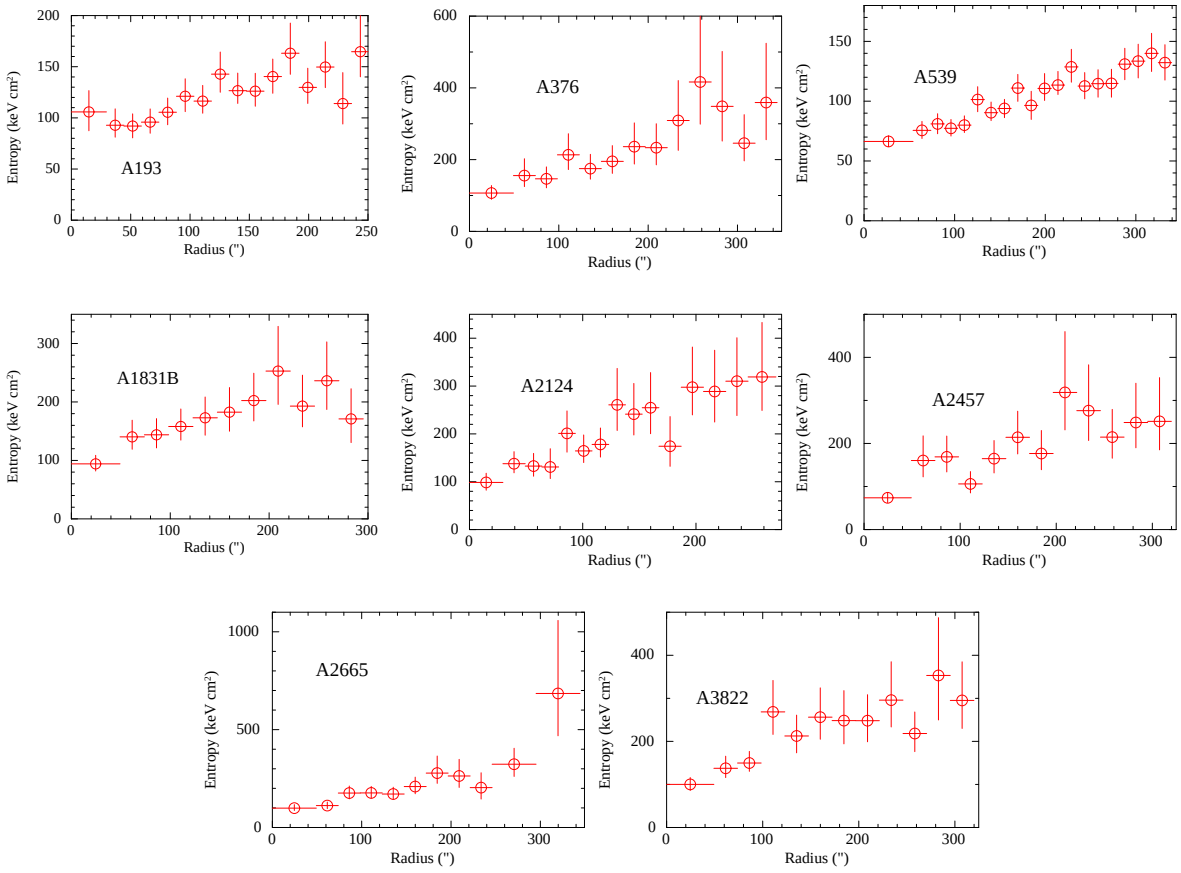

Fig. 7.— Projected entropy (S) profiles of the clusters A193, A376, A539, A1831B, A2124, A2457, A2665, and A3822, respectively.

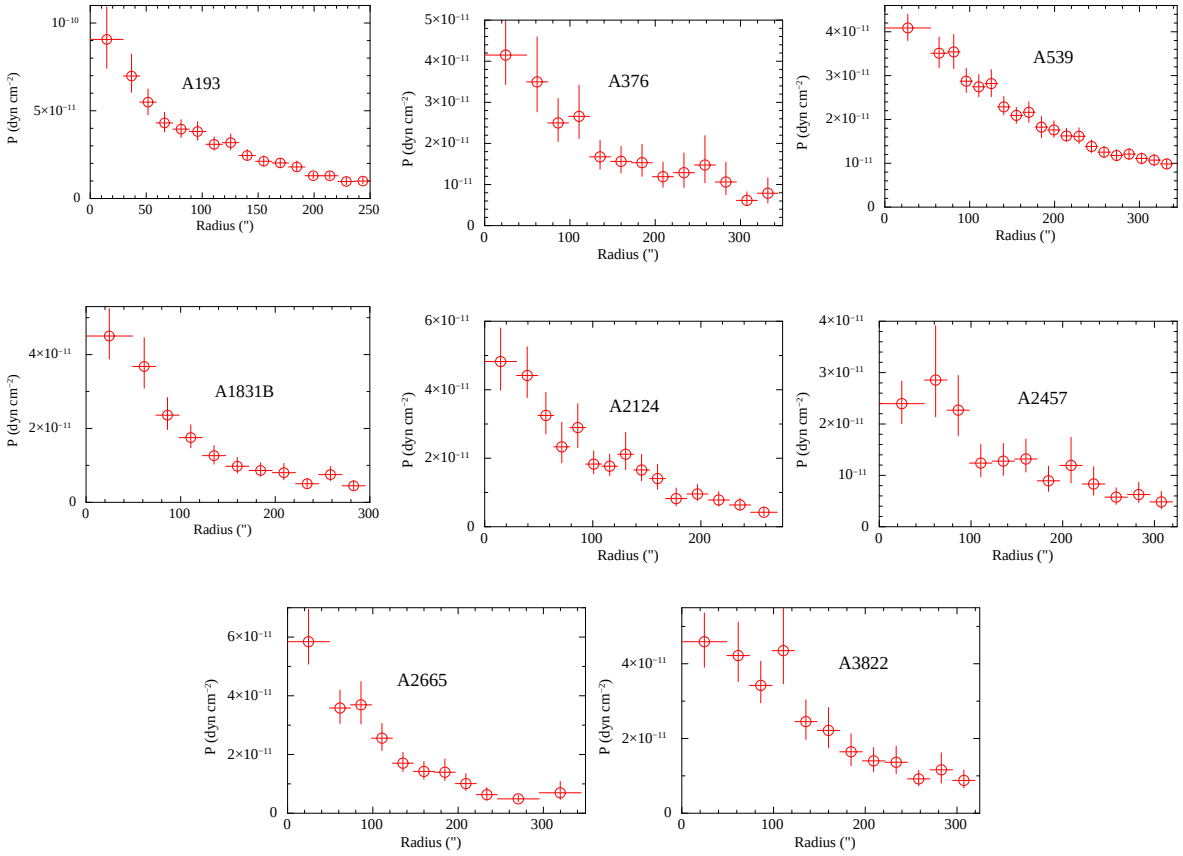

Fig. 8.— Projected pressure (P) profiles of the clusters A193, A376, A539, A1831B, A2124, A2457, A2665, and A3822, respectively.

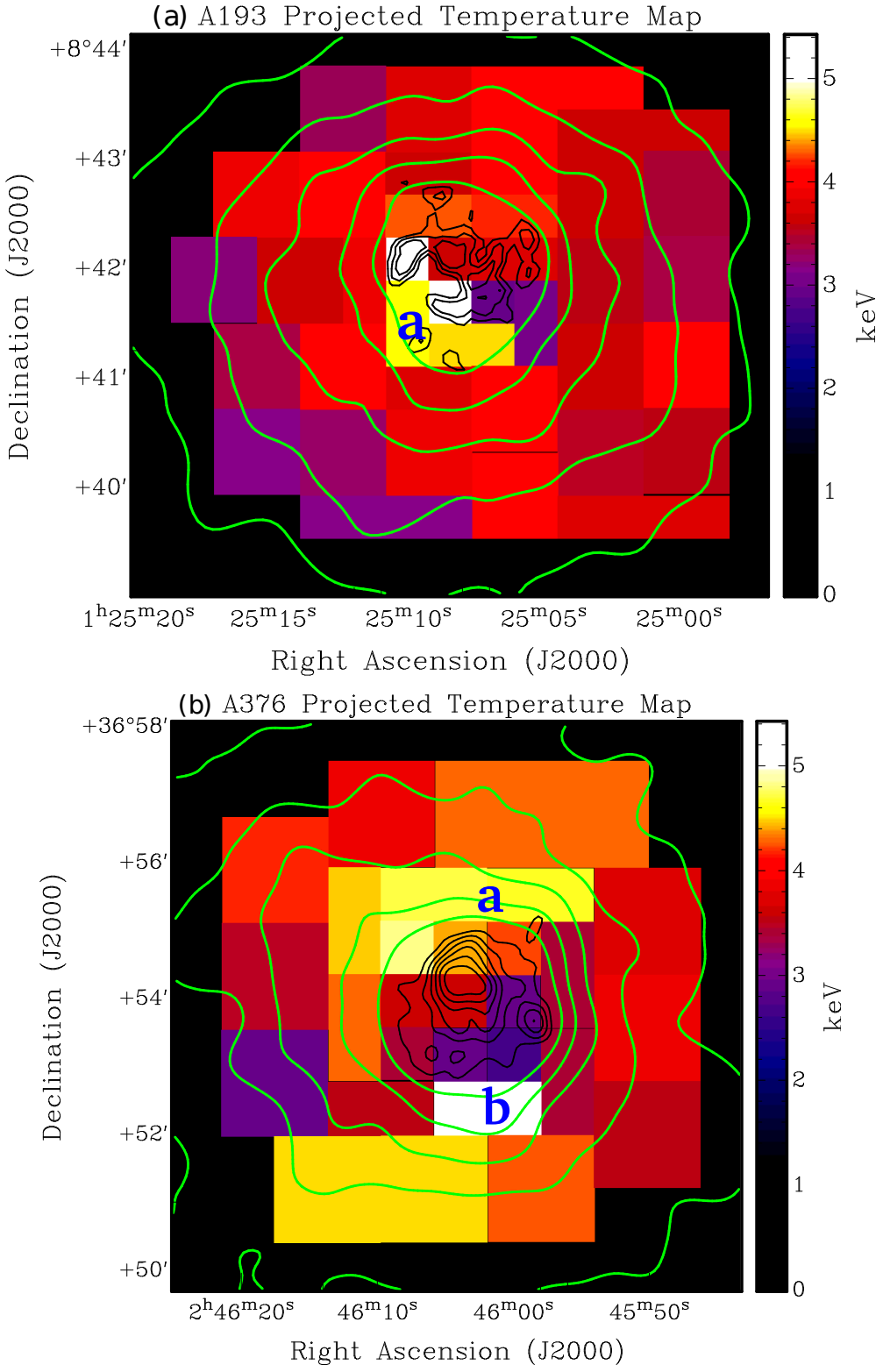
(a) A193 Projected Temperature Map
+8°44′
+43′
+42′
+41′
+40′
Declination (J2000)
a
keV
5
4
3
2
1
0
1h25m20s
25m15s
25m10s
25m05s
25m00s
Right Ascension (J2000)
(b) A376 Projected Temperature Map
+36°58′
+56′
+54′
+52′
+50′
Declination (J2000)
a
b
keV
5
4
3
2
1
0
2h46m20s
46m10s
46m00s
45m50s
Right Ascension (J2000)

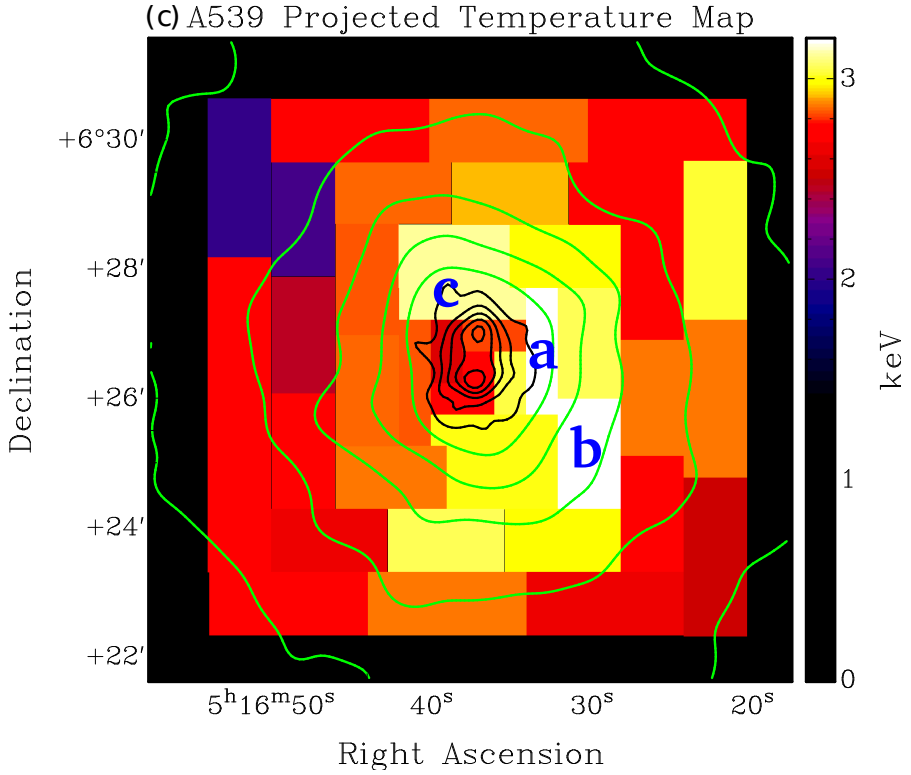
(c) A539 Projected Temperature Map
+6°30′
+28′
+26′
+24′
+22′
Declination
c
a
b
3
2
1
0
keV
5h16m50s
40s
30s
20s
Right Ascension

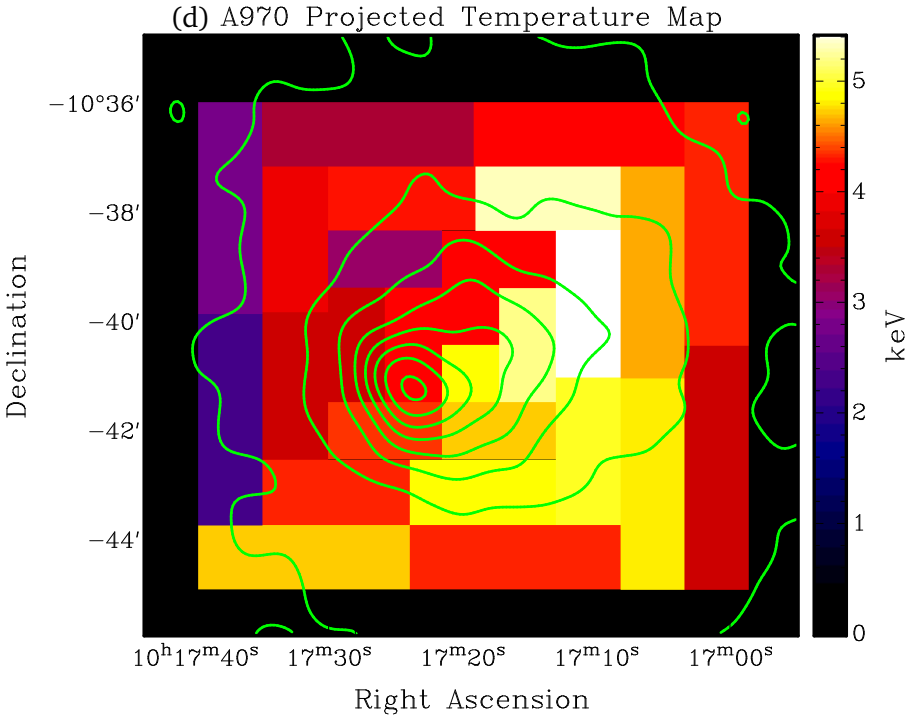
(d) A970 Projected Temperature Map
−10°36′
−38′
−40′
−42′
−44′
Declination
5
4
3
2
1
0
keV
10h17m40s
17m30s
17m20s
17m10s
17m00s
Right Ascension

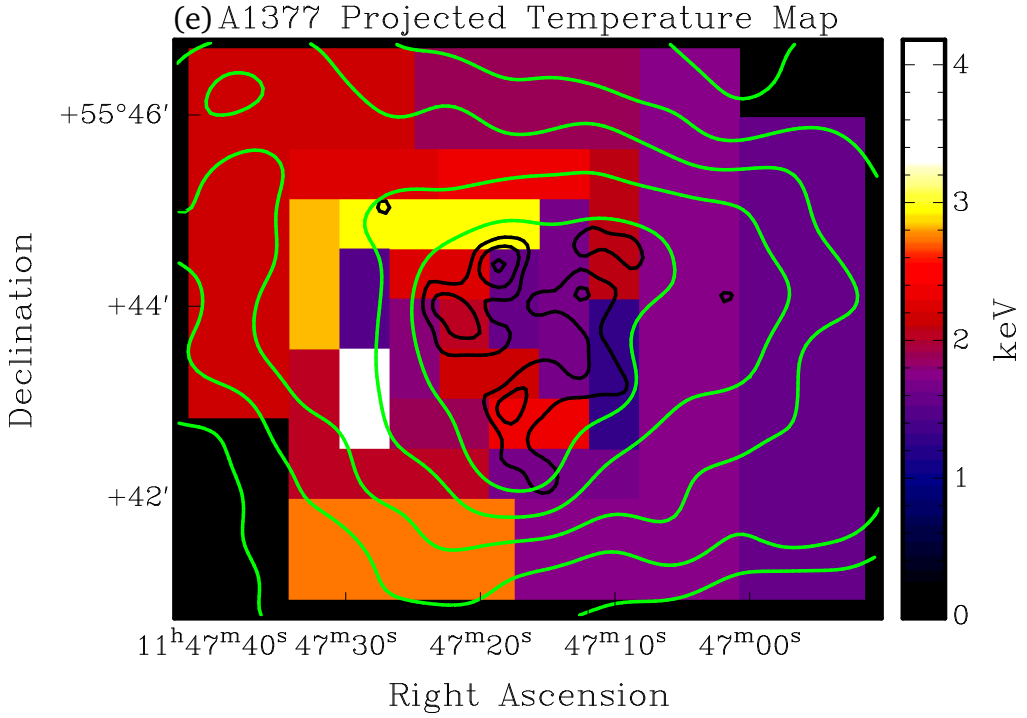
(e) A1377 Projected Temperature Map
+55°46′
+44′
+42′
Declination
11h47m40s 47m30s 47m20s 47m10s 47m00s
Right Ascension
4
3
2
1
0
keV

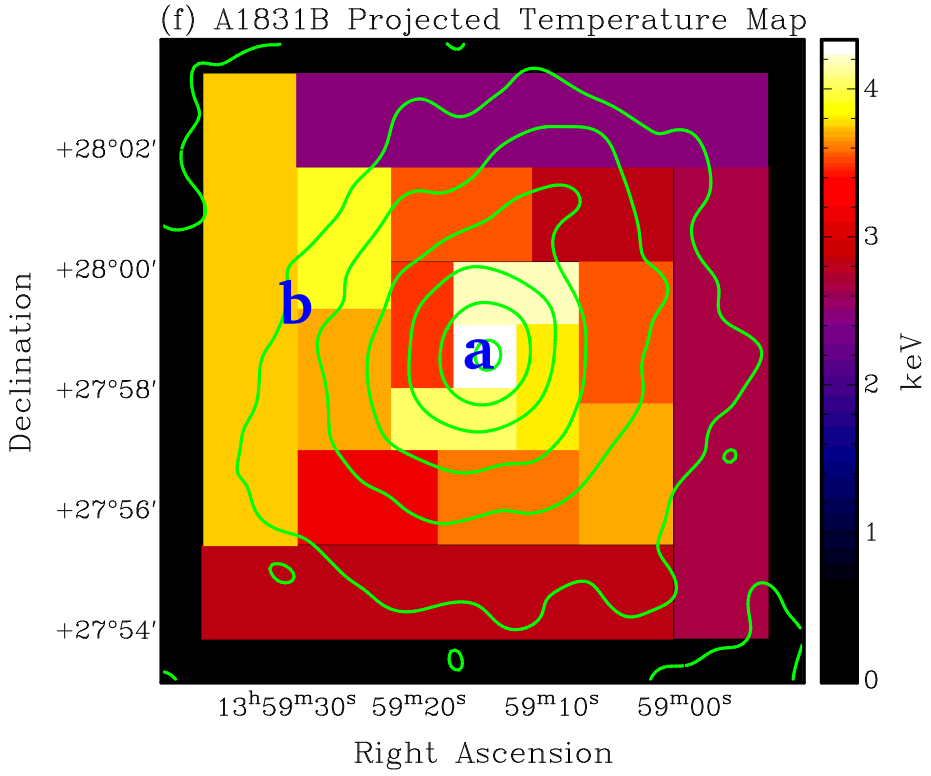
(f) A1831B Projected Temperature Map
+28°02′
+28°00′
+27°58′
+27°56′
+27°54′
Declination
b
a
13h59m30s 59m20s 59m10s 59m00s
Right Ascension
4
3
2
1
0
keV

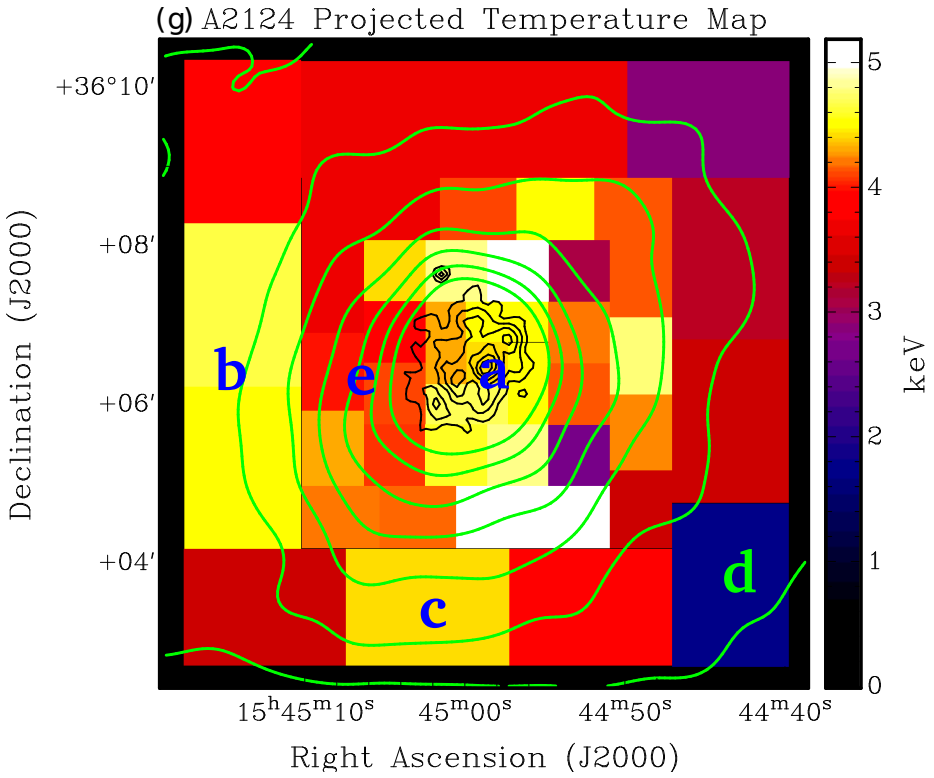
(g) A2124 Projected Temperature Map
+36°10′
+08′
+06′
+04′
Declination (J2000)
b
e
a
c
d
5
4
3
2
1
0
keV
15h45m10s
45m00s
44m50s
44m40s
Right Ascension (J2000)

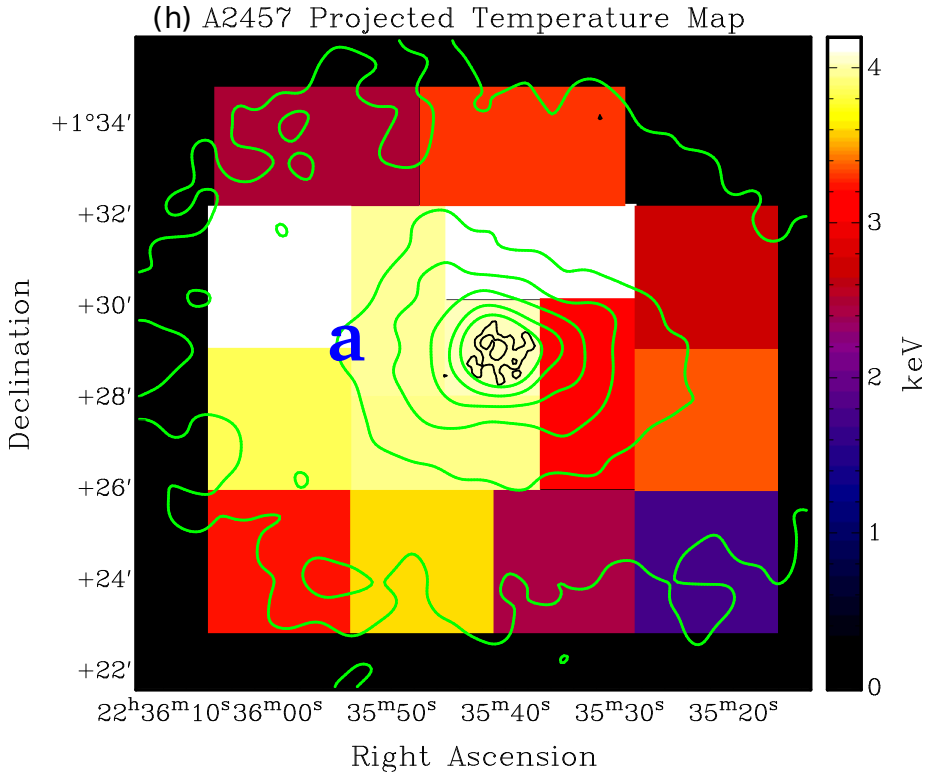
(h) A2457 Projected Temperature Map
+1°34′
+32′
+30′
+28′
+26′
+24′
+22′
Declination
a
4
3
2
1
0
keV
22h36m10s36m00s
35m50s
35m40s
35m30s
35m20s
Right Ascension

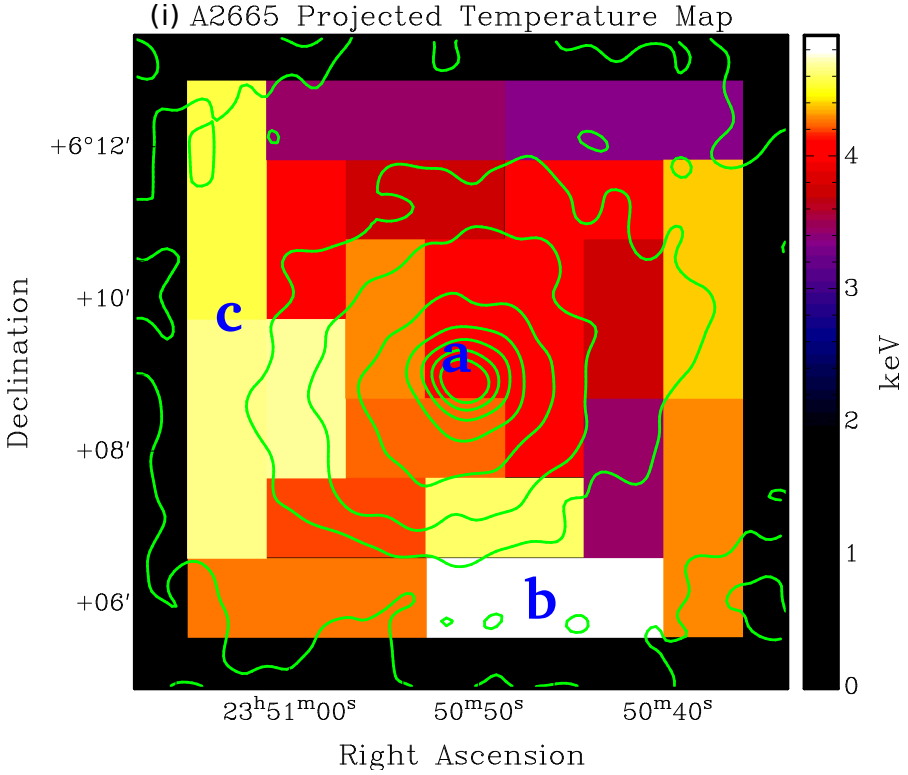
(i) A2665 Projected Temperature Map
+6°12′
+10′
+08′
+06′
Declination
c
a
b
keV
0
1
2
3
4
23h51m00s
50m50s
50m40s
Right Ascension

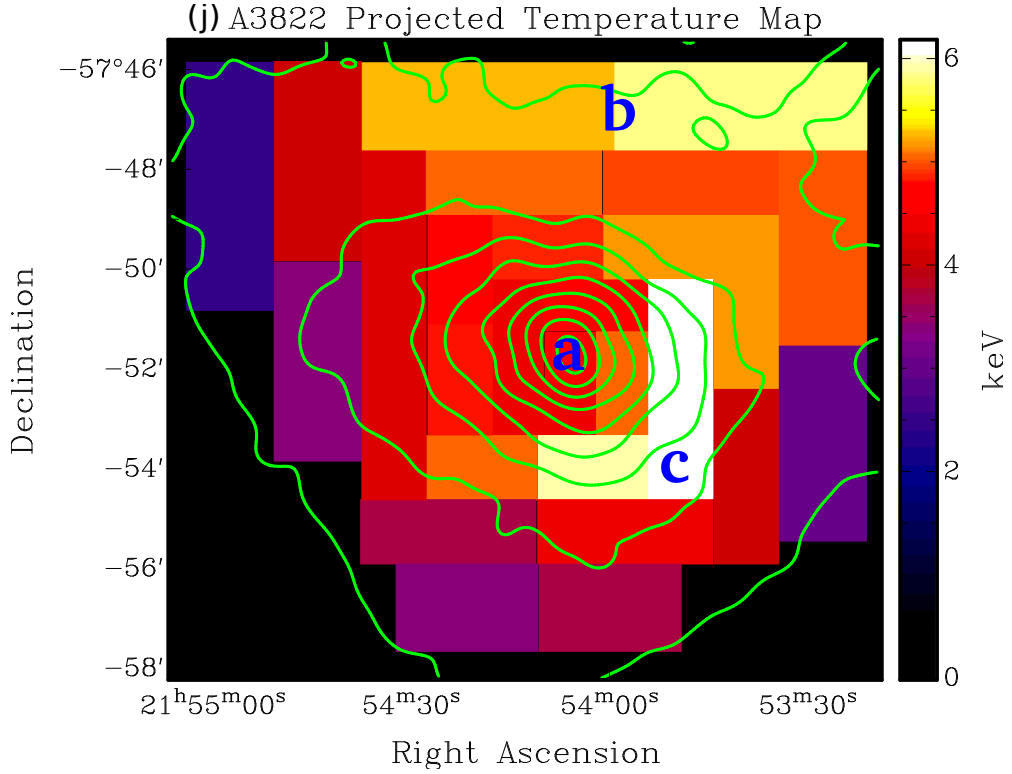
(j) A3822 Projected Temperature Map
−57°46′
−48′
−50′
−52′
−54′
−56′
−58′
Declination
b
a
c
keV
0
2
4
6
21h55m00s
54m30s
54m00s
53m30s
Right Ascension

Fig. 9.— (a)-(j): Projected temperature (kT) maps of the clusters A193, A376, A539, A970, A1377, A1831B, A2124, A2457, A2665, and A3822, respectively, obtained from the spectral analysis of box shaped regions (see §3.5). The overlaid green contours for A193 and A2665 are from their *Chandra* images smoothed with a Gaussian kernel of width $12''$ with intensity levels distributed from 14σ to 43σ and 3σ to 106σ above the mean background level, respectively. The overlaid green contours for A376, A539, A970, A1377, A1831, A2124, A2457 and A3822 are from their *Chandra* images smoothed with a Gaussian kernel of width $20''$ with intensity levels distributed from 5σ to 17σ, 15σ to 78σ, 2σ to 115σ, 6σ to 20σ, 2σ to 92σ, 2σ to 23σ, 1σ to 25σ and 3σ to 47σ above the mean background level, respectively. The overlaid black contours for A193, A376, A539, A1377, A2124 and A2457 are from their *Chandra* images smoothed with Gaussian kernels of width $4''$, $8''$, $8''$, $8''$, $4''$ and $4''$, with intensity levels distributed from 22σ to 25σ, 12σ to 30σ, 27σ to 89σ, 10σ to 13σ, 10σ to 17σ and 14σ to 32σ above the mean background level, respectively.

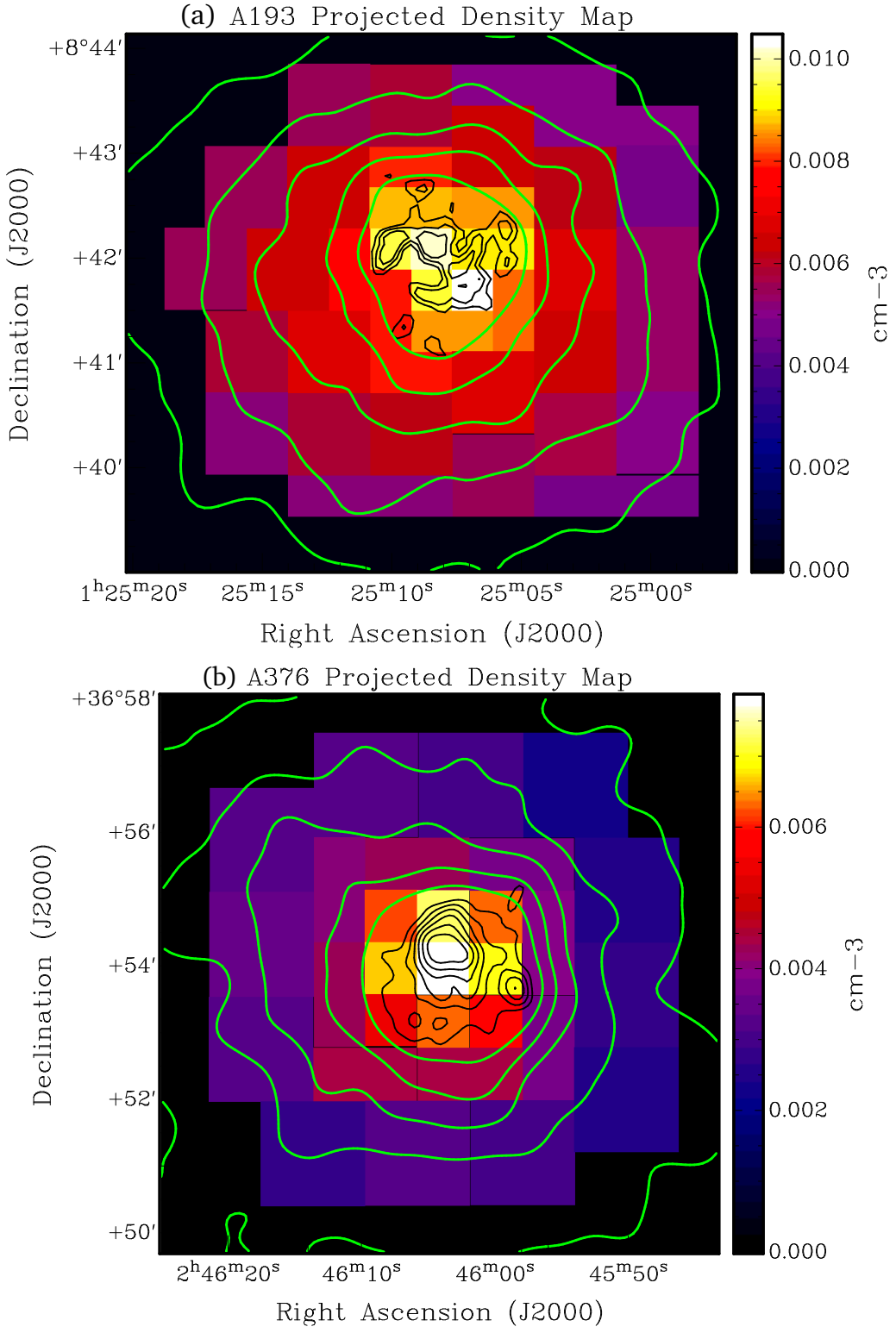
(a) A193 Projected Density Map
+8°44′
+43′
+42′
+41′
+40′
Declination (J2000)
1h25m20s
25m15s
25m10s
25m05s
25m00s
Right Ascension (J2000)
0.010
0.008
0.006
0.004
0.002
0.000
cm−3
(b) A376 Projected Density Map
+36°58′
+56′
+54′
+52′
+50′
Declination (J2000)
2h46m20s
46m10s
46m00s
45m50s
Right Ascension (J2000)
0.006
0.004
0.002
0.000
cm−3

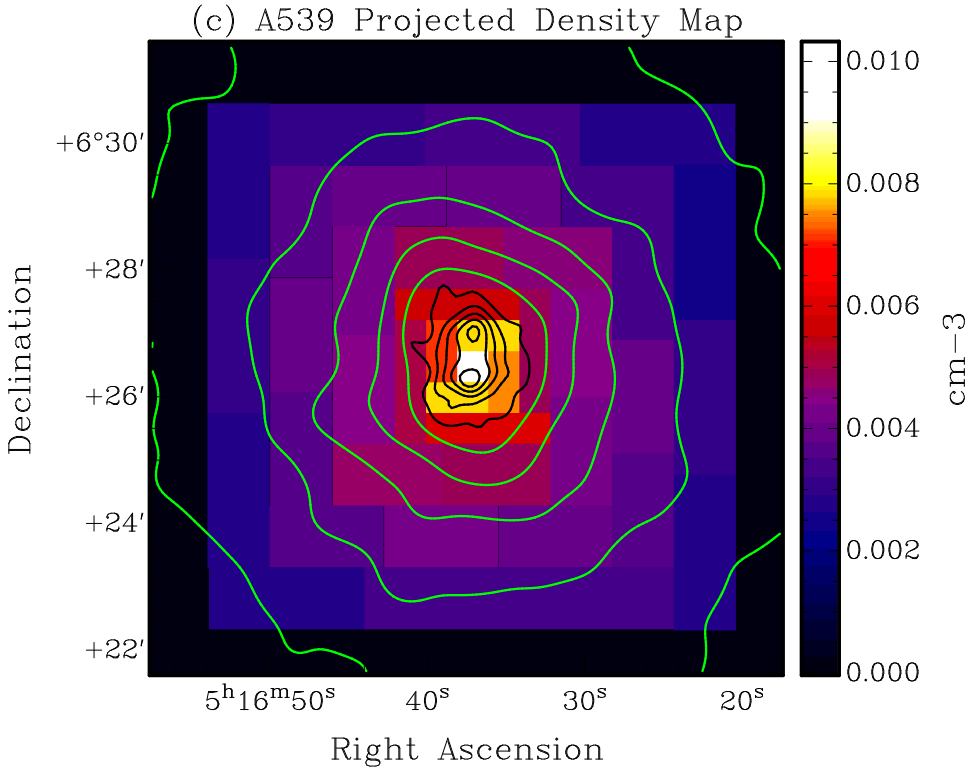
(c) A539 Projected Density Map
+6°30′
+28′
+26′
+24′
+22′
Declination
5h16m50s
40s
30s
20s
Right Ascension
0.010
0.008
0.006
0.004
0.002
0.000
cm−3

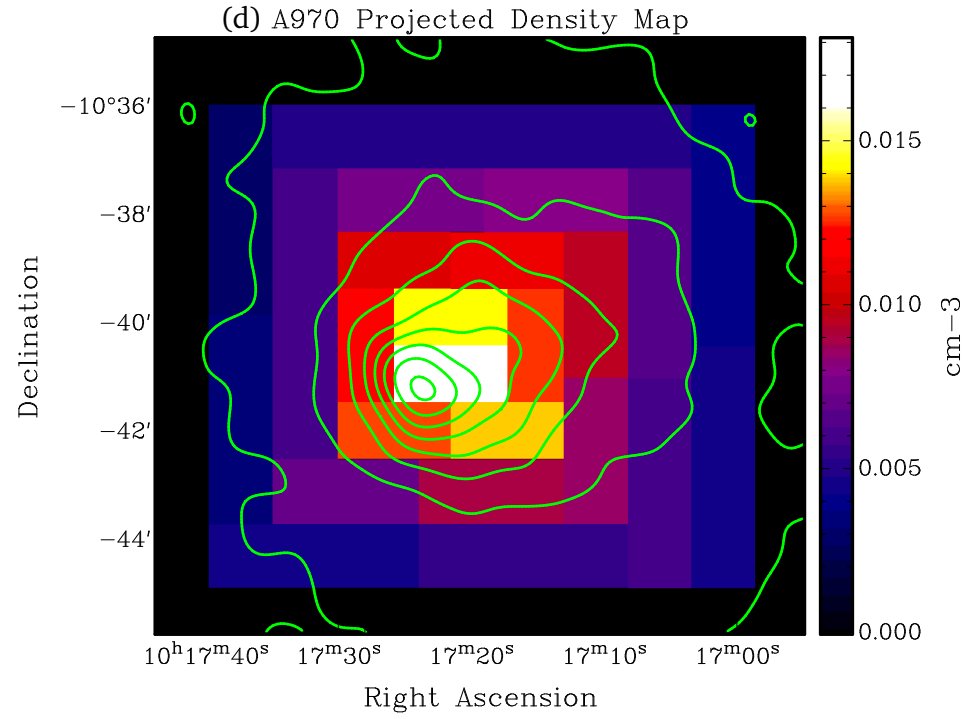
(d) A970 Projected Density Map
−10°36′
−38′
−40′
−42′
−44′
Declination
10h17m40s
17m30s
17m20s
17m10s
17m00s
Right Ascension
0.015
0.010
0.005
0.000
cm−3

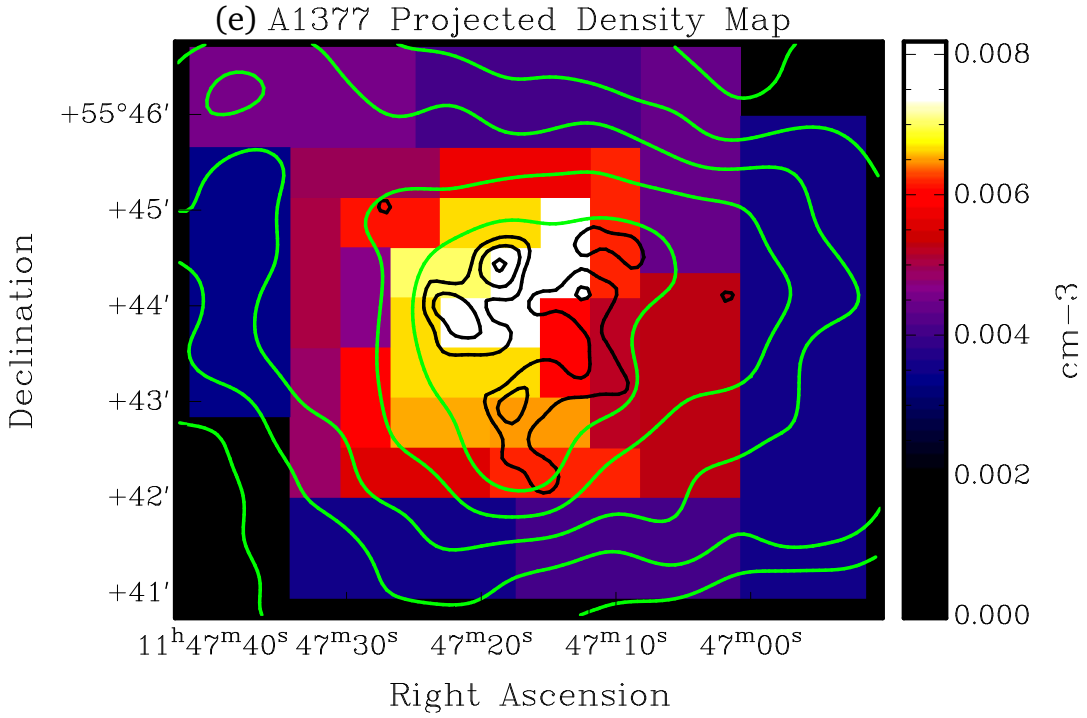
(e) A1377 Projected Density Map
+55°46′
+45′
+44′
+43′
+42′
+41′
Declination
11h47m40s
47m30s
47m20s
47m10s
47m00s
Right Ascension
0.008
0.006
0.004
0.002
0.000
cm−3

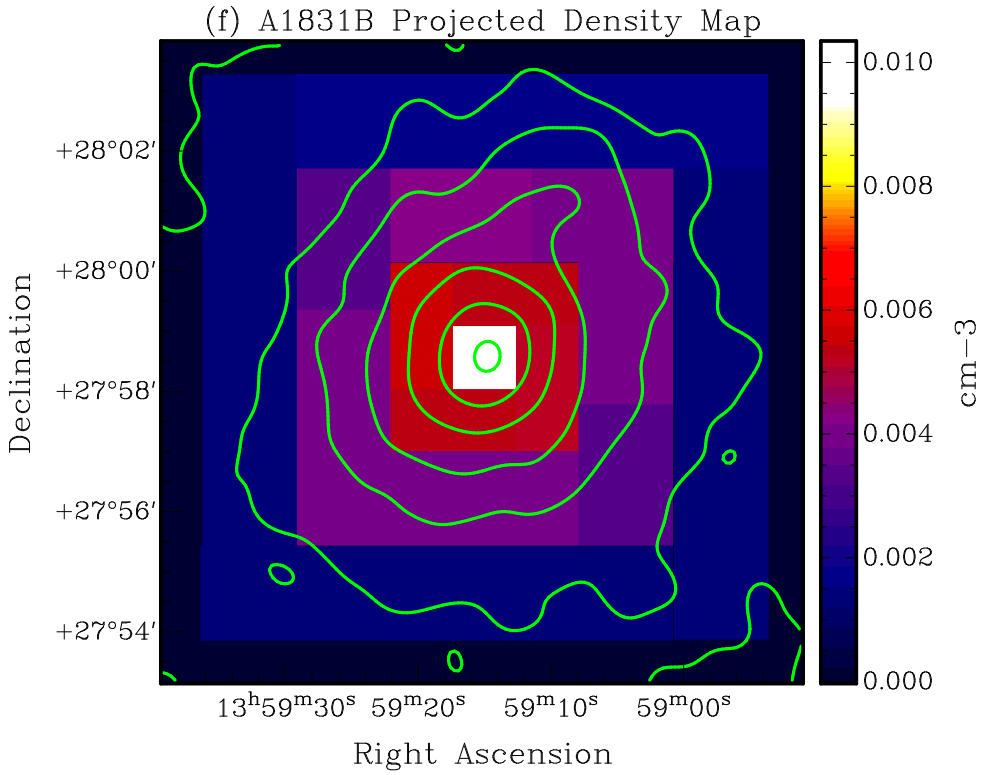
(f) A1831B Projected Density Map
+28°02′
+28°00′
+27°58′
+27°56′
+27°54′
Declination
13h59m30s
59m20s
59m10s
59m00s
Right Ascension
0.010
0.008
0.006
0.004
0.002
0.000
cm−3

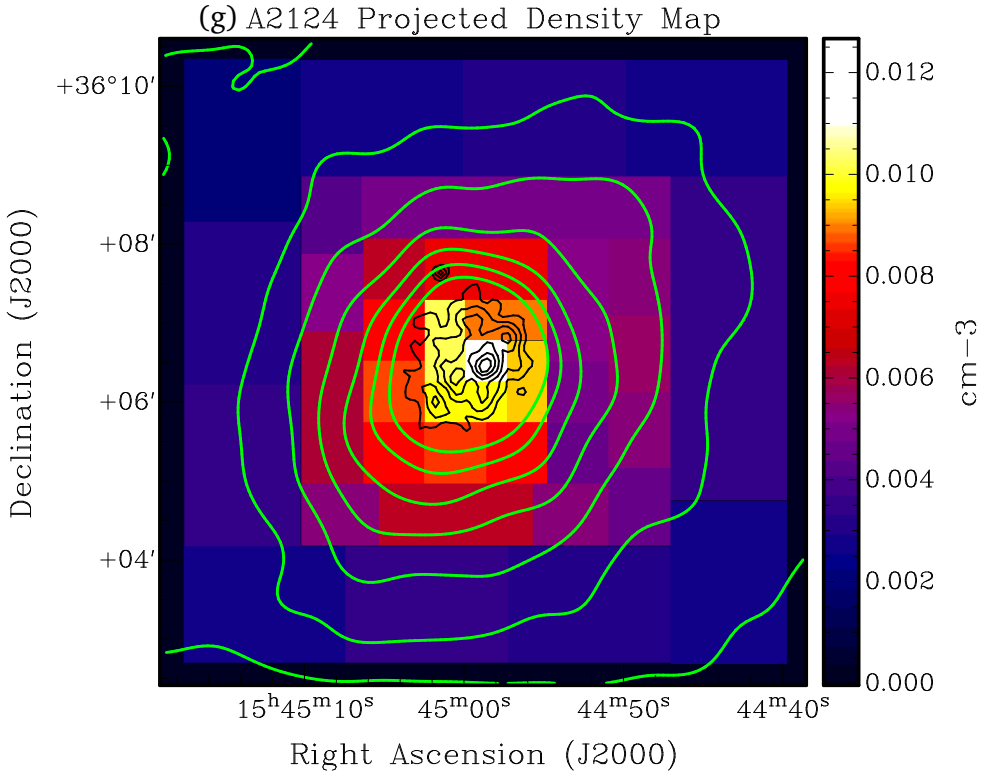
(g) A2124 Projected Density Map
+36°10′
+08′
+06′
+04′
Declination (J2000)
15h45m10s
45m00s
44m50s
44m40s
Right Ascension (J2000)
0.012
0.010
0.008
0.006
0.004
0.002
0.000
cm−3

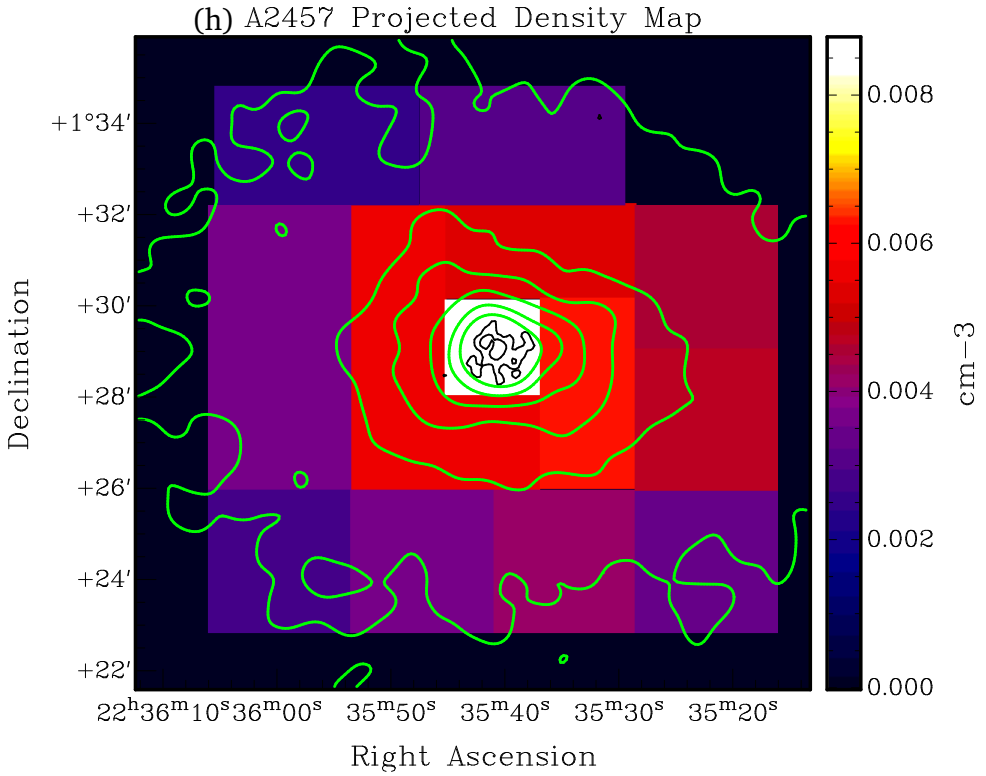
(h) A2457 Projected Density Map
+1°34′
+32′
+30′
+28′
+26′
+24′
+22′
Declination
22h36m10s36m00s
35m50s
35m40s
35m30s
35m20s
Right Ascension
0.008
0.006
0.004
0.002
0.000
cm−3

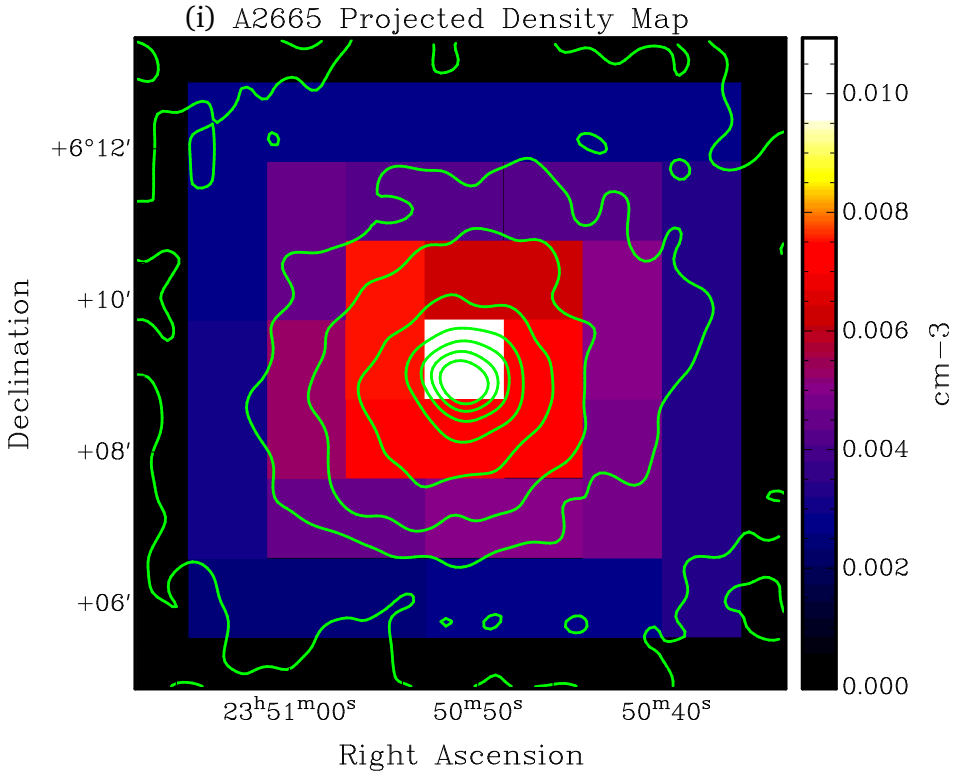
(i) A2665 Projected Density Map
+6°12′
+10′
+08′
+06′
Declination
23h51m00s
50m50s
50m40s
Right Ascension
0.010
0.008
0.006
0.004
0.002
0.000
cm−3

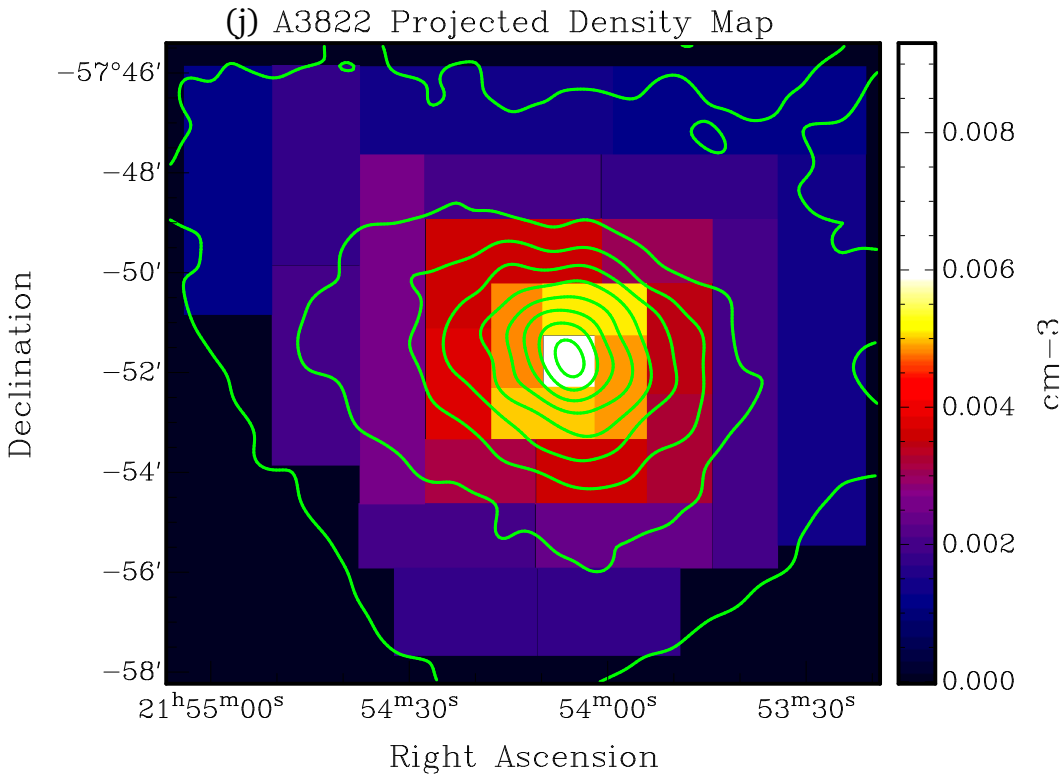
(j) A3822 Projected Density Map
−57°46′
−48′
−50′
−52′
−54′
−56′
−58′
Declination
21h55m00s
54m30s
54m00s
53m30s
Right Ascension
0.008
0.006
0.004
0.002
0.000
cm−3

Fig. 10.— (a)-(j): Projected electron number density (n_e) maps of the clusters A193, A376, A539, A970, A1377, A1831B, A2124, A2457, A2665 and A3822, respectively, obtained from the spectral analyses of box shaped regions (see §3.5). The overlaid intensity contours are from the *Chandra* images as explained in the caption of Figure 9.

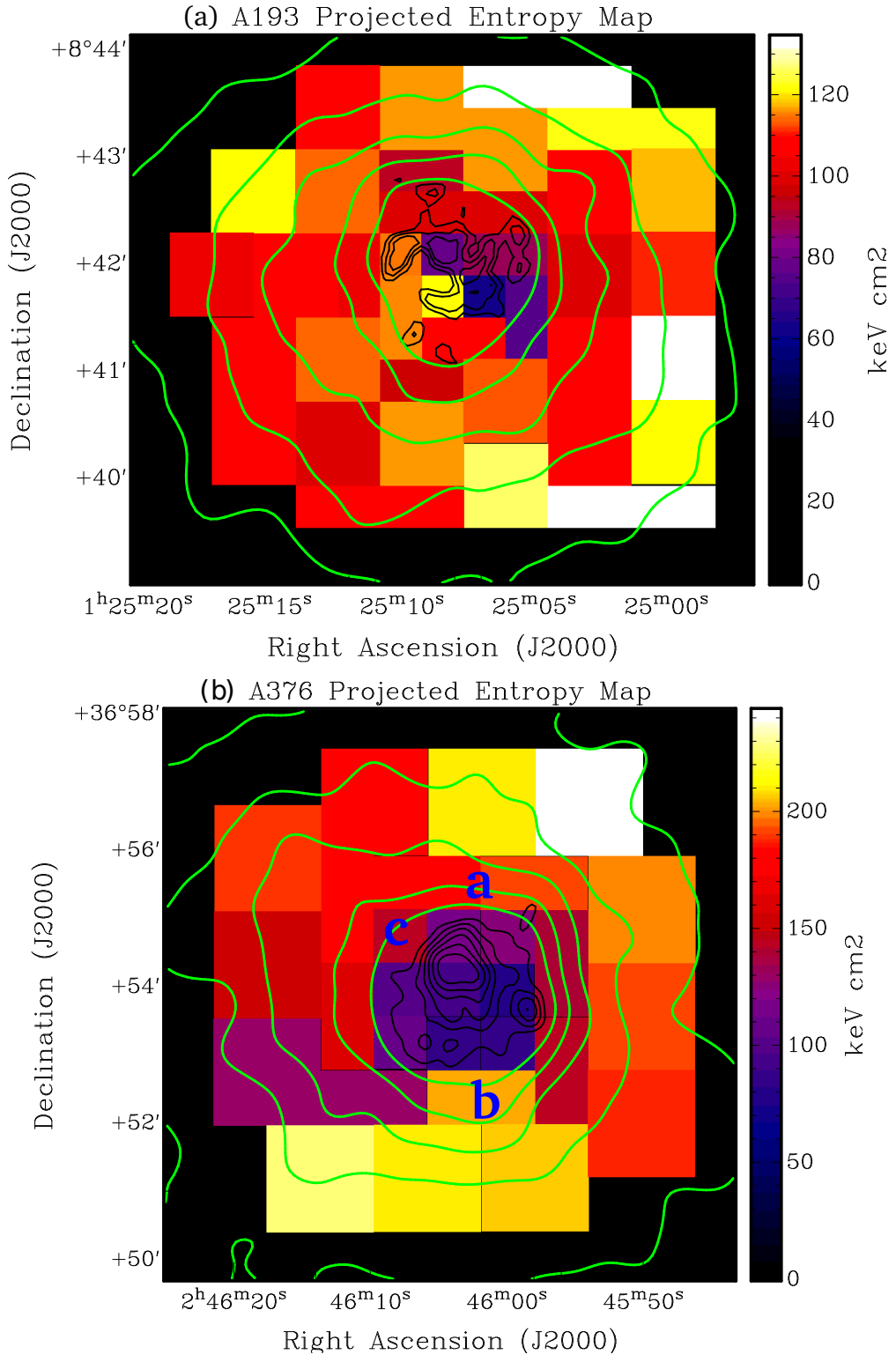
(a) A193 Projected Entropy Map
+8°44′
+43′
+42′
+41′
+40′
Declination (J2000)
1h25m20s
25m15s
25m10s
25m05s
25m00s
Right Ascension (J2000)
120
100
80
60
40
20
0
keV cm2
(b) A376 Projected Entropy Map
+36°58′
+56′
+54′
+52′
+50′
Declination (J2000)
a
c
b
2h46m20s
46m10s
46m00s
45m50s
Right Ascension (J2000)
200
150
100
50
0
keV cm2

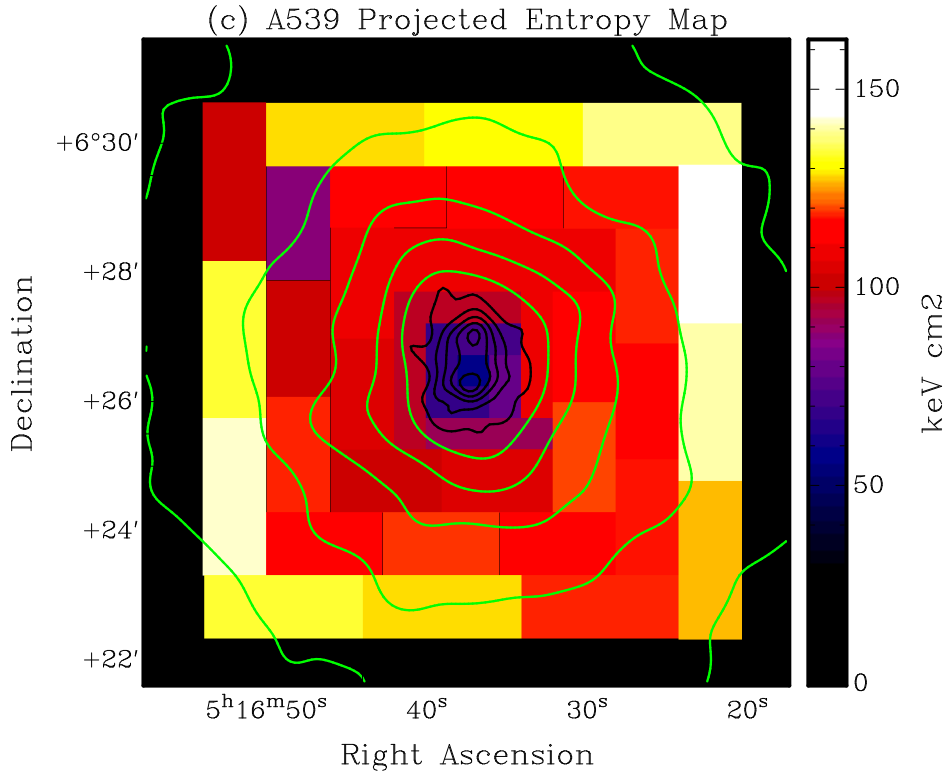
(c) A539 Projected Entropy Map
+6°30′
+28′
+26′
+24′
+22′
Declination
5h16m50s
40s
30s
20s
Right Ascension
150
100
50
0
keV cm2

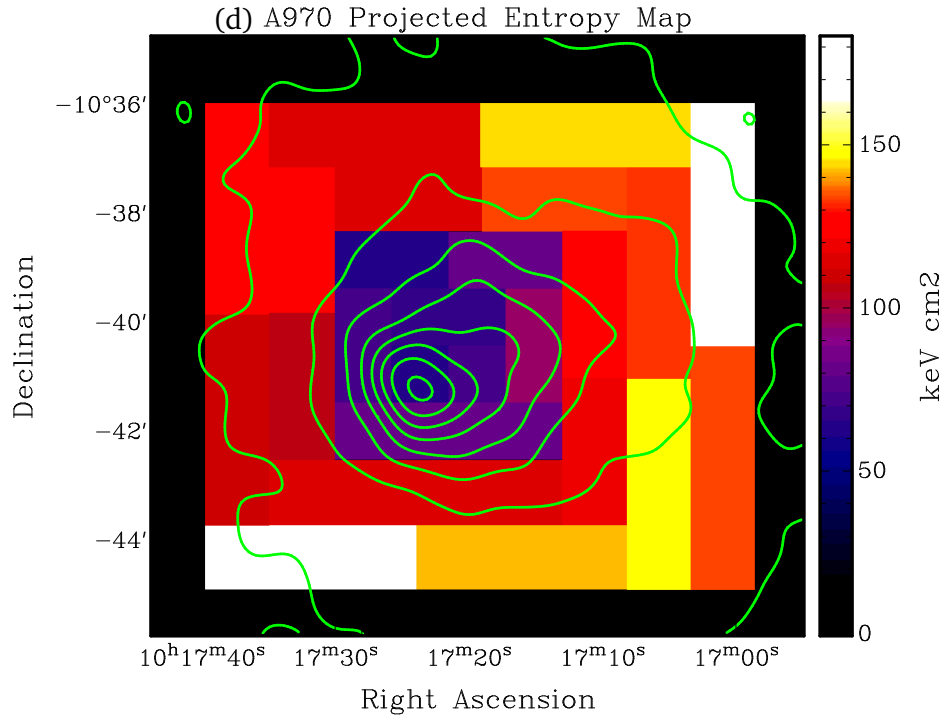
(d) A970 Projected Entropy Map
−10°36′
−38′
−40′
−42′
−44′
Declination
10h17m40s
17m30s
17m20s
17m10s
17m00s
Right Ascension
150
100
50
0
keV cm2

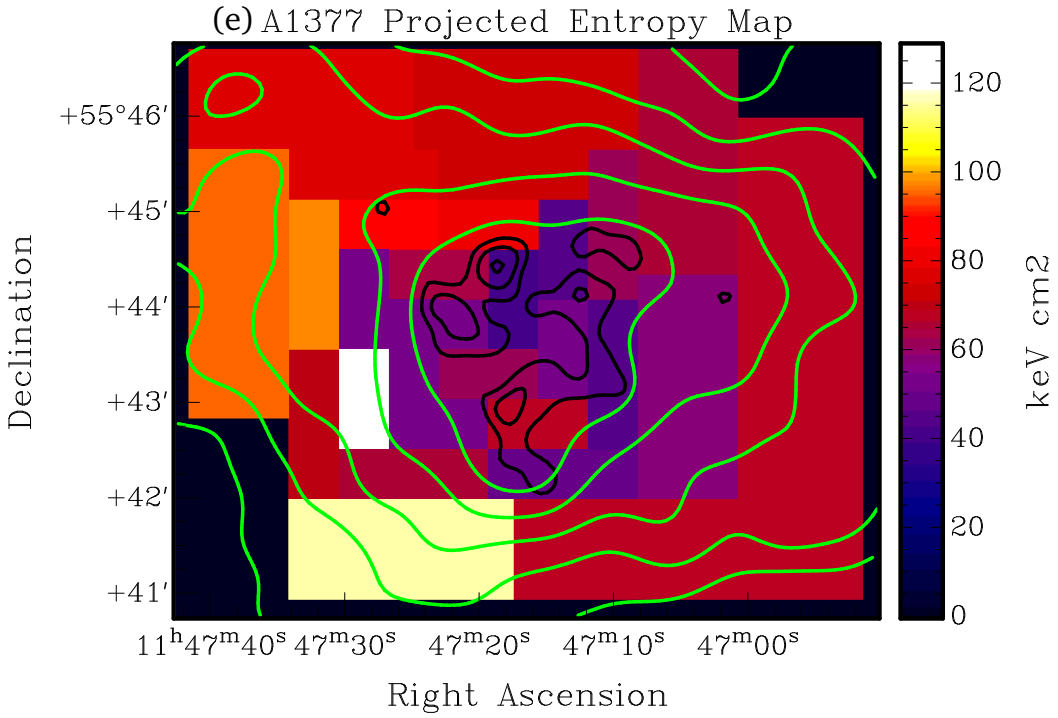
(e) A1377 Projected Entropy Map
+55°46′
+45′
+44′
+43′
+42′
+41′
Declination
11h47m40s 47m30s 47m20s 47m10s 47m00s
Right Ascension
120
100
80
60
40
20
0
keV cm2

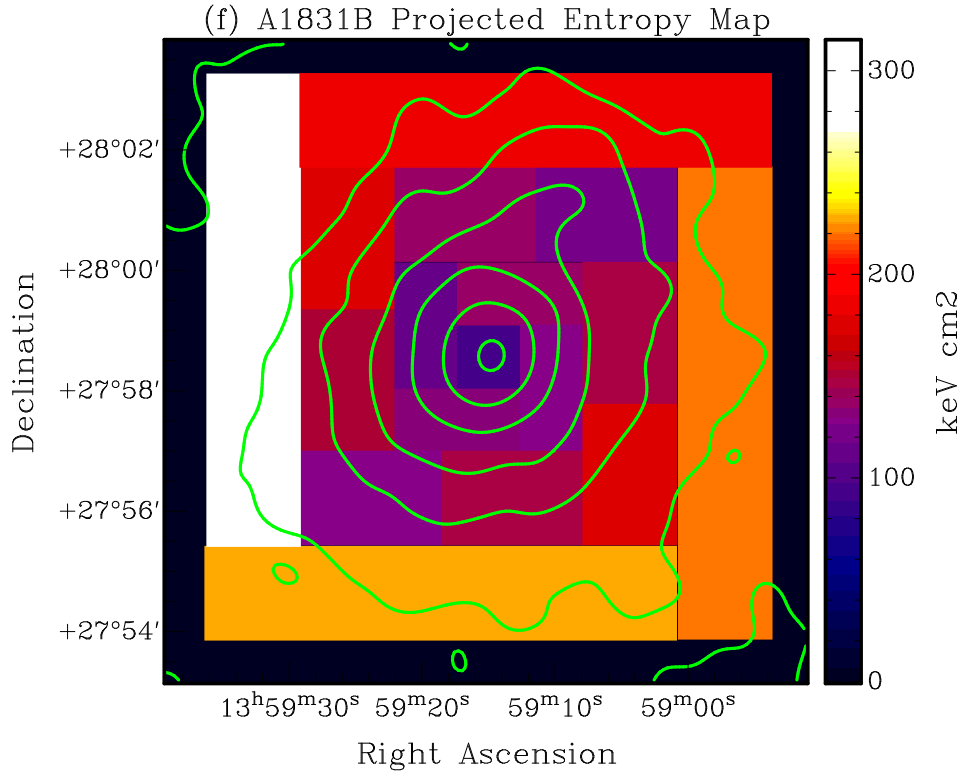
(f) A1831B Projected Entropy Map
+28°02′
+28°00′
+27°58′
+27°56′
+27°54′
Declination
13h59m30s 59m20s 59m10s 59m00s
Right Ascension
300
200
100
0
keV cm2

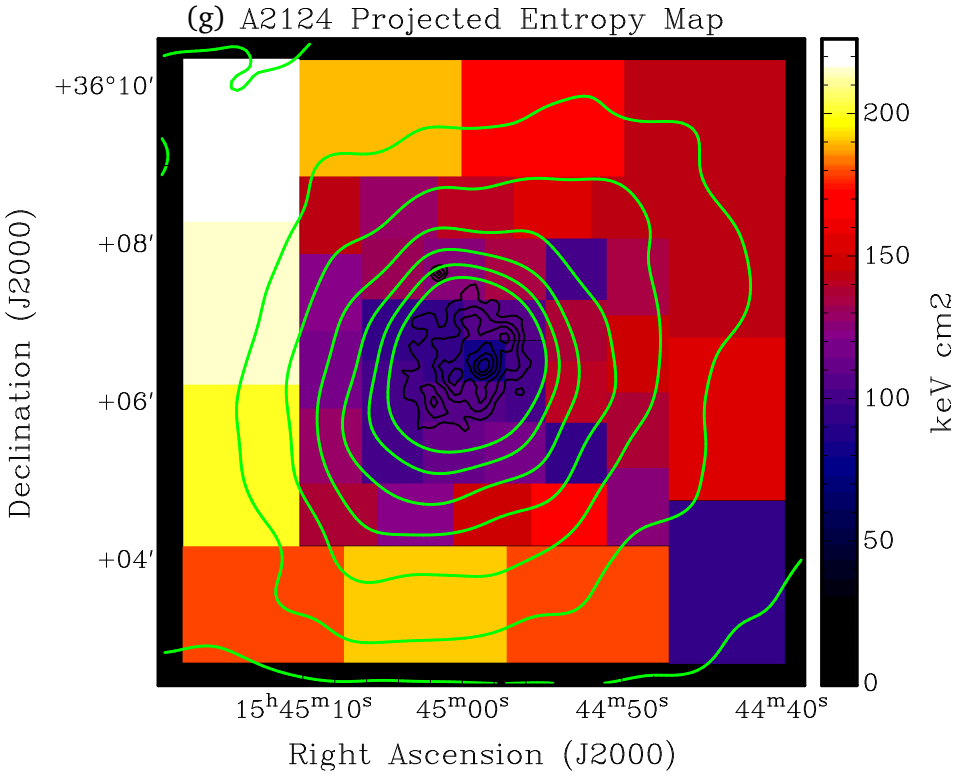
(g) A2124 Projected Entropy Map
+36°10′
+08′
+06′
+04′
Declination (J2000)
15h45m10s
45m00s
44m50s
44m40s
Right Ascension (J2000)
200
150
100
50
0
keV cm2

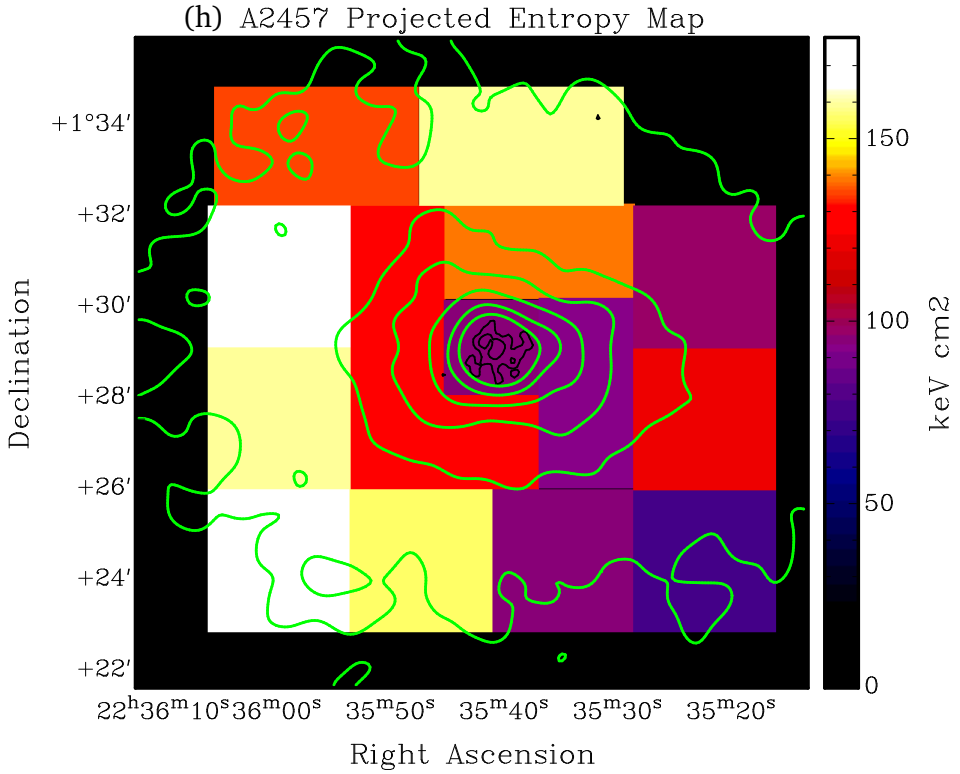
(h) A2457 Projected Entropy Map
+1°34′
+32′
+30′
+28′
+26′
+24′
+22′
Declination
22h36m10s36m00s
35m50s
35m40s
35m30s
35m20s
Right Ascension
150
100
50
0
keV cm2

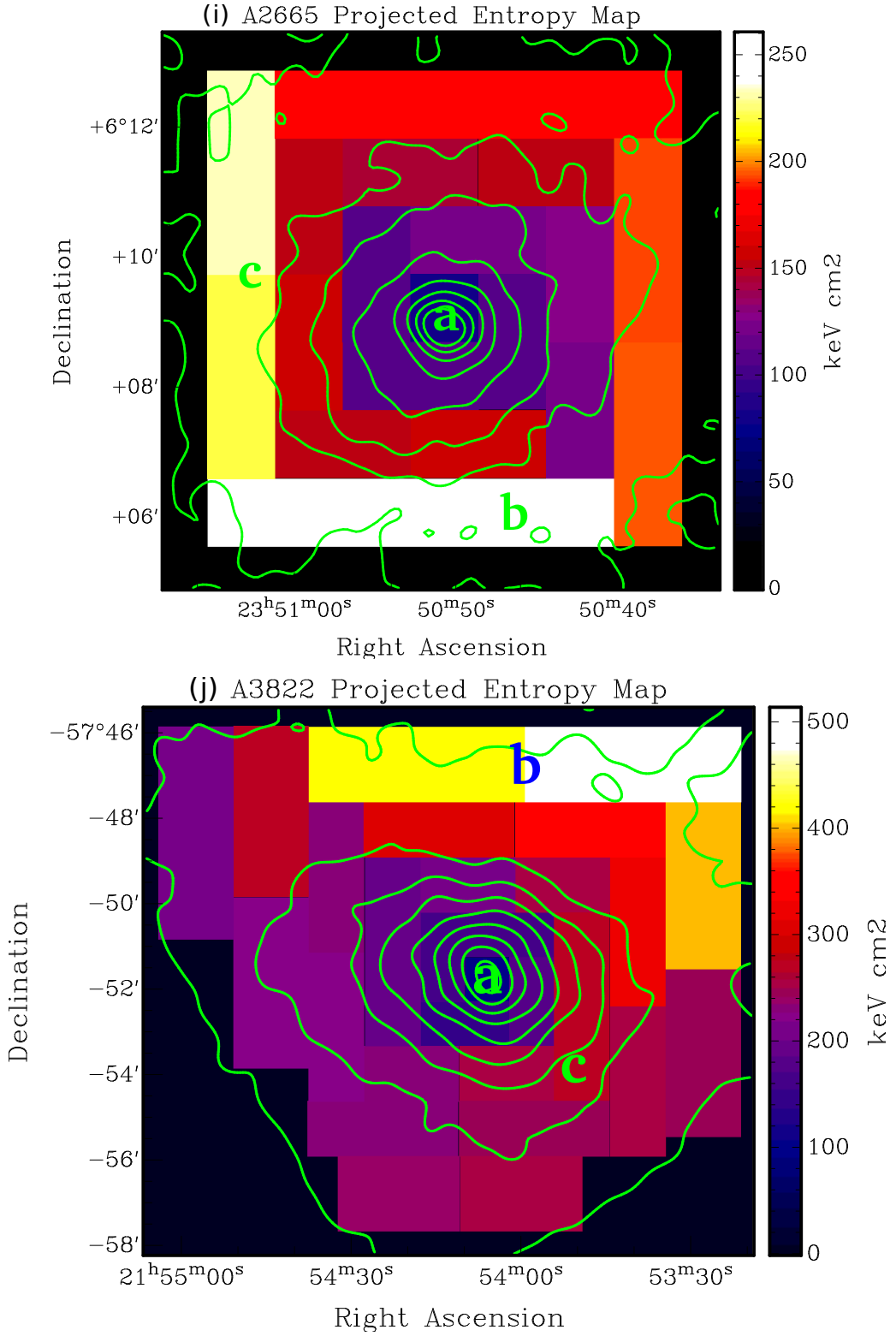
(i) A2665 Projected Entropy Map
+6°12′
+10′
+08′
+06′
Declination
23h51m00s
50m50s
50m40s
Right Ascension
a
b
c
250
200
150
100
50
0
keV cm2
(j) A3822 Projected Entropy Map
−57°46′
−48′
−50′
−52′
−54′
−56′
−58′
Declination
21h55m00s
54m30s
54m00s
53m30s
Right Ascension
a
b
c
500
400
300
200
100
0
keV cm2

Fig. 11.— (a)-(j): Projected entropy (S) maps of the clusters A193, A376, A539, A970, A1377, A1831B, A2124, A2457, A2665, and A3822, respectively, obtained from the spectral analyses of box shaped regions (details of spectral analyses are given in §3.5). The overlaid intensity contours are from the *Chandra* images as explained in the caption of Figure 9.

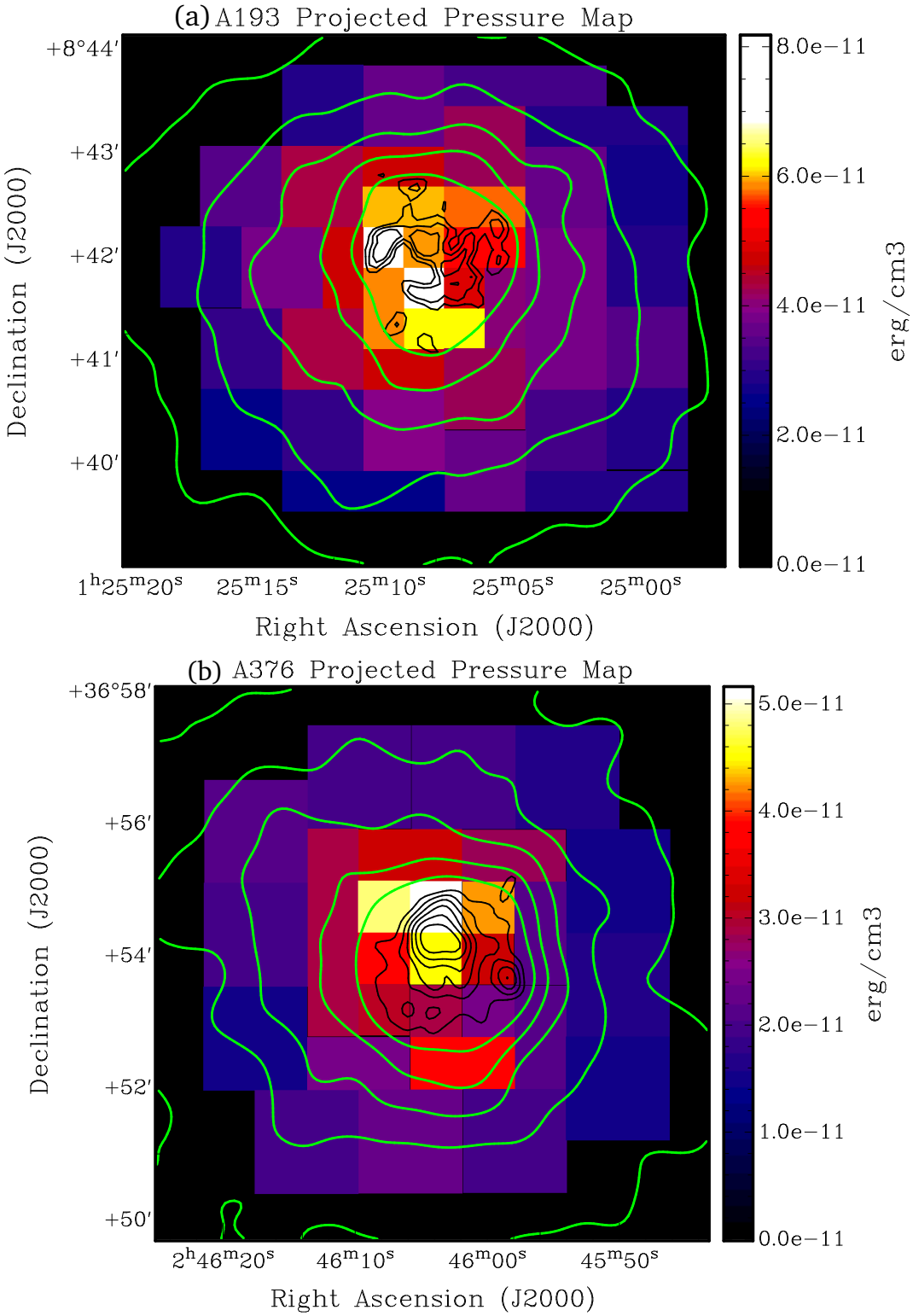
(a) A193 Projected Pressure Map
+8°44′
+43′
+42′
+41′
+40′
Declination (J2000)
1h25m20s
25m15s
25m10s
25m05s
25m00s
Right Ascension (J2000)
8.0e−11
6.0e−11
4.0e−11
2.0e−11
0.0e−11
erg/cm3
(b) A376 Projected Pressure Map
+36°58′
+56′
+54′
+52′
+50′
Declination (J2000)
2h46m20s
46m10s
46m00s
45m50s
Right Ascension (J2000)
5.0e−11
4.0e−11
3.0e−11
2.0e−11
1.0e−11
0.0e−11
erg/cm3

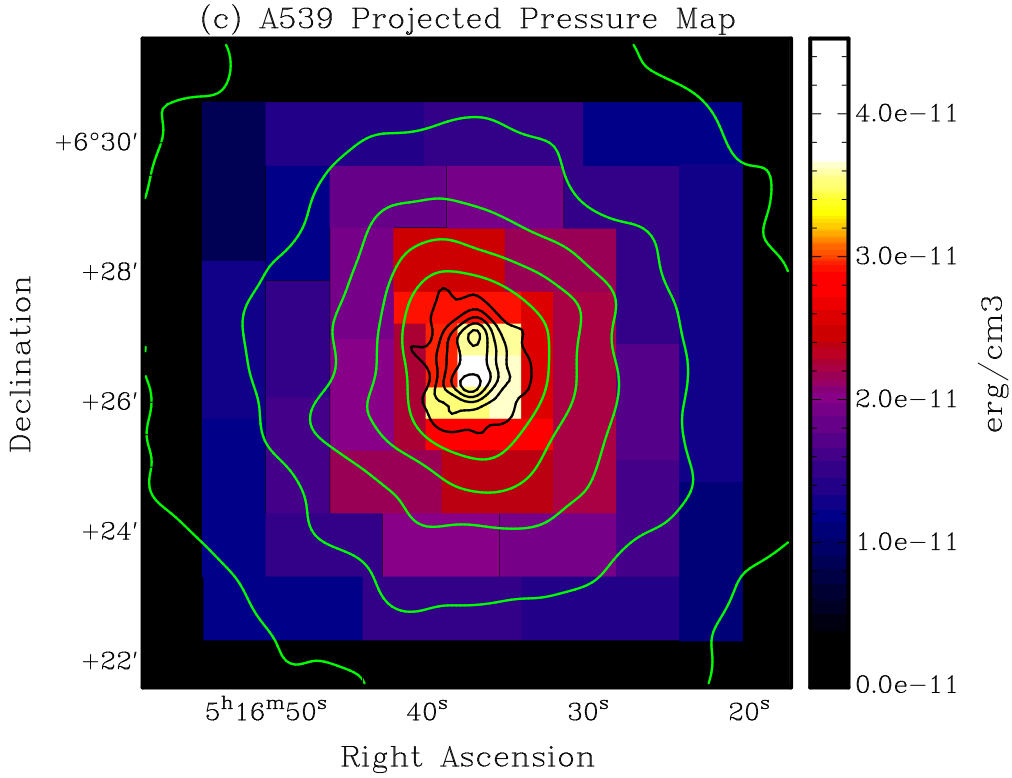
(c) A539 Projected Pressure Map
+6°30′
+28′
+26′
+24′
+22′
Declination
5h16m50s
40s
30s
20s
Right Ascension
4.0e−11
3.0e−11
2.0e−11
1.0e−11
0.0e−11
erg/cm3

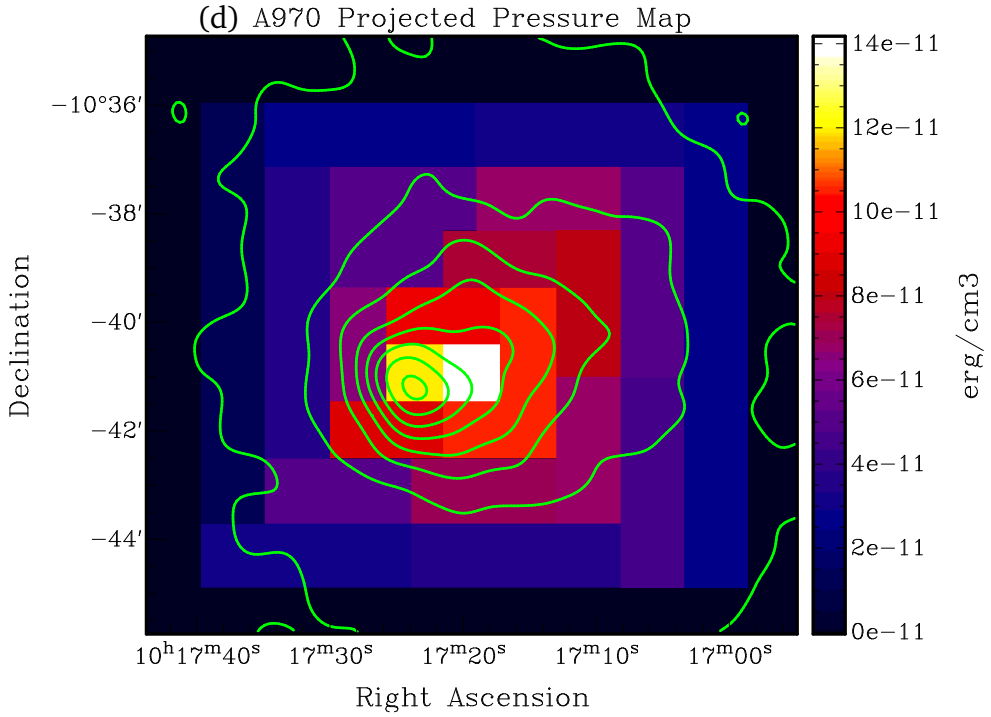
(d) A970 Projected Pressure Map
−10°36′
−38′
−40′
−42′
−44′
Declination
10h17m40s
17m30s
17m20s
17m10s
17m00s
Right Ascension
14e−11
12e−11
10e−11
8e−11
6e−11
4e−11
2e−11
0e−11
erg/cm3

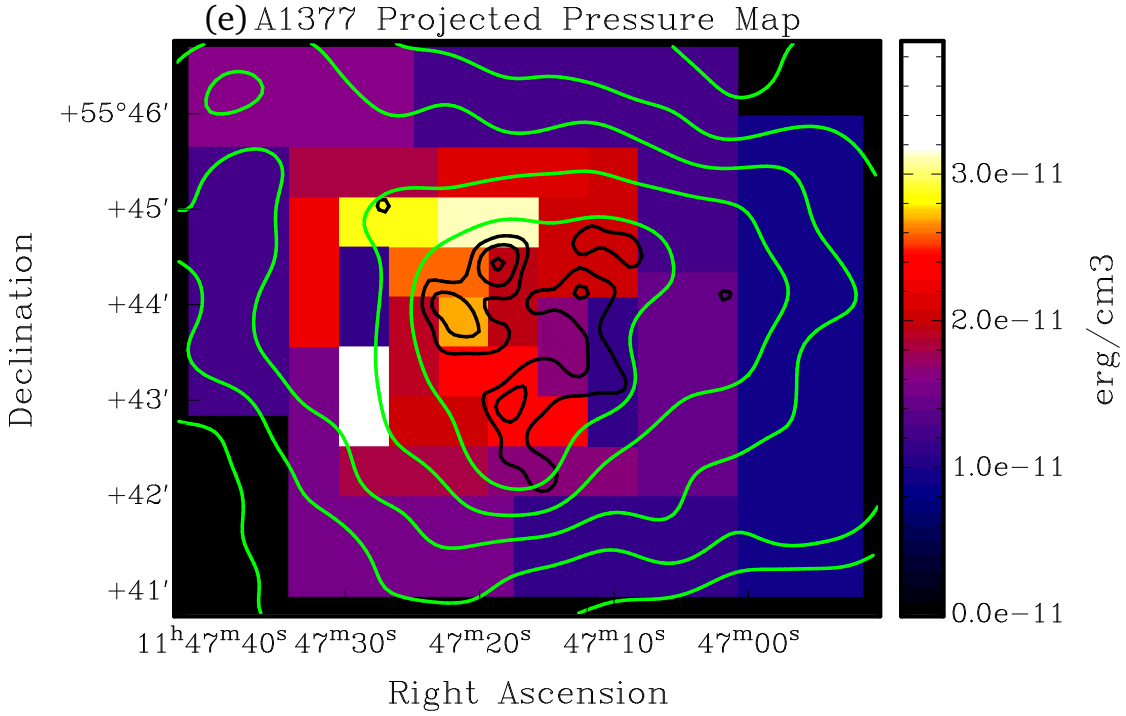
(e) A1377 Projected Pressure Map
+55°46′
+45′
+44′
+43′
+42′
+41′
Declination
11h47m40s
47m30s
47m20s
47m10s
47m00s
Right Ascension
3.0e−11
2.0e−11
1.0e−11
0.0e−11
erg/cm3

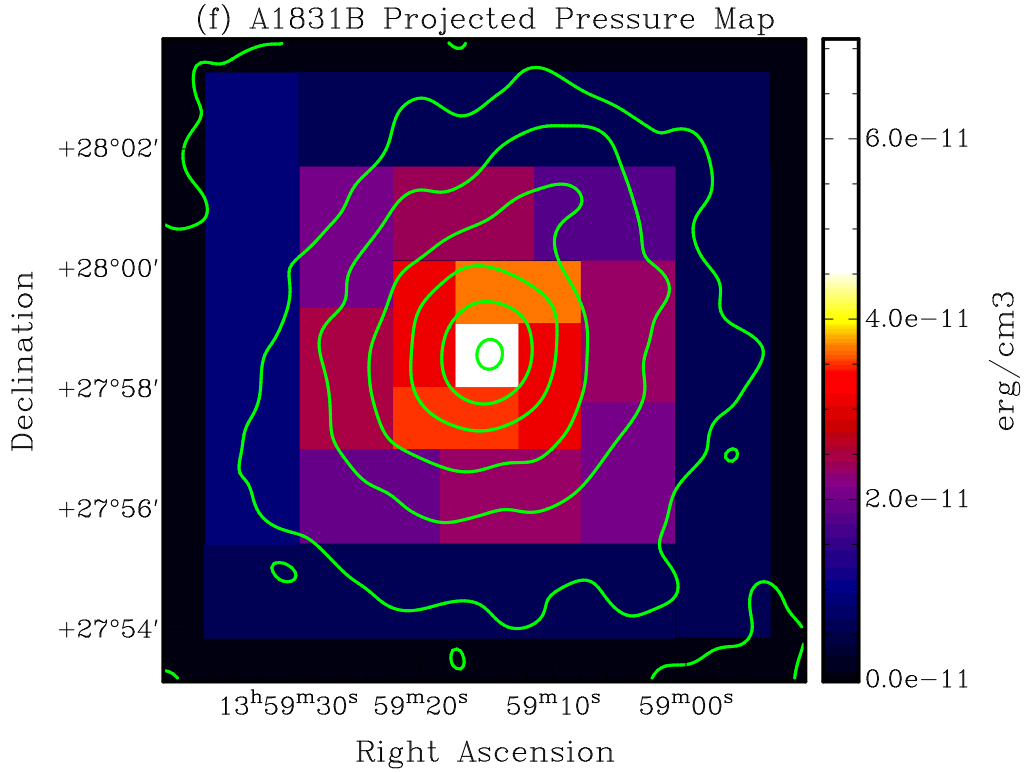
(f) A1831B Projected Pressure Map
+28°02′
+28°00′
+27°58′
+27°56′
+27°54′
Declination
13h59m30s
59m20s
59m10s
59m00s
Right Ascension
6.0e−11
4.0e−11
2.0e−11
0.0e−11
erg/cm3

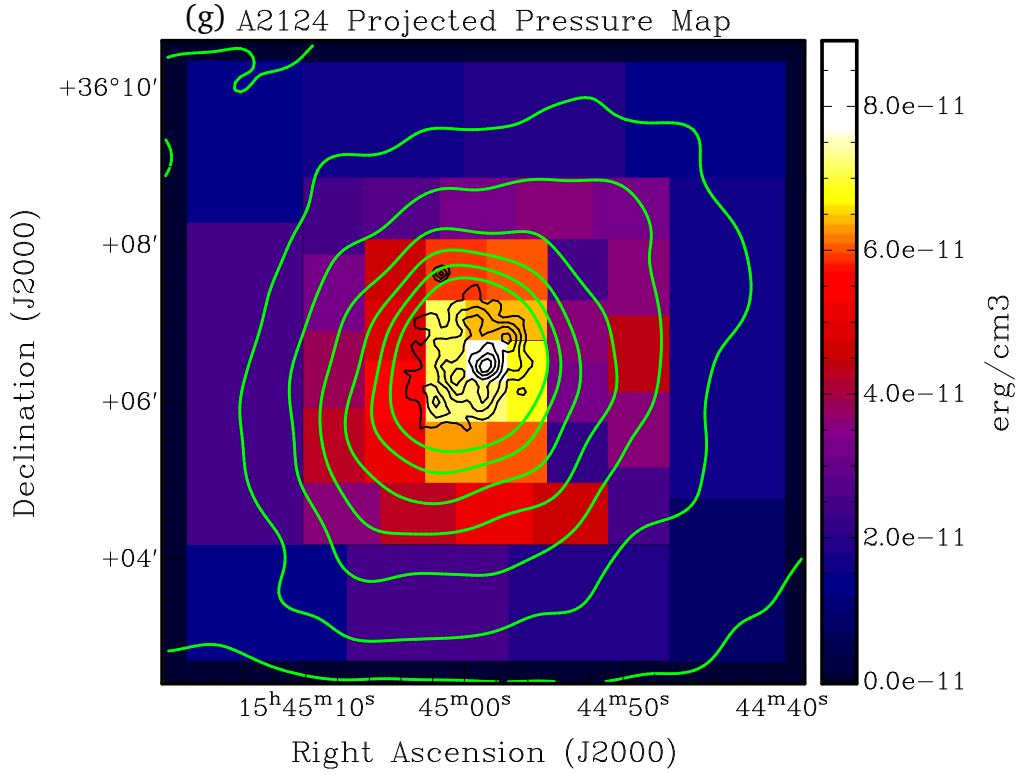
(g) A2124 Projected Pressure Map
+36°10′
+08′
+06′
+04′
Declination (J2000)
15h45m10s
45m00s
44m50s
44m40s
Right Ascension (J2000)
8.0e−11
6.0e−11
4.0e−11
2.0e−11
0.0e−11
erg/cm3

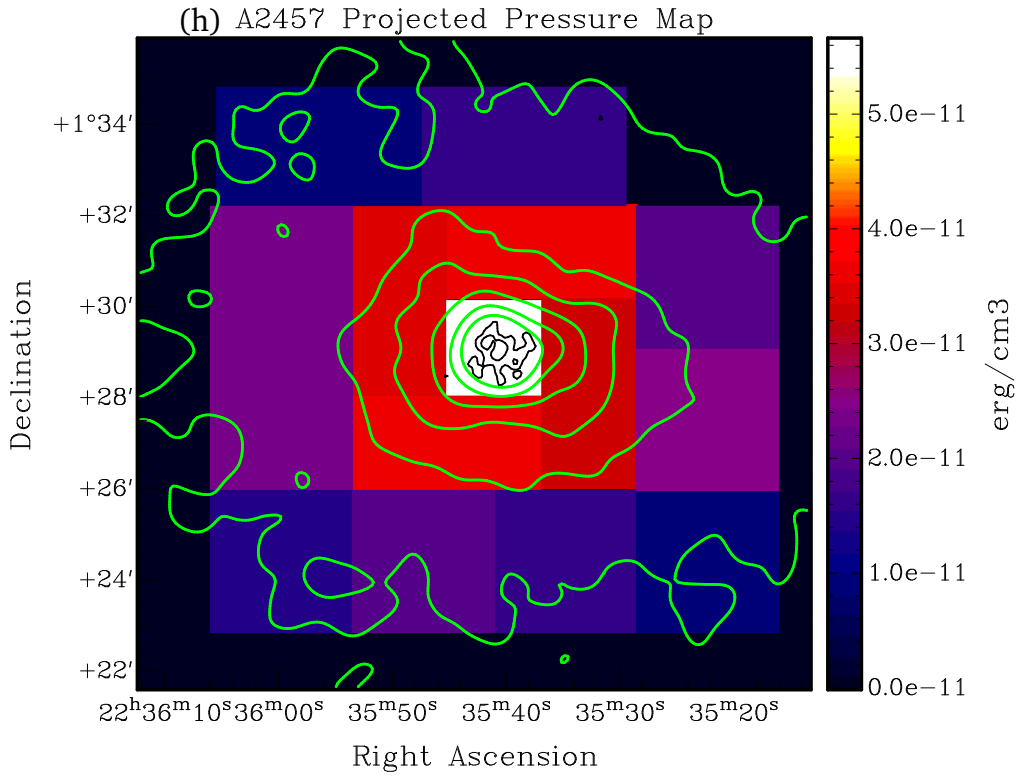
(h) A2457 Projected Pressure Map
+1°34′
+32′
+30′
+28′
+26′
+24′
+22′
Declination
22h36m10s36m00s
35m50s
35m40s
35m30s
35m20s
Right Ascension
5.0e−11
4.0e−11
3.0e−11
2.0e−11
1.0e−11
0.0e−11
erg/cm3

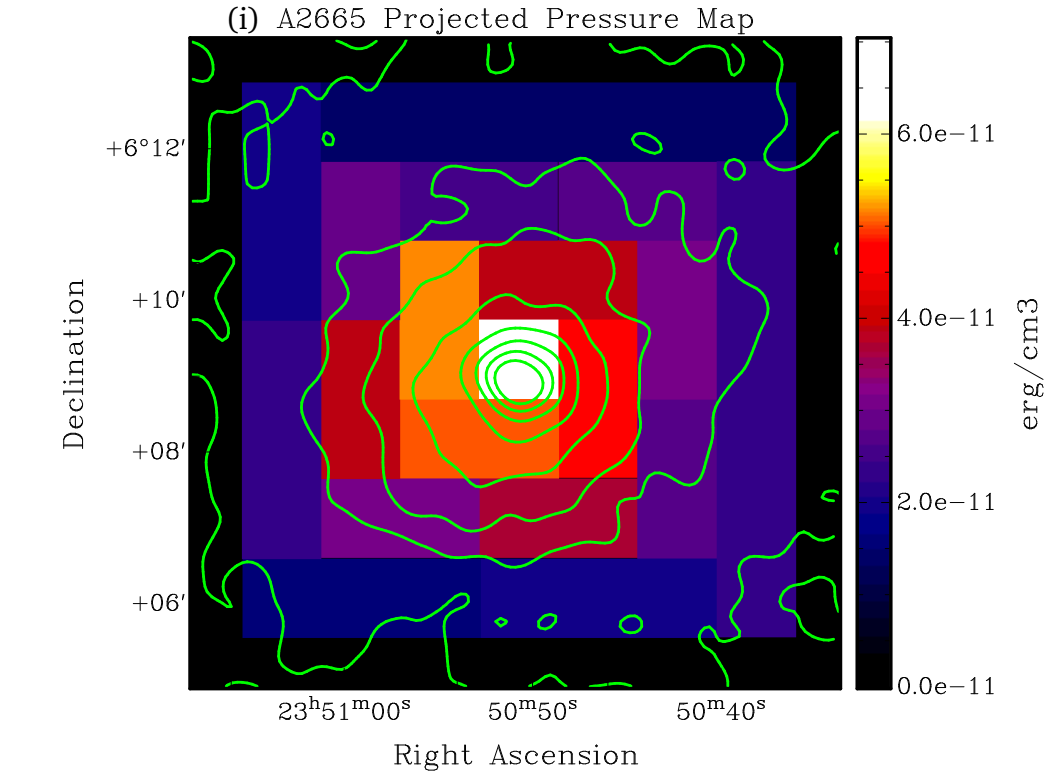
(i) A2665 Projected Pressure Map
+6°12′
+10′
+08′
+06′
Declination
23h51m00s
50m50s
50m40s
Right Ascension
6.0e−11
4.0e−11
2.0e−11
0.0e−11
erg/cm3

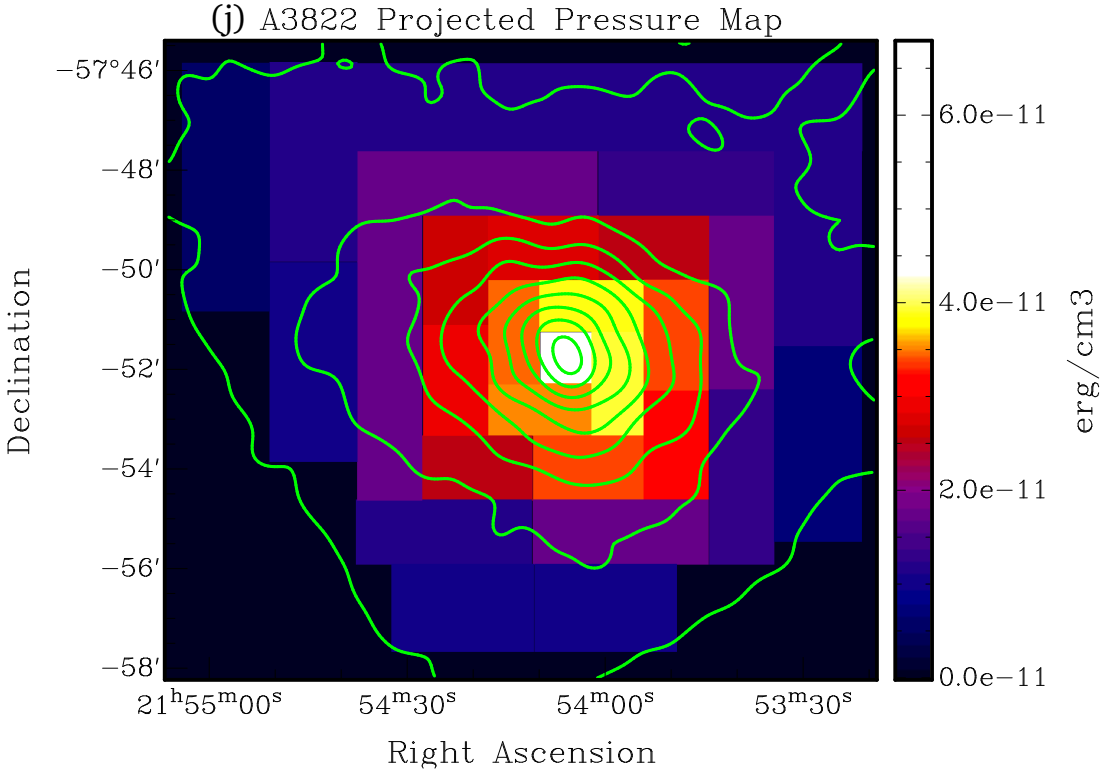
(j) A3822 Projected Pressure Map
−57°46′
−48′
−50′
−52′
−54′
−56′
−58′
Declination
21h55m00s
54m30s
54m00s
53m30s
Right Ascension
6.0e−11
4.0e−11
2.0e−11
0.0e−11
erg/cm3

Fig. 12.— (a)-(j): Projected pressure (P) maps of the clusters A193, A376, A539, A970, A1377, A1831B, A2124, A2457, A2665, and A3822, respectively, obtained from the spectral analysis of box shaped regions (see §3.5). The overlaid intensity contours are from the *Chandra* images as explained in the caption of Figure 9.

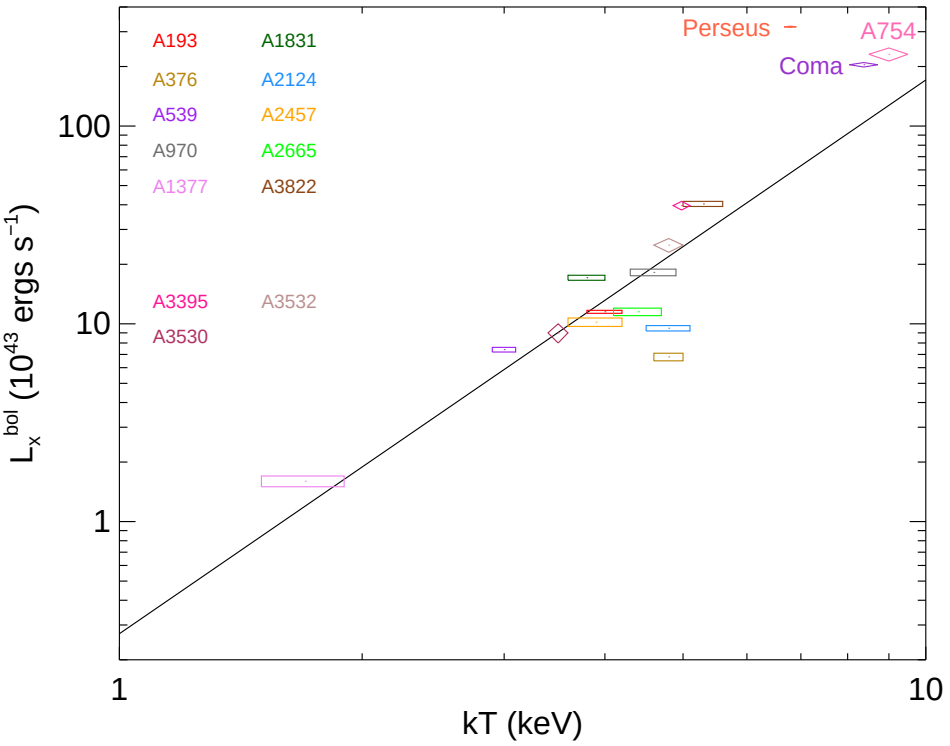

Fig. 13.— L_X-kT relation of clusters of galaxies obtained by Takey et al. (2013) (solid line). The values obtained for the ten clusters of the sample are shown as rectangles, and those of Coma, A754, Perseus, A3395, A3532 and A3530 are shown as diamonds.